Geosciences and engineering : a publication of the University of Miskolc

4. évf. 7. sz. / 2015

Balogh Gergely Pál Improved statistical analysis of geophysical logs measured in penetration holes	7-19
Poyanmehr, Zahra Geochemical analysis of Buda Thermal Karst system, Hungary	20-31
Híves Kristóf Mining and evaluation of shale reservoirs	32-44
Dobos Endre - Hegedűs András - Vágó János Estimating landslide susceptibility for the Carpathian region using GIS modeling approach	45-58
Kiss Anett How overdetermination and start model influence the estimation accuracy of an acoustic rock physical model	59-74
Paulovics József - Bokányi Ljudmilla Evaluation of the biosorption potential of Undaria pinnatifida macro algae in a column system with real effluents	75-85
Trinh Van Quyen - Nagy Sándor Effect of various production parameters on biomass agglomeration	86-96

Geosciences and Engineering, Vol. 4, No. 7 (2015), pp. 7–19.

IMPROVED STATISTICAL ANALYSIS OF GEOPHYSICAL LOGS MEASURED IN PENETRATION HOLES

GERGELY PÁL BALOGH

University of Miskolc, Department of Geophysics,
H-3515 Miskolc-Egyetemváros
E-mail: gfbg@uni-miskolc.hu

Abstract: A multivariate statistical approach is presented that can be effectively applied to the interpretation of engineering geophysical sounding measurements and geotechnical tests. By the use of factor analysis of penetration logs an estimate of water (and gas) saturation can be given. In the first step, the mechanical, electrical and radioactivity data acquired by cone penetration tools equipped with geophysical sensors are processed simultaneously to estimate the factor variables. Then, an exponential regression relation between the first factor and water saturation is used to calculate the vertical distribution of water saturation in shallow formations. The conventional algorithm of factor analysis is further developed by using Steiner's most frequent value method to give a more accurate solution in case of non-Gaussian noises and outlying data. The statistical method was tested in a western Hungarian data set to make a comparison between the procedures of traditional and Steiner-weighted factor analysis. The single-borehole method is extended to multi-borehole applications, which gives a reliable estimate of water content between the boreholes.

Keywords: *engineering geophysical sounding, factor analysis, Steiner's weight, water saturation*

1. INTRODUCTION

The engineering geophysical sounding (EGS) method allows the in-situ geophysical investigation of shallow structures and is an improved version of the CPT (Cone Penetration Test) method [1]. In the beginning, this technology gave information only about soil mechanical parameters. However, it was further developed, which opened new paths for geophysical measurements. Several types of physical parameters can be observed in penetration holes with a specialty that only the steel tube isolates the probe from the soil, and the measured data are transferred through the rods pushed into the ground. EGS tools can be used for the assessment of shallow freshwater-bearing formations, which include geophysical detectors for measuring geotechnical, electrical and nuclear data. For detecting the hydrocarbon contamination in soils, PÉREZ-CONONA et al. [2] used a 2D method for imaging the subsurface resistivity for different electrode arrays. Similarly, DRAHOS and GALSA [3] developed a multidimensional numerical approach to investigate the vertical and radial characteristic of the resistivity tool in inhomogeneous medium. The EGS technique using several log types gives quantitative information on the composi-

tion, porosity, shale content and water saturation of the subsoils. The interpretation of the EGS data is generally made by deterministic or point-by-point inversion methods [4]. Statistical processing of EGS data is also a promising approach, as is demonstrated in this paper. Multivariate methods like principle component analysis, exploratory factor analysis and cluster analysis make it possible to separate lithological units, detect pore-filling fluids, and estimate petrophysical parameters of the sediments.

Factor analysis is normally applied to reduce the number of observed parameters and extract latent information from a statistical sample [5]. In geophysics, the measured data is analyzed to calculate factors that can be related to petrophysical properties of the formations [6], [7], [8]. In hydrocarbon formation evaluation, SZABÓ [9] developed a factor analysis based technique to estimate the shaliness of shaly-sand reservoirs. The factor analysis of EGS logs allows the estimation of water saturation and the simulation of neutron-porosity data for unmeasured intervals [10]. JÖRESKOG [11] suggested a non-iterative solution to the problem of factor analysis, which gives optimal results for normally distributed data. This requirement is usually not fulfilled for EGS data, because asymmetric data sets and outliers may distort the solution significantly. In this study, the classical factor analysis algorithm (FA) is further developed to give a more robust solution using STEINER'S [12] most frequent value method (MFV-FA). The new method is based on the iterative improvement of the deviation between the measured and calculated data. During the procedure of factor analysis, optimal weights are re-calculated for EGS data to estimate the factor logs in a robust manner. The MFV method-based factor analysis procedure is tested in a Hungarian measurement area, and results are compared to those of independent inverse modeling.

2. THE MOST FREQUENT VALUE AND THE STEINER'S WEIGHTS

We know several methods for the estimation of the mean of the statistical sample, which can be very noise-sensitive, but there are some noise-resistant methods, too. If we give small weights (w_k) to points away from the plurality of the data (x_k), and large ones to points where we have the highest data density, we get a location parameter as a statistical characteristics, which is more reliable estimator than the arithmetic mean. The weighted average of data is

$$M = \frac{\sum_{k=1}^{N} x_k w_k}{\sum_{k=1}^{N} w_k} \qquad (k = 1,2,\ldots N) \cdot \tag{1}$$

STEINER [12] chose the k-th weight as follows

$$w_k = \frac{\varepsilon^2}{\varepsilon^2 + (x_k - M)^2} \quad , \tag{2}$$

where N is the number of data, ε is the scale parameter called dihesion. If the value of ε is large, all data obtain the same weight and outliers spoil the estimation of the characteristic value, but in case of small ε, the data far away from the center are ignored. The weighted mean *(M)* defined in *Equation (1)* is called the most frequent value. *Equation (1)* is a recursive process for the calculation of M; therefore, an iterative algorithm is needed in which the values of M and ε are simultaneously estimated. In the first iteration step, dihesion can be chosen from the sample range

$$\varepsilon_1 \le \frac{\sqrt{3}}{2}\left[\max(x_k) - \min(x_k)\right], \tag{3}$$

while the initial value of M_1 can be the sample mean or median. In the following iteration steps, M and ε are derived by iteration

$$\varepsilon_{j+1}^2 = \frac{3\sum_{k=1}^{N} \frac{\left(x_k - M_j\right)^2}{\left[\varepsilon_j^2 + \left(x_k - M_j\right)^2\right]^2}}{\sum_{k=1}^{N} \frac{1}{\left[\varepsilon_j^2 + \left(x_k - M_j\right)^2\right]^2}} \Leftrightarrow M_{j+1} = \frac{\sum_{k=1}^{N} \frac{\varepsilon_{j+1}^2}{\varepsilon_{j+1}^2 + \left(x_k - M_j\right)^2} x_k}{\sum_{k=1}^{N} \frac{\varepsilon_{j+1}^2}{\varepsilon_{j+1}^2 + \left(x_k - M_j\right)^2}}. \tag{4}$$

As an example, we show the calculation of M for a cone-resistance *(RCPT)* log measured in Bátaapáti, southwest Hungary [4].

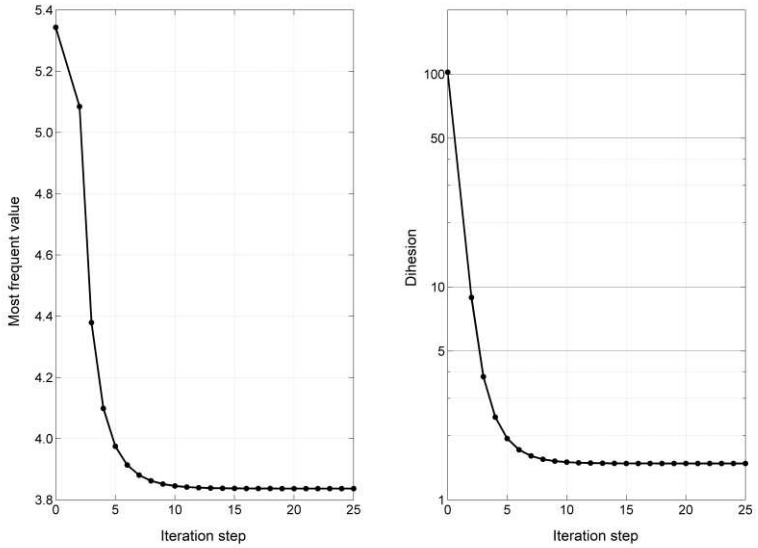

Figure 1. The convergence of the most frequent value (on the left) and dihesion (on the right) in the MFV iteration procedure

In *Figure 1,* the development of convergence for the optimal values of the most frequent value and the dihesion is shown. The dihesion gradually decreases, while less and less weights are given to the outliers. The arithmetic mean and the most frequent value of the *RCPT* log are shown in *Figure 2.* It can be seen that the estimation of the most frequent value is resistant, while the arithmetic mean is quite sensitive to outliers

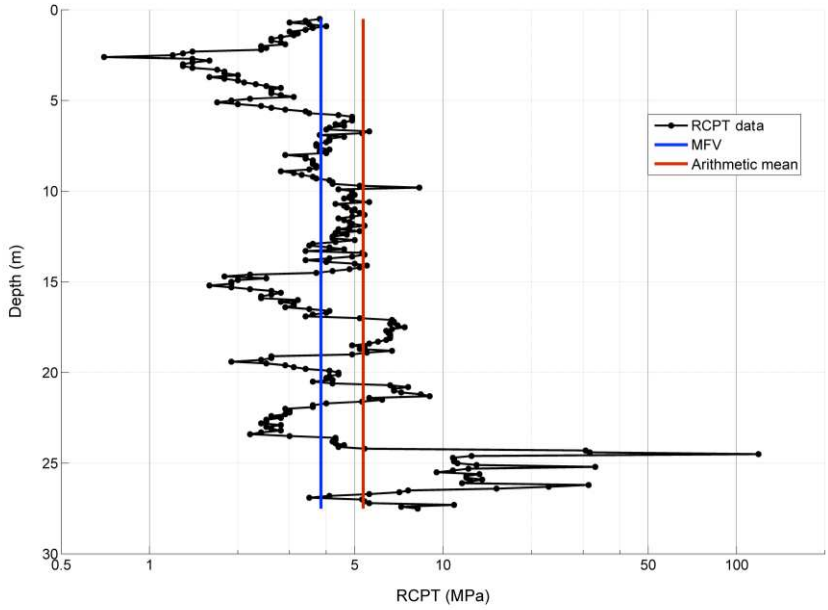

Figure 2. The most frequent value and arithmetic mean of the RCPT data set

3. MFV-BASED FACTOR ANALYSIS

The input of factor analysis is the *N*-by-*K* matrix of standardized EGS data (**D**), which is decomposed into two matrices

$$\mathbf{D} = \mathbf{F}\mathbf{L}^{\mathrm{T}} + \mathbf{E}, \tag{5}$$

where **F** is the *N*-by-*Q* matrix of factor scores, **L** is the *K*-by-*Q* matrix of factor loadings and **E** is the matrix of residuals (*Q* is the number of extracted factors, *N* is the number of depth points and *K* is the number of EGS logs). The factor loadings and the factor scores are generally estimated jointly by the maximum likelihood method. JÖRESKOG [11] proposed a fast (non-iterative) algorithm for calculating the factor loadings, which gives optimal results for normally distributed data. The conventional model of factor analysis defined in *Equation (5)* is reformulated

$$\mathbf{d} = \tilde{\mathbf{L}}\mathbf{f} + \mathbf{e}, \tag{6}$$

where **d** denotes the *KN* column vector of EGS data, $\tilde{\mathbf{L}}$ is the *NK*-by-*NQ* matrix of factor loadings, **f** is the *QN* vector of factor scores, **e** is the *KN* vector of prediction errors (i.e. deviations between measured and calculated EGS data). In the first step of the robust procedure, we give an estimate to the initial values of factor loadings and scores by JÖRESKOG'S method [11]. Then, these starting values are refined gradually by an iterative algorithm which takes the form in the *q*-th iteration step as

$$\mathbf{L}^{\mathrm{T}(q)} = \left(\mathbf{F}^{\mathrm{T}(q-1)}\mathbf{F}^{(q-1)} + \alpha^2\mathbf{I}\right)^{-1}\mathbf{F}^{\mathrm{T}(q-1)}\mathbf{D}, \tag{7}$$

$$\mathbf{f}^{(q)} = \left(\tilde{\mathbf{L}}^{\mathrm{T}(q-1)}\mathbf{W}\tilde{\mathbf{L}}^{(q-1)}\right)^{-1}\tilde{\mathbf{L}}^{\mathrm{T}(q-1)}\mathbf{W}\mathbf{d}, \tag{8}$$

where α is a properly chosen damping factor. The elements of the *NK*-by-*NK* diagonal weight matrix **W** are proportional to the deviation of measured (**d**) and calculated data ($\tilde{\mathbf{L}}\mathbf{f}$). The elements of **W** matrix are the Steiner weights given in *Equation (2)* by $M = 0$ as we have standardized data ($j = 1,2,\ldots, KN$)

$$W_{jj} = \frac{\varepsilon^2}{\varepsilon^2 + (e_j)^2}\ . \tag{9}$$

The optimal values of dihesion and the most frequent value of the data prediction errors are estimated simultaneously in an inner loop of the MFV-FA method. The larger the distance between the observed and predicted data in *Equation (9),* the less weight given to the relevant datum. At the end of the MFV-FA procedure the vertical distribution of factor scores is given.

The former (one-dimensional) algorithm of the MFV-FA method was developed for the simultaneous processing of EGS data sets acquired from several boreholes drilled along a survey line. As a result of the 2D MFV-FA procedure, the 2D sections of the factor variables can be derived from a much larger statistical sample than a single borehole yields. Let $\mathbf{D}_h$ denote the data matrix of the *h*-th borehole *(h* = 1,2,…,*H).* After gathering the standardized data of several neighboring boreholes into the integrated data matrix $\mathbf{D}^* = (\mathbf{D}_1,\ldots,\mathbf{D}_h,\ldots,\mathbf{D}_H)^{\mathrm{T}}$, the initial values of factor scores can be estimated by Jöreskog's method. The calculated data vector is $\mathbf{e}^* = \mathbf{d}^* - \tilde{\mathbf{L}}^*\mathbf{f}^*$, which in matrix form is

$$\begin{pmatrix} \mathbf{d}_1 \\ \vdots \\ \mathbf{d}_h \\ \vdots \\ \mathbf{d}_H \end{pmatrix} = \begin{pmatrix} \tilde{\mathbf{L}}_1 & 0 & 0 & 0 & 0 \\ 0 & \ddots & 0 & 0 & 0 \\ 0 & 0 & \tilde{\mathbf{L}}_\mathrm{h} & 0 & 0 \\ 0 & 0 & 0 & \ddots & 0 \\ 0 & 0 & 0 & 0 & \tilde{\mathbf{L}}_H \end{pmatrix} \begin{pmatrix} \mathbf{f}_1 \\ \vdots \\ \mathbf{f}_h \\ \vdots \\ \mathbf{f}_H \end{pmatrix} + \begin{pmatrix} \mathbf{e}_1 \\ \vdots \\ \mathbf{e}_h \\ \vdots \\ \mathbf{e}_H \end{pmatrix}, \tag{10}$$

where $\tilde{\mathbf{L}}_h$ and $\mathbf{f}_h$ denote the matrix of factor loadings and the vector of factor scores estimated along the h-th penetration hole, respectively. Having N_h number of processed depths in the h-th hole, the total number of processed depth levels is $N^* = N_1+N_2+\ldots+N_H$. By using the same number of EGS tools in all penetration holes, the size of the diagonal weight matrix $\mathbf{W}$ modifies to KN^*-by-KN^* in the 2D MFV-FA procedure. The factor loadings $\mathbf{L}^*$ and the factor scores $\mathbf{f}^*$ are analogously determined as in the 1D case by using *Equations (7)* and *(8).* The 2D maps of factor scores obtained by the above procedure can be directly correlated to the petrophysical parameters of soils. The results of regression experiments and field applications are shown in the next section.

4. CASE STUDY

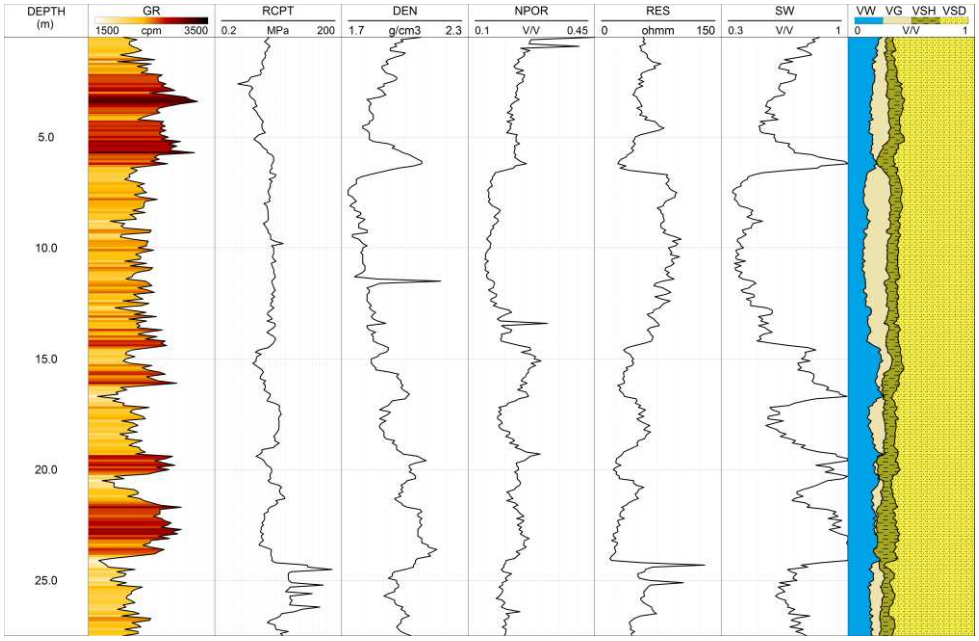

Figure 3. EGS data contaminated by outlying data, water saturation estimated by weighted inversion, the logs of water and gas content, sand and shale volumes

The feasibility of the MFV-FA procedure is demonstrated using real EGS data measured in Bátaapáti, southwest Hungary. The maximal depth of penetration holes is approximately 25 meters. The formations investigated are composed of loose shaly and loessy sand saturated with air and freshwater. The soil parameters of interest are the volumetric rations of sand *(VSD),* shale *(VSH),* water *(VW)* and gas *(VG).* The sum of *VW* and *VG* gives porosity *(POR),* the pore space occupied by water is the water saturation *(SW).* Cone resistance *(RCPT),* natural gamma-ray intensity *(GR),* density *(DEN),* neutron-porosity *(NPOR)* and resistivity *(RES)* logs

are available for the statistical analysis. The soil parameters can be evaluated by local inversion using a weighted-least-squares method, which minimizes the deviation between the observed and calculated data normalized to the data variances in each depth, separately [4], [13]. The physical variables observed in a penetration hole and the composition of sediments estimated from inverse modeling are plotted in *Figure 3*. Preliminary tests of normality revealed that with the exception of the natural gamma-intensity log, the EGS data follow non-Gaussian distribution. The outliers may distort the solution of the conventional FA procedure.

The MFV-FA procedure improves the Jöreskog solution by updating the factor loadings and scores by *Equations (7)–(9).* The relative distance (RMS) between the measured and calculated data is reduced gradually during the iteration procedure. The factor loadings and factor scores are updated in 15 steps, and in an inner loop the Steiner-weights are recalculated in 30 further steps, at the same time the dihesion is automatically decreased and changed differently for each EGS log. As a result, keeping the same value of ε, the larger the misfit between the measured and calculated data, the smaller the value of the weights. With the decrease in ε, larger deviations (owing to outliers) contribute less to the solution. *Figure 4* shows the decrease in the L_1-norm of the vector of prediction errors and the median of the Steiner's weights with the iteration steps. It is seen that the MFV-FA procedure converges continuously to the optimum, which proves the stability of the statistical procedure. The data misfit for the MFV-FA procedure is smaller than that of the traditional FA method.

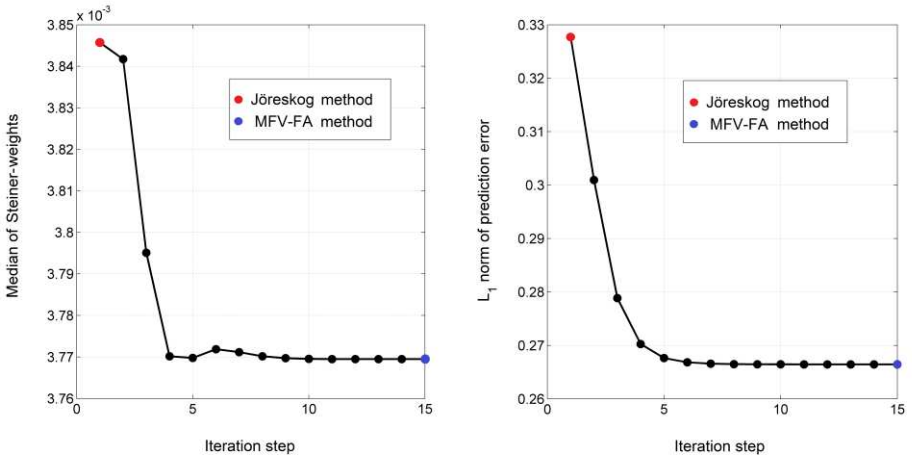

Figure 4. Median of Steiner-weights (on the left) and the convergence of the L_1 norm of the prediction error in the MFV-FA procedure (on the right)

In the given example, two independent factors are calculated by the MFV-FA method. The loadings of the first factor are –0.01 *(RCPT),* 0.17 *(GR),* 0.86 *(DEN),*

0.73 *(NPOR),* −0.88 *(RES),* which show the partial correlations between the EGS logs and the first factor. The strongest correlation is indicated between the first factor and water saturation-sensitive logs *(NPOR, RES),* as well as the *DEN* log. *Figure 5* shows that the first factor (F_1) is connected to water saturation (S_w) by the following regression relation

$$S_w = ae^{-bF_1} + c\,. \tag{11}$$

The regression coefficients of the above exponential function are estimated with 95% confidence bounds (a = 0.77±0.14, b = 0.22±0.04, c = −0.12±0.11). The Pearson's correlation coefficient between the first factor and water saturation is R = 0.96 for the FA method and R = 0.98 for the MFV-FA procedure. In *Figure 5,* it can be seen that the MFV-FA method effectively suppresses the effect of the outliers. *Figure 6* shows the factor logs estimated by the conventional FA method (F1_FA) and the further developed robust MFV-FA process (F1_MFV−FA). The resultant water saturation log can be compared to the results of independent point-by-point inversion *(SW_INV).* The deviation between the results of conventional factor analysis and inverse modeling is *RMS* = 7.4%. The same quantity is *RMS* = 4.6 % computed for the iteratively reweighted statistical method. We can notice that in depths of the outliers the extreme noises do not influence the result of MFV-FA procedure. For example, between 10 and 15 m as well as in the vicinity of 25 m, the first factor (F1_MFV−FA) and the derived water saturation profiles (SW_MFV−FA) do not include outliers. It is shown that the MFV-FA procedure is outlier-resistant and gives reliable results.

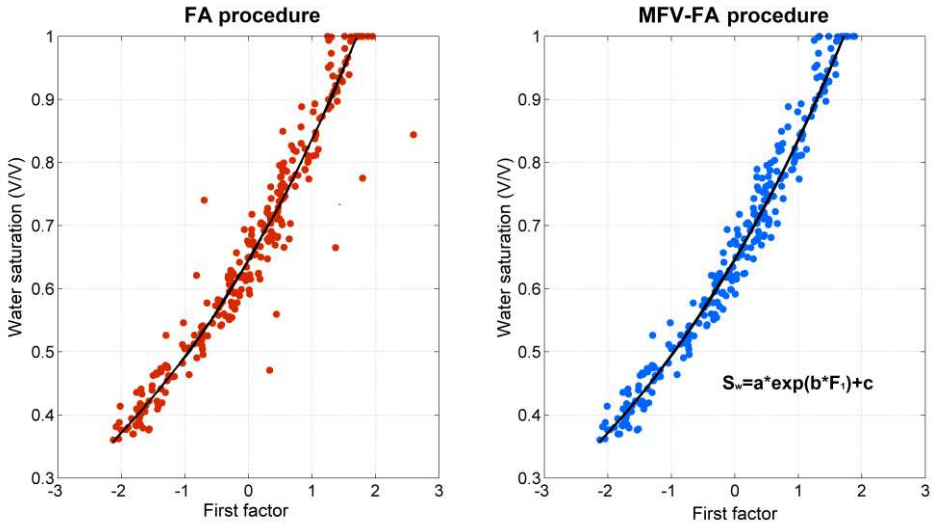

Figure 5. Regression relation between the first factor and water saturation for the case of outlying data given by FA procedure (on the left) and local inverse modeling (on the right)

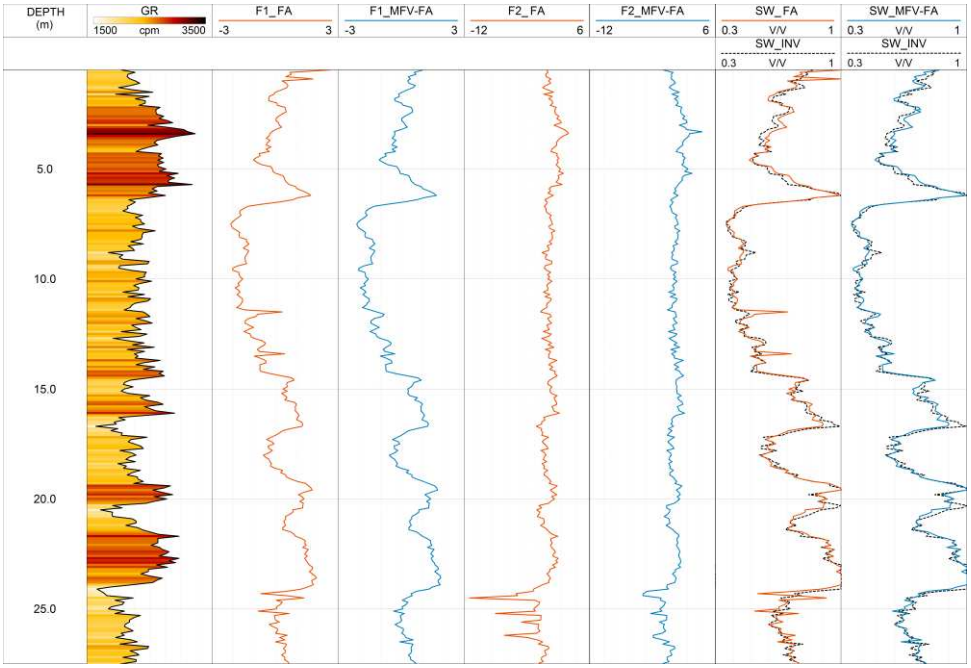

Figure 6. Factor logs estimated by the traditional FA and MFV-FA procedures, water saturation logs estimated by factor analysis and local inversion

The 2D processing of well logs is usually favorable for better interpretation and maximization of subsurface information [14]. The EGS data set of 12 penetration holes measured over the Bátaapáti site is processed by the 2D MFV-FA method using *Equation (10).* The penetration hole of the earlier (1D MFV-FA) statistical analysis is located at horizontal distance 550 m along the survey line. The same control parameters are used as in the 1D MFV-FA problem, where the total number of processed data is 15,500. The relative number of outliers is small, but the use of 2D factor analysis is favorable because of the large statistical sample. The 2D section of the first statistical factor is estimated directly by the 2D MFV-FA method *(Figure 7).* From the results of 2D factor analysis, a regression analysis can be made to detect the relation between the factor scores and water saturation for the whole area. *Figure 8* illustrates a strong correlation between the first factor and water saturation. The regression coefficients in *Equation (11)* are estimated with 95% confidence bounds: $a = 0.85 \pm 0.04$, $b = 0.20 \pm 0.01$ and $c = -0.23 \pm 0.04$. These values of regression coefficients are close to those of the 1D case. On the other hand, it is observable that the estimation errors are significantly reduced. This is the result of the processing of a large statistical sample (i.e., data of several penetration holes) in the 2D procedure. The figure also shows good agreement between the results of factor analysis (2D MFV-FA) and those of the local inversion made separately well-by-well. In *Figure 9,* it can be seen that both the horizontal and

vertical distribution of water saturation can be determined by the 2D MFV-FA method. The blue shaded area represents highly saturated formations, while the shallow air-filled soils are indicated by greenish color. By the use of factor analysis further derived quantities such as dry density and hydraulic conductivity can be estimated [15], [16].

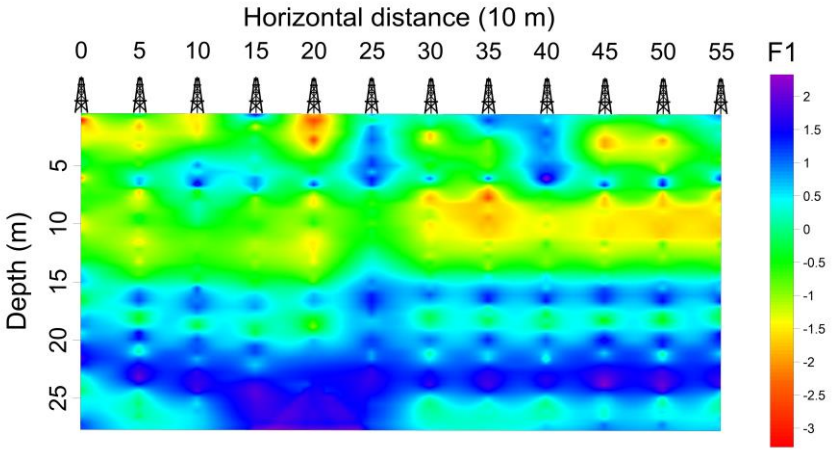

Figure 7. The section of the first factor estimated by the 2D MFV-FA procedure

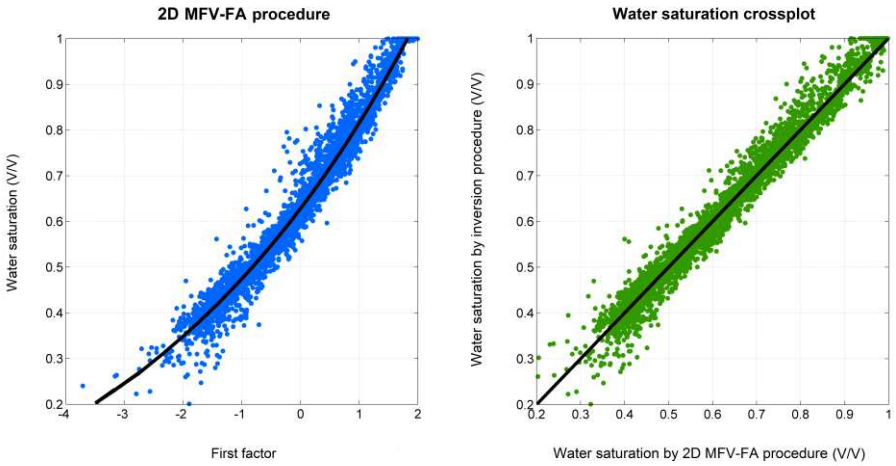

Figure 8. Regression relation between the first factor and water saturation (on the left), water saturation estimated by 1D inversion and 2D MFV-FA procedures (on the right)

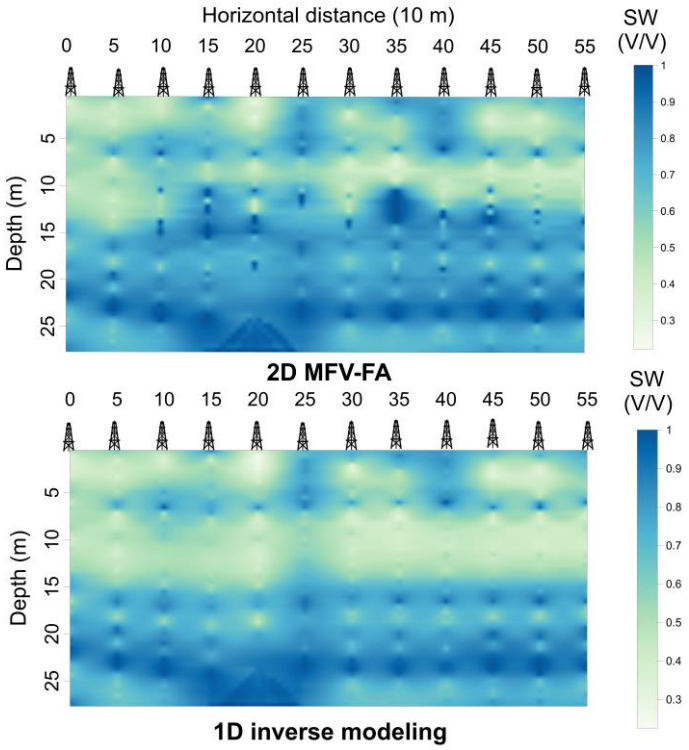

Figure 9. Water saturation sections estimated by 2D MFV-FA method and a set of 1D local inversion procedures

5. CONCLUSIONS

A new robust factor analysis method is proposed for the evaluation of engineering geophysical sounding (EGS) measurements. The statistical factors are calculated by the joint processing of EGS data. From the factor scores the water saturation and gas content of near-surface layers are derived. The robust factor analysis algorithm is different from the conventional method, as it weights not only the specific variances, but it also takes the accuracy of each data point into consideration. Optimal weights are calculated from the deviation between the measured and calculated EGS logs. With the factor–water saturation relation an independent estimation of water saturation can be given, which can increase the reliability of the interpretation results. According to experience, at least 40% improvement can be achieved by the use of the MFV-FA method. The estimation accuracy of water saturation can be further increased by integrating and analyzing EGS data of several penetration holes. The implementation of the two-dimensional factor analysis is also presented in this study, which facilitates to extend the results of factor analysis to a larger area and improve the petrophysical model of heterogeneous unconsolidated formations.

ACKNOWLEDGEMENTS

The author thanks the support of the Hungarian Scientific Research Fund for OTKA project PD-109408, Assoc. Prof. Norbert Péter Szabó and Prof. Mihály Dobróka (University of Miskolc) for their scientific advice and Assoc. Prof. Dezső Drahos (Eötvös Loránd University) and János Stickel (Elgoscar Ltd.) for their cooperation.

REFERENCES

[1] FEJES–JÓSA 1990
FEJES, I.–JÓSA, E.: The engineering geophysical sounding method: Principles, instrumentation, and computerised interpretation. In: S. H. WARD (ed.): *Geotechnical and Environmental Geophysics 2: Environmental and groundwater*. Society of Exploration Geophysicists, 1990, 321–331.

[2] PÉREZ-CORONA et al. 2016
PÉREZ-CORONA, M.–GARCÍA, J. A.–TALLER, G.–POLGÁR, D.–BUSTOS, E.–PLANK, Z.: The cone penetration test and 2D imaging resistivity as tools to simulate the distribution of hydrocarbons in soil. *Physics and Chemistry of the Earth*, 91, 2016, 87–92.

[3] DRAHOS–GALSA 2007
DRAHOS, D.–GALSA, A.: Finite element modelling of penetration electric sonde (in Hungarian). *Magyar Geofizika*, 48, 2007, 22–30.

[4] DRAHOS 2005
DRAHOS, D.: Inversion of engineering geophysical penetration sounding logs measured along a profile. *Acta Geodetica et Geophysica Hungarica*, 40, 2005, 193–202.

[5] LAWLEY–MAXWELL 1969
LAWLEY, D. N.–MAXWELL, A. E.: Factor analysis as a statistical method. *The Statistician*, 12, 1969, 209–229.

[6] XU et al. 2010
XU, C.–DAI, F.–YAO, X.–ZHAO, Z.–XIAO, J.: GIS platform and certainty factor analysis method based Wenchuan earthquake-induced landslide susceptibility evaluation. *Journal of Engineering Geology*, No. 1, 2010, 15−26.

[7] STOFFERS–PLÜGER–WALTER 1984
STOFFERS, P.–PLÜGER, W.–WALTER, P.: Geochemistry and mineralogy of continental margin sediments from Westland, New Zealand. *New Zealand Journal of Geology and Geophysics,* 27, 1984, 351–362.

[8] ANDRADE 2014
ANDRADE, R.: Delineation of fractured aquifer using numerical analysis (factor) of resistivity data in a granite terrain. *International Journal of Geophysics*, ID 585204, 2014, 8.

[9] SZABÓ 2011
SZABÓ, N. P.: Shale volume estimation based on the factor analysis of well-logging data. *Acta Geophysica,* Vol. 59, No. 5 (2011), 935–953.

[10] SZABÓ–DOBRÓKA–DRAHOS 2012
SZABÓ, N. P.–DOBRÓKA, M.–DRAHOS, D.: Factor analysis of engineering geophysical sounding data for water saturation estimation in shallow formations. *Geophysics*, 77, 2012, WA35–WA44.

[11] JÖRESKOG 2007
JÖRESKOG, K. G.: Factor analysis and its extensions. In: CUDECK, R.–MACCALLUM, R. C. (eds.): *Factor analysis at 100: Historical developments and future directions*. Lawrence Erlbaum Associates, Mahwah, NJ, 2007, 47–77.

[12] STEINER 1991
STEINER, F.: *The Most Frequent Value, Introduction to a Modern Conception of Statistics*. Academic Press, Budapest, 1991.

[13] DOBRÓKA–SZABÓ 2012
DOBRÓKA, M.–SZABÓ, N. P.: Interval inversion of well-logging data for automatic determination of formation boundaries by using a float-encoded genetic algorithm. *Journal of Petroleum Science and Engineering*, 86–87, 2012, 144–152.

[14] DOBRÓKA et al. 2009
DOBRÓKA, M.–SZABÓ, P. N.–CARDARELLI, E.–VASS, P.: 2D inversion of borehole logging data for simultaneous determination of rock interfaces and petrophysical parameters. *Acta Geodaetica et Geophysica Hungarica*, 44, 2009, 459–479.

[15] SZABÓ 2012
SZABÓ, N. P.: Dry density derived by factor analysis of engineering geophysical sounding measurements. *Acta Geodaetica et Geophysica Hungarica*, 47, 2012, 161–171.

[16] SZABÓ 2015
SZABÓ, N. P.: Hydraulic conductivity explored by factor analysis of borehole geophysical data. *Hydrogeology Journal*, 23, 2015, 869−882.

Geosciences and Engineering, Vol. 4, No. 7 (2015), pp. 20–31.

GEOCHEMICAL ANALYSIS OF BUDA THERMAL KARST SYSTEM, HUNGARY

ZAHRA POYANMEHR

University of Szeged, Doctoral School of Geosciences
e-mail: poyan@freemail.hu

Abstract: The purpose of this study is to characterize the different groundwater flow systems of the Buda Thermal Karst system by evaluation of the geochemistry of the water. Cluster analysis was applied to classify similar objects to categories. Measured concentration of main cations, anions and stable isotopes in the karst water were plotted on a graph to check the reliability of cluster groups, the spatial distribution of objects and the main flow paths of the region. Geochemical analysis of thermal waters resulted in three different main flow paths. The presence of younger water in the flow system (10% to near 50%) in the Central zone of Budapest prove the mixing of old and hot thermal water with younger and lukewarm waters. The young waters partly originate from an uncovered carbonate area (recharge area) as a shallow intermediate flow system and the other part from the covering sediments. This confirms the sensitivity of the thermal springs to infiltrated pollution in the Central zone of Budapest.

Keywords: *Buda Thermal Karst, flow system, mixing, geochemistry*

1. INTRODUCTION

The Buda thermal system, with more than 100 springs, wells and observation wells, is under an increasing threat from growing discharge, overexploitation and contamination. To characterize the flow system of the study area water geochemistry data, among other data, have been recorded for a long time. Three main discharge zones were identified based on temperature and geochemical properties of thermal waters in Budapest (ALFÖLDI et al., 1968): lukewarm springs (20–28 °C) from the intermediate flow system discharging north of Budapest (North Zone), hot springs (40–60 °C) from the regional flow system discharging in south Budapest (South Zone) and a central zone, consisting of both lukewarm (from the intermediate flow system) and hot springs discharging next to each other (Central Zone) (ALFÖLDI, 1981; SÁRVÁRY, 1995).

The age of the hot springs (40–60 °C) was estimated to be between 5,000 and 16,000 years (DEÁK, 1978). The water of the hot springs was rich in total dissolved solids (1,200–1,700 mg/l) and CO_2 (200–400 mg/l) and characterized by a Ca–Na–Cl–SO_4–HCO_3 hydrogeochemical facies (GOLDSCHEIDER et al., 2010). Different flow paths were indicated by diverse temperature range and distinct chemical composition (e.g. total dissolved solid) of thermal water in the area (ALFÖLDI et al., 1968).

The goal of this study was to characterize the different flow paths in the area by the evaluation of archive hydrogeochemical, environmental isotope data and to provide more precise information based on previous studies. This could help to make decisions related to the management of the karst system and the remediation of contaminated springs and wells.

2. DESCRIPTION OF THE STUDY AREA

The study area is located in the NE part of the Transdanubian Central Range (TCR). It consists of several thousand meters of Mesozoic carbonate rocks (HAAS et al., 1988). One of the regional discharge areas of TCR is localized in Budapest, where the Danube as the main river or main base level of erosion separates the hilly range in the west (Buda) and step-faulted subsided basin in the east (Pest). Gradual uplifting of the area resulted in an outcrop of Triassic-Eocene carbonate rocks in the western and northwestern highlands, which are known to be the main recharge area. The precipitation percolates through the uncovered carbonate rocks in the highlands. It flows mainly gravitationally (ALFÖLDI et al., 1979) but is also influenced by strong convective heat flow and increasing geothermal gradient (75–100 ^{o}C/km) (ALFÖLDI, 1982; LORBERER, 2002).

The gravity-driven groundwater flows along the step-faulted basin in different scales which is understood within a conceptual framework of hierarchical flow systems, as a local, intermediate and regional flow system (TÓTH, 1962, 1963, 1999; ERŐSS et al., 2008).

Based on previous studies (ALFÖLDI, 1978; 1982; KORPÁS, 1999), circulation of thermal karst water within the dolomitic limestone formation was found to be controlled by depositional features (unconformities, cave and clustic horizons) and by tectonic features such as faults and related fractures. “Ascending thermal water (along faults) mixes with cooler meteoric water giving the thermal springs and spa along the Danube.” (WERNER et al., 2014)

3. RESULTS

The geochemical composition of 80 wells and springs in the wider area of Budapest was used to characterize the different flow paths in the study area *(Figure 1).* The data were recorded between 1950 and 2004 with different time steps and consist of the major cations (Na^+, Ca^{2+}, Mg^{2+}), anions (Cl^-, SO_4^{2-}, HCO_3^-) and temperature. To unify the data of every sampling point the median value of components was considered.

Cluster analysis was performed to classify the water samples belonging to different main flow paths in the study area. SPSS software was applied for hierarchical cluster analysis method and average linkage agglomerative clustering to statistically analyze data.

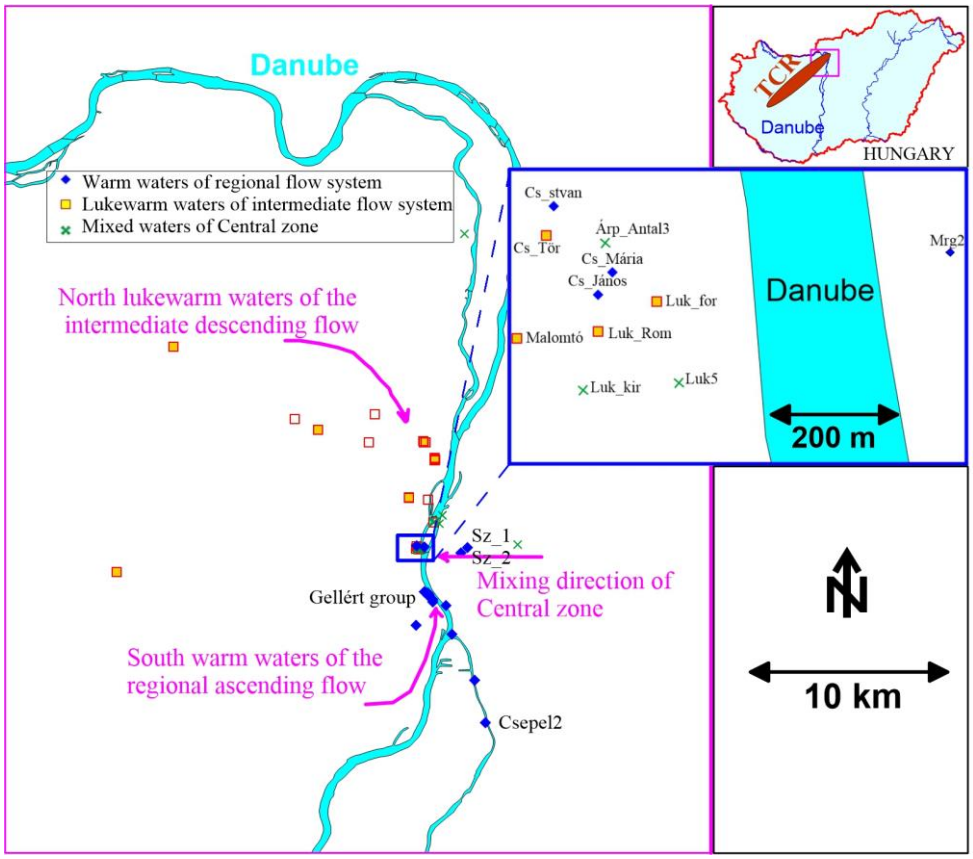

Figure 1. Study area with three different flow paths: North lukewarm intermediate flow, South warm regional flow and the Central Zone where both flow systems discharge next to each other in the Western part of the Danube. Wells group are shown based on cluster analysis classification (TCR: Transdanubian Central Range)

Water samples were classified into three main groups, based on the major cations, anions and temperature. These groups were: the lukewarm waters, belonging to the North Zone and the intermediate flow system; warm and sulphurous water belong to the regional flow system; and mixed water of the Central Zone, where the old and hot regional flow mixed with younger water.

The spatial distribution of objects and the main flow paths of the region, the relation between main cations, anions and stable isotope components were illustrated and evaluated to check the reliability of cluster groups.

The three main flow paths in the study area were confirmed by the relation between Cl^- and SO_4^{2-} concentration *(Figure 2).* The origin of the water could be determined by the concentration of chloride ion, being the conservative component, while water-rock interaction along the flow path results in a higher sulphate concentration.

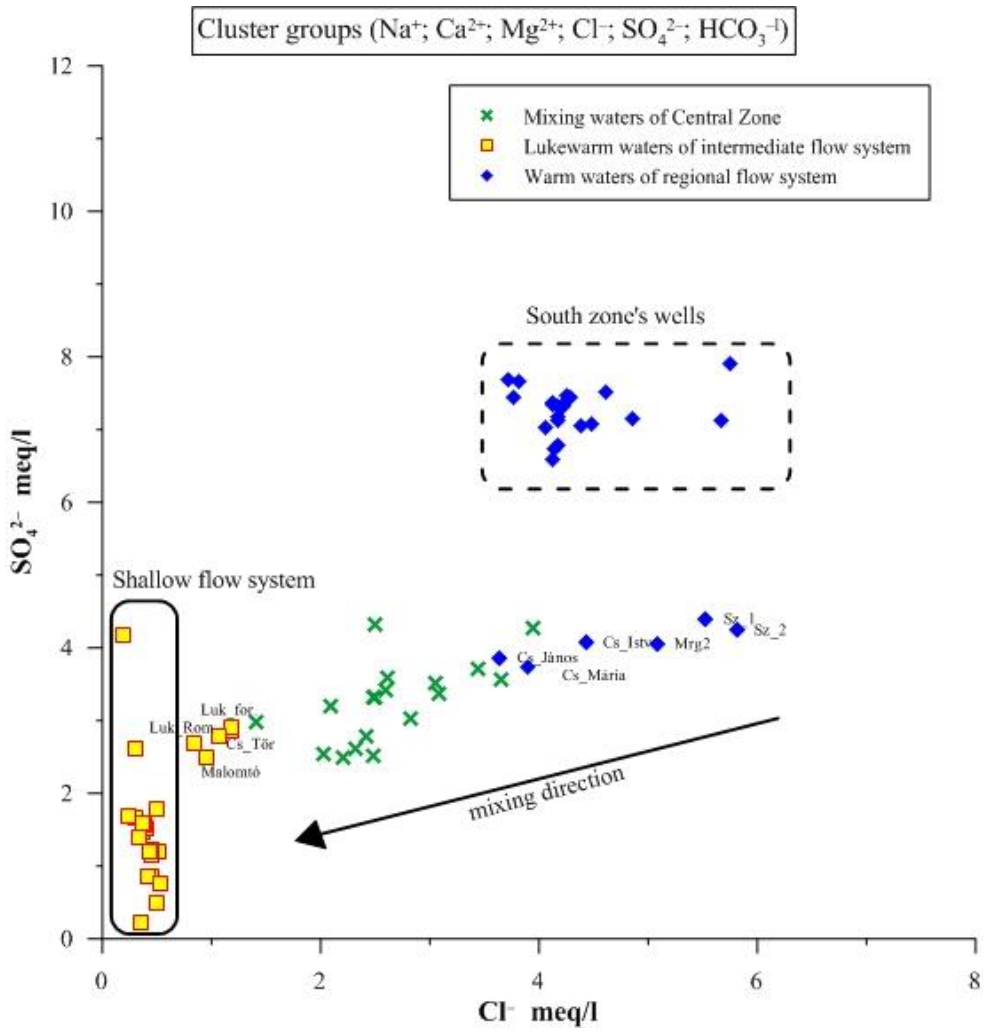

Figure 2. Relation between Cl^- and SO_4^{-2} concentration of Buda thermal waters

In *Figure 2* the South Zone wells were represented by the dashed line framed group with high concentrations of Cl^- and SO_4^{2-}. The lukewarm shallow flow system was shown by the solid line encircled group, with nearly constant Cl^- concentration. The Central Zone, where the waters of different origin mixed with each other, was represented by a decrease in Cl^- concentration along the flow path toward the springs. Despite the cluster groups, several wells of intermediate flow and regional flow are located in the Central Zone. The existence of water of hot and regional flow (diamond) and water of lukewarm intermediate flow (square) in the Central Zone represents the mixing and discharge of two different origins (flow path) of water near the springs in the well tectonized Central Zone.

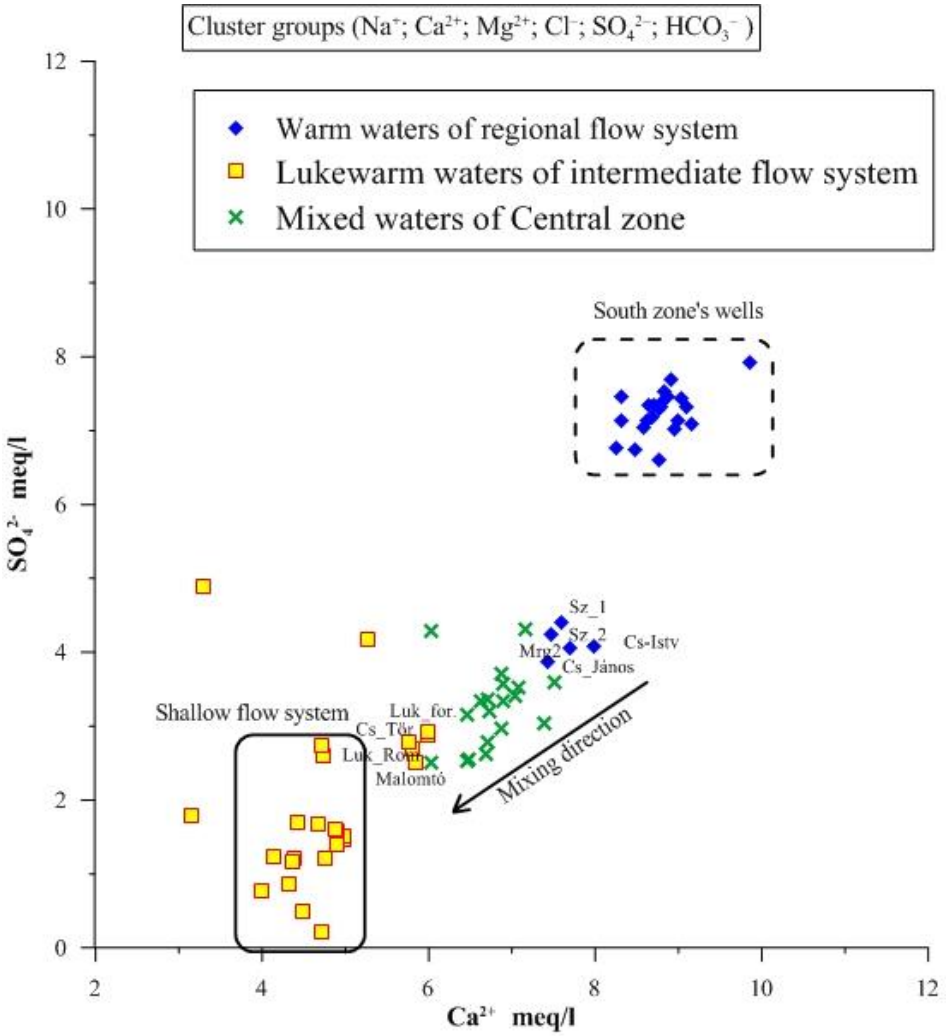

Figure 3. Relation between Ca^{2+} and SO_4^{2-} concentration

The three main flow paths were also confirmed by the relation between Ca^{2+} and SO_4^{2-} concentrations. In *Figure 3,* the South zone wells with a high concentration of Ca^{2+} and $SO_4^{2-}$are separated from the shallow flow system with increasing SO_4^{2-} concentration. Despite the cluster groups, some members of the regional (diamond) and intermediate flow (square) are located in the Central Zone, representing the mixing and discharge of waters of two different origins near the springs.

The stable isotopic composition of waters was plotted on a $\delta^{18}O$–δD diagram *(Figure 4).* Water infiltrated at various temperatures was indicated by scattered points along the Global Meteoric Water Line (GMWL). The GMWL was reported by CRAIG (1961):

$$\delta D = 8 \times \delta^{18}O + 10$$

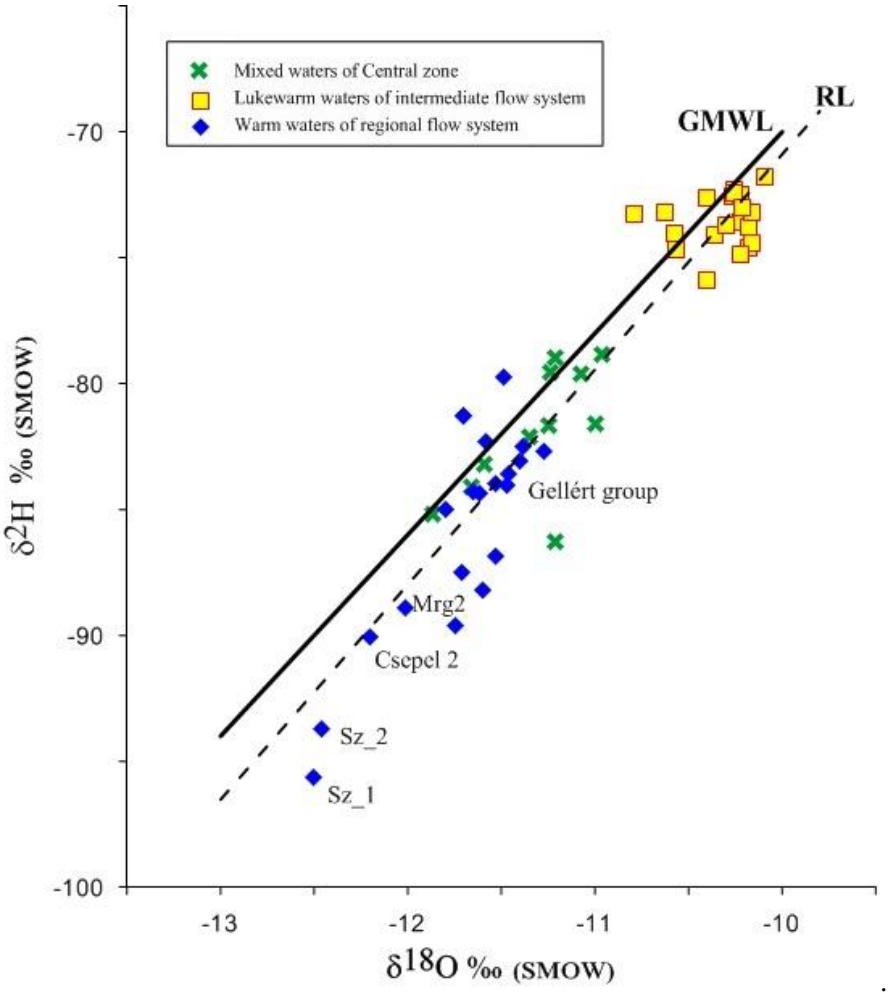

Figure 4. Relation of $\delta^{18}O$(SMOW) and δD of Buda Thermal Waters; RL: fitted Regression Line of samples

Fitted regression of samples was similar to the global water line: $D = 8.5\times\delta^{18}O+14.5$. In Hungary, Holocene waters had $\delta^{18}O$ value between –9,3‰ and –10‰ (VSMOW). The waters infiltrating during the last glacial period or end of the Pleistocene had $\delta^{18}O$ values of –11‰ and –14‰ (VSMOW). The $\delta^{18}O$ values between –10‰ and –11‰ represents the infiltration during a transitional period or mixing waters (BARBIDORICS et al., 1998; DEÁK et al., 1996). In *Figure 4* the North Zone's wells (square) were separated from the other wells. They had Holocene waters belonging to the shallow intermediate flow path. In the remaining water samples, the presence of younger water in the Central zone (from Sz_1, Sz_2 wells toward the mixing waters of Central Zone) and the south of Budapest (from Csepel2 well toward the Gellért group) was indicated by a decrease in heavy

oxygen isotope concentration of about –13‰, –11.5‰ and in deuterium of about –95‰, –75‰, respectively.

The mixing of end members in the Central Zone was confirmed by radionuclides (ERŐSS, 2012). However, in the South Zone this was not confirmed. This research revealed only the hydrothermal water discharge in the South Zone's wells and springs, and suggested that probably another fluid component enters the system in the (–400) and (+100) m a.s.l. elevation interval (ERŐSS et al., 2012).

A 3D numerical steady-state flow model of the study area (POYANMEHR, 2013) has quantified that the younger waters firstly originated from the recharge or uncovered carbonate area (19% of the total infiltrated water) and secondly from the edge of the covering sediments (5% of the total infiltrated water). Based on the 3D steady-state model, 40% of infiltrated water in aquitard cover layers (between the surface and –500 m a.s.l. elevation interval) flows toward the karst system through the edge of the cover layer *(Figure 5).*

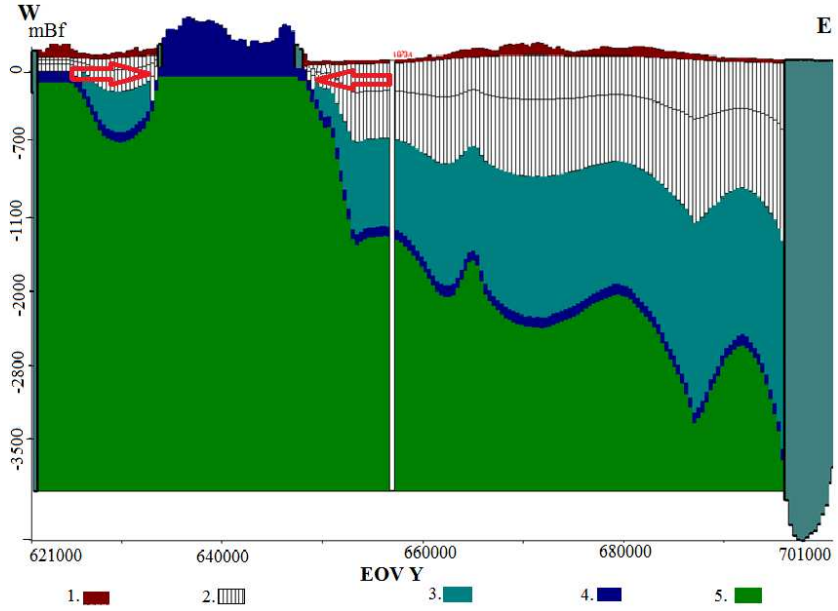

Figure 5. Scheme of infiltrated water of the aquitard layer flow toward the karst system through the edge of the aquitard layer (shallower than –500 m); 1. water-table bearing layer; 2. aquitard cover layer shallow than –500 m; 3. aquitard cover layer deeper than –500 m; 4. karst layer; 5. Not karstified rocks. Arrows show the contact area of aquitard layer shallower than –500m with the main karst, where 40% of infiltrated water of cover layers flows toward the karst thermal waters (POYANMEHR, 2013).

So based on the 3D model, depletion of heavy isotopes in south wells resulted in the flow of younger water through the edge of cover layers to the karst thermal system. This confirms the result of radionuclides research in the South Zone, which

suggested the entering of another fluid component into the karst waters. The sensitivity of the thermal system to infiltrated pollution through the upper edge of the covering sediments was also confirmed.

The relation between chloride concentration (meq/l) and the ^{18}O δ value of the Central Zone wells is represented in *Figure 6.* In the Central Zone chloride concentration decreased, while heavy oxygen isotopes increased along the mixing direction toward the spring *(Figure 6).* This indicates the mixing of ascending regional old water, depleted in heavy oxygen isotopes and higher Cl^- concentration, with younger water enriched in heavy oxygen isotopes and lower Cl^- concentration. The latter belongs to the shallow intermediate flow.

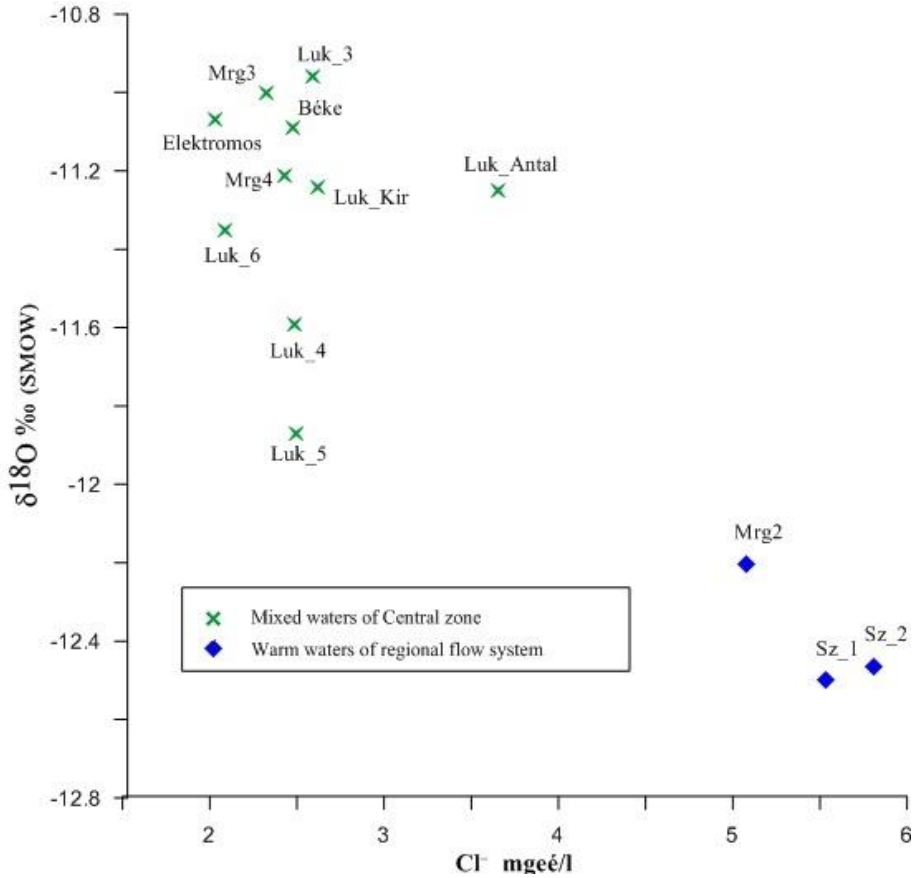

Figure 6. Relation between Cl^- and $\delta^{18}O$ (SMOW) in mixing direction

The mixing ratio in two places was calculated along the mixing line:

- Margitsziget 2 well (Mrg2)
- Lukács–Király spring (Luk_Kir)

4. MIXING IN THE MARGIT 2 WELL

To calculate the mixing ratio, two end members were needed, represented by two water samples belong to different flow paths. The first end member, which represents the old regional flow path, is Széchenyi 2 well (located in the eastern part of the Danube River). For the second end member the Piliscsaba well (located in the western highlands) is chosen, which represents the fresh infiltrated water belonging to the shallow intermediate flow.

Table 1

Geochemical composition of samples which used to calculate the mixing ratio

Wells	T °C	Na^+ mg/l	Ca^{2+} mg/l	Mg^{2+} mg/l	Cl^- mg/l	SO_4^{2-} mg/l	HCO_3^- mg/l	δ^2H ‰	$\delta^{18}O$ ‰
Margit 2 (Mrg2)	68.00	159.0	154.3	37.3	180	194.9	557.55	–90.0	–12.20
Széchenyi 2 (Sz_2)	72.60	175.0	149.5	36.0	206	204.0	561.20	–93.7	–12.46
Lukács–Király (Luk_Kir)	40.05	96.6	150.7	41.8	92.7	172.8	540.50	–79.6	–11.24
Piliscsaba	12.00	17.6	83.0	38.8	7	69.0	393.00		
Pilisszentiván	11.10	30	112	50	38	162	336	–74	–10

Considering the conservative Cl^- ion in the two end members (Piliscsaba with 7 mg/l and Széchenyi 2 with (206 mg/l) the proportion of the two end members in the Margit well (180 mg/l) was 13:87%. The mixing ratio based on the temperature supported this ratio (8–92%) as well.

The stable isotope data were also appropriate to calculate the mixing ratio. Stable isotope data of the Margit 2 well ($\delta^{18}O$: –12.2 ‰, δD: –90‰) and Széchenyi 2 ($\delta^{18}O$ –12.5 ‰, δD –93.7‰) were measured but the stable isotope in Piliscsaba was not available. Therefore, to calculate the stable isotope of the Piliscsaba well, data of a nearby well (Pilisszentiván) was considered and adjusted with respect to the height difference. This resulted in a calculated oxygen and deuterium concentration for Piliscsaba of $\delta^{18}O$ –10‰ and δD –74‰ (DEÁK, personal communication). Based on these values the mixing ratio in the Margit 2 well was about 10:90 or 15:85.

5. MIXING RATIO IN THE LUKÁCS–KIRÁLY SPRING

Temperature and chemical composition of several wells of the Lukács group were significantly different from the other members of the group. The possibility of mixing and the existence of a warmer and geochemical composition-rich component were confirmed. Mixing ratio was computed in one of the warm members of the Lukács group, the Lukács–Király spring. The conservative Cl^- ion concentration of the Lukács–Király spring (92.7 mg/l) suggested a mixing ratio of 43:57% of the two end members: the Széchenyi 2 well (206 mg/l) and the Piliscsaba well (7 mg/l). Temperature data also indicated a mixing ratio of 47:53%.

The oxygen and deuterium isotope content of the Lukács–Király spring are listed in *Table 1*. The two end members, as in the previous case, are the Széchenyi 2 and Piliscsaba wells. The isotope content of the Piliscsaba well is computed and adjusted data. The mixing ratio using $\delta^{18}O$ –10‰ and δD –70‰ in the Piliscsaba well was about 50:50% or 41:59%.

The mixing ratios computed from Cl^- concentrations and temperatures were close to each other, but the ratio calculated from the stable isotope δ values were different. In this case, possibly, the estimated isotope δ values of the Piliscsaba well were not appropriate for the mixing calculation. Mixing ratios in the Lukács–Király spring showed a significant increase in the proportion of the cold end member in Lukács–Király spring, comparing to the Margit 2 well (Mrg2). The increasing proportion of colder water along the flow path was indicated.

6. CONCLUSION

The accuracy of different flow paths reported earlier was verified by the evaluation of water geochemistry. The results of the geochemical analysis of thermal waters proved the increasing presence of younger water along the flow path from the Széchenyi wells toward the thermal springs (10% to near 50%) in the Central Zone of Budapest. The young waters originated from both the uncovered carbonate area (recharge area) as intermediate flow system and from the edge of the covering sediments. Because of this, the sensitivity of thermal springs in the Central zone of Budapest to infiltrated pollution is shown.

The probability of upward flow from south of Budapest (Csepel 2 well) toward the thermal springs (Gellért springs) was confirmed by the geochemical analysis of waters of south Budapest.

ACKNOWLEDGEMENTS

The author is deeply grateful to Dr. Irén Varsányi Zoltánné, Dr. János Szanyi and Máté Osvald for their suggestions, comments, and reviews regarding the manuscript.

REFERENCES

[1] ALFÖLDI et al. 1968
ALFÖLDI, L.–BÉLTEKEY, L.–BÖCKER, T.–HORVÁTH, J.–KESSLER, H.–KORIM, K.–ORAVECZ, J.–SZALONTAI, G.: *Budapest hévizei* (Thermal waters of Budapest) [in Hungarian]. VITUKI, Budapest, 1968, 365 p.

[2] ALFÖLDI et al. 1978
ALFÖLDI, L.–DEÁK, J.–LIEBE, P.–LORBERER, Á.: Connection of cold and warm karstic water resources in the Hungarian Central Mountains with special reference to draining efforts of mining (in Hungarian). *Proceedings of resarach activity of VITUKI.* Report series (1976–1977) 3.15. 1978, 300–317.

[3] ALFÖLDI 1979
ALFÖLDI, L.: Budapesti hévizek (Thermal waters of Budapest) [in Hungarian]. *VITUKI Közlemények*, 20, 1979, 1–102.

[4] ALFÖLDI 1981
ALFÖLDI, L.: A budapesti geotermikus áramlási rendszer modellje (Model of the geothermal flow system in Budapest) [in Hungarian]. *Hidrológiai Közlöny*, 61(9), 1981, 397–403.

[5] ALFÖLDI 1982
ALFÖLDI, L.: A layered thermal-water twin flow system. *J Hydrol,* 56, 1982, 99–105.

[6] BARBIDORICS–FÓRIZS– PAPP 1998
BARBIDORICS, J.–FÓRIZS, I.–PAPP, S.: Isotopic hydrogeological study of the thermal karst system in the Buda Mountains, Hungary. *RMZ – Material and Geoenvironment,* Vol. 45, No. 1–2, 1998, 8–12.

[7] CRAIG 1961
CRAIG, H.: Isotope variations in meteoric waters. *Science,* Vol. 133, 1961, 1702–1703.

[8] DEÁK 1978
DEÁK, J.: Environmental isotopes and water chemical studies for groundwater research in Hungary. *Isotope Hydrology,* Vol. I. IAEA-SM-228/13, 1978, 221–249.

[9] DEÁK et al. 1996
DEÁK, J.–DESEÖ, E.–BÖHLKE, J. K.–RÉVÉSZ, K.: Isotope hydrology studies in the Szigetköz region, northwest Hungary in. *Proceedings Series. Isotopes in water resources 127 management.* International Atomic Energy Agency, Vienna. IAEA-SM-336/15, 1996, 419– 432.

[10] ERŐSS–MÁDL-SZŐONYI–CSOMA 2008a
ERŐSS, A.–MÁDL-SZŐONYI, J.–CSOMA, É. A.: Characteristics of discharge at Rose and Gellért Hills, Budapest, Hungary. *Cent. Eur. Geol,* 51, 2008, 267–281.

[11] ERŐSS–CSOMA– MÁDL-SZŐNYI 2008b
ERŐSS, A.–CSOMA, É. A.–MÁDL-SZŐNYI, J.: The effects of mixed hydro-thermal and meteoric fluids on karst reservoir development, Buda Thermal Karst, Hungary. In: SASOWSKY, I. D.–FEAZEL, C. T.–MYLORIE, J. E.–PALMER, A. N.–PALMER, M. V. (eds.): *Karst from recent to reservoirs.* Karst Waters Institute, Spec Publ 14, Leesburg, VA, 2008, 57–63.

[12] ERŐSS et al. 2012
ERŐSS, A.–MÁDL-SZŐNYI, J.–SURBECK, H.–HORVÁTH, Á.–GOLDSCHEIDER, N.–CSOMA, A.: Radionuclides as natural tracers for the characteri-

zation of fluids in regional discharge areas, Buda Thermal Karst, Hungary. *Journal of Hydrology,* 426–427, 2012, 124–137.

[13] GOLDSCHEIDER et al. 2010
GOLDSCHEIDER, N.–MÁDL-SZŐNYI, J.–ERŐSS, A.–SCHILL, E.: Review: Thermal water resources in carbonate rock aquifers. *Hydrogeology Journal*, 18, 2010, 1303–1318.

[14] HAAS et al. 1989
HAAS, J.–TÓTH-MAKK, Á.–ORAVECZ-SCHEFFER, A.–GÓCZÁN, F.–ORAVECZ, J.–SZABÓ, I.: Alsó-triász alapszelvények a Dunántúli-középhegységben (Lower Triassic key sections in the Transdanubian Central Range) [in Hungarian]. *Földtani Int. Évk.,* 65(2), 1989.

[15] KORPÁS 1981
KORPÁS, L.: Oligocene-Lower Miocene formations of the Transdanubian Central Mountains in Hungary. *MÁFI Évkönyv,* 64, 1981.

[16] KORPÁS–LANTOS–NAGYMAROSY 1999
KORPÁS, L.–LANTOS, M.–NAGYMAROSY, A.: Timing and genesis of early marine caymanites in the hydrothermal palaeokarst system of Buda Hills, Hungary. *Sedimentary Geology*, 123, 1999, 9–29.

[17] LORBERER 2002
LORBERER, Á. et al.: A budapesti termálkarszt állapot-értékelése (Status reviews about the thermal karst water of Budapest) [in Hungarian]. *VITUKI final report.* 2002.

[18] POYANMEHR 2013
POYANMEHR, Z.: Conceptualization and implementation of an integrated regional groundwater model for Budapest cold-thermal karst system, Hungary. *Central European Geology Journal*, 56(4), 2013, 359–380.

[19] SÁRVÁRY 1995
SÁRVÁRY, I.: A budapesti termálkarszt kitermelhető vízkészleteinek felülvizsgálata (Review of exploitable resources of Budapest thermal karst waters) [in Hungarian]. *Hidrológiai Közlöny,* Vol. 75, No. 2 (1995), 87–93.

[20] TÓTH 1962
TÓTH, J.: A theory of groundwater motion in small drainage basins in central Alberta, Canada. *J Geophys Res,* Vol. 67, No. 11 (1962), 4375–4387.

[21] TÓTH 1963
TÓTH, J.: A theoretical analysis of groundwater flow in small drainage basins. *J Geophys Res,* 68, 1963, 4795–4812.

Geosciences and Engineering, Vol. 4, No. 7 (2015), pp. 32–44.

MINING AND EVALUATION OF SHALE RESERVOIRS

KRISTÓF HÍVES

Abstract: The role of unconventional hydrocarbons has increased rapidly in recent decades. This is the reason that our knowledge is also growing day by day. The aim of this article is to summarize the current state of knowledge about the most widespread unconventional reservoirs, shale gas and shale oil. This article describes the unconventional reservoir types, how they are mined, what kind of obstacles prevent their production, and how these problems could be solved. Next it introduces how the unconventional shale reservoirs appears during well logging. Both qualitative and quantitative evaluation methods are presented. These methods involve the determination of Total Organic Content (TOC) value and Gas Content (GC). Finally, demonstrated by a specific example, I investigated how much of these methods work in the practice. In this section I investigated and used the Passey method to evaluate a certain well in the USA.

Keywords: *unconventional, petrophysics, Passey method, TOC, shale gas, shale oil*

1. INTRODUCTION

Conventional hydrocarbons have gone through migration and accumulated in geometrically well-defined areas of structural or tectonic traps. The types of hydrocarbon to which this definition could not be applied are called unconventional [1]. In this case, migration does not take place and the reservoir is usually the same as the source rock. In this case hydrocarbon is produced from layers with very low porosity and permeability (< 0.1 mD). Various mining processes have been developed to improve these parameters: hydraulic fracturing, acidizing etc. Their extraction is generally more complex and more expensive than in the case of conventional reservoirs. The amount of unconventional hydrocarbons is one magnitude higher than that of the conventional ones. Huge locations can be found in many parts of the world, for example in the US, in Canada, Poland etc. However, due to its high costs, environmentally destructive impact and the various energy policies of some countries, production is not allowed in several parts of the world.

2. TYPES AND MINING OF UNCONVENTIONAL RESERVOIRS

There are several kinds of unconventional hydrocarbons:

- shale gas,
- shale oil,
- tar sand oil,
- tight sand or deep gas,
- coalbed methane,
- hydrocarbon hydrates.

This article deals with the first two types.

2.1. Shale gas

Shale gas is a type of natural gas that is trapped inside the micro pore system of shales. The gas can occur in very-low-permeability rocks, which means that these deposits need special methods for production and their production is likely to be more expensive than that of conventional deposits. There are huge amount of shale gas in the USA, Argentina, China etc. *(Figure 1).*

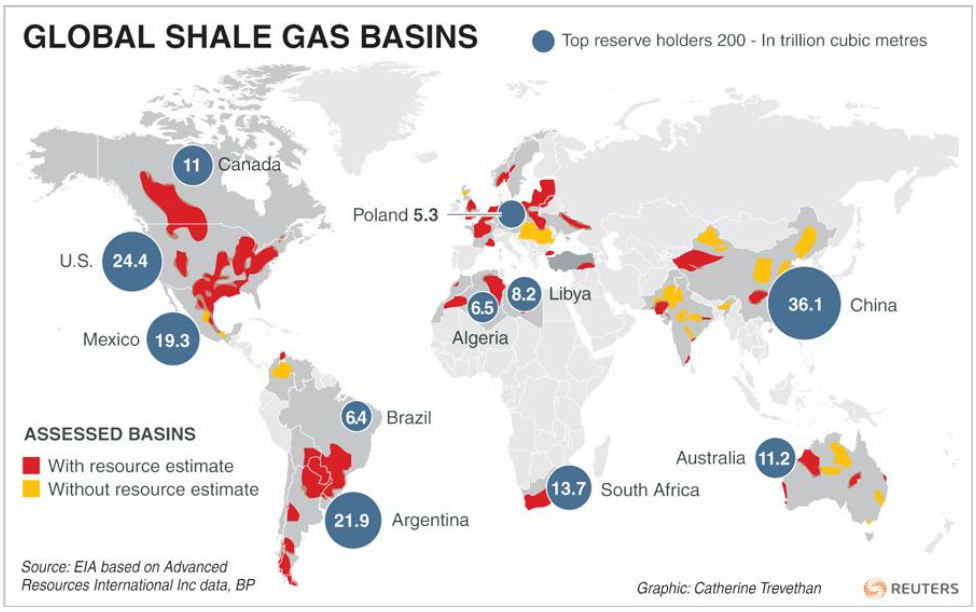

Figure 1. *Shale gas resources based on US Energy Information Administration (EIA) data*

Production:

Since shale is impermeable, its mining is not possible in traditional ways. This has prevented their production for decades. To solve this problem, two methods have been developed independently: one method is hydraulic fracturing, the other is horizontal drilling. With time, these methods were merged to create an effective and safe technology.

First, the shale layer is reached by vertical drilling, after this the direction of drilling is altered to form a horizontal well. Following the drilling, high pressure fluid is injected into the shale (this process is called hydraulic fracturing). Of this fluid, 90% is water, 9.51% is sand, and the remaining 0.49% is other chemical substances. Some elements of the fluid help to keep the fractures open, which in turn helps gas to flow to the surface *(Figure 2).* After extraction of the gas, the pressure is reduced and the injected water returns to the surface [1].

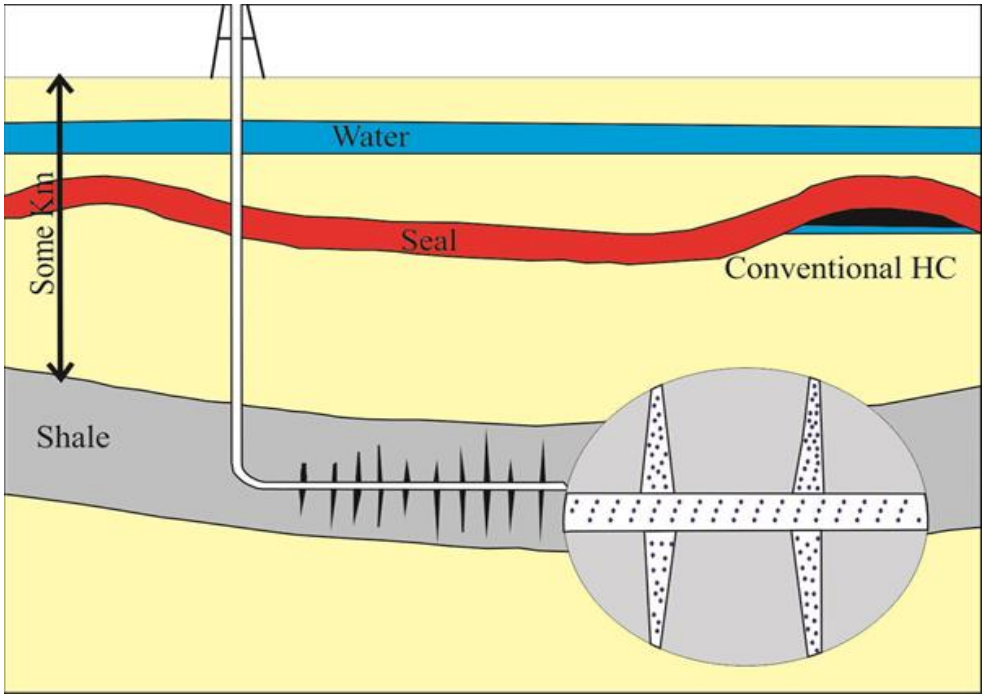

Figure 2. *Production of shale gas (Modified after [1])*

Shale gas extraction is currently ongoing, mainly in the USA. A huge advantage is that it takes place in a big territory, unlike conventional hydrocarbons, which are limited to are relatively small area. Therefore it is able to supply gas to a big region without building long pipelines, although a large number of wells are required. One well can produce gas in smaller yield but for a longer time than conventional wells. Finding unconventional hydrocarbons is relatively easy, but achieving commercial quantity is difficult.

2.2. Shale Oil

Shale oil is a type of unconventional crude oil that is produced from sedimentary rocks which contain large amounts of organic matter. This kind of hydrocarbon has not been buried deeply enough to make it possible for the hydrocarbons to be generated sufficiently. Therefore, anoxic treatment is required after the mining [2].

In this case, the entire body of rock (which is coevally sourcerock and reservoir rock) has to be brought to the surface. The excavated rock is grinded, after which it is delivered to large ovens in which the petroleum can be distilled. Distillation can be started at 300 °C, but is most effective at approximately 500 °C. Because of the large amount of the energy invested, the production in many cases is not economical.

Recent research has suggested that the source rock should be heated before the mining and specialized heating tubes should be employed in the wellbores. Thus, the oil could be separated from the rock deep under the surface and then the oil could be produced in the conventional way *(Figure 3).* This would provide a cheaper and more effective mining method [1].

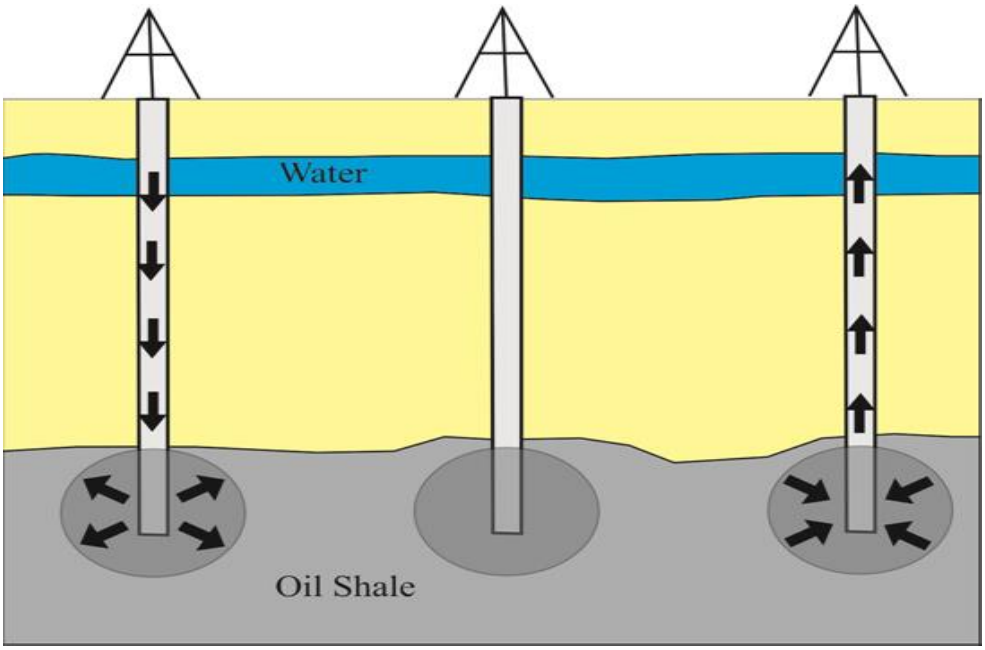

Figure 3. *Suggestion for the shale oil production (Modified after [1])*

3. WELL LOGGING

How does unconventional hydrocarbon appear in logs? Because of the organic content, we could assume high resistivity, high transit time on sonic log, low density, high neutron porosity and high gamma radiation. This idea is not far from the reality [3], [4].

Most of the conventional logs can be used in unconventional cases, although not all of them are effective. Generally, the following probes are used: resistivity, density, neutron, PE, sonic, natural gamma ray (intensity), spectral gamma, temperature, borehole camera and NMR.

Temperature measurement could be also very useful in shale gas exploration, especially in the case when a small amount of gas reaches the wellbore prior to the measurement. In this case, we will get an easily recognizable anomaly compared to the geothermal gradient.

Gamma ray is less effective in unconventional gas exploration. In some cases, spectral gamma logging may help in the evaluation. Examination of the uranium

content can be useful if the sediment formed in a marine environment. The uranium content is in connection with the total organic content (TOC = total organic content or total organic carbon). However, a general lack of uranium content can be observed in cases where the sedimentation took place in a lacustrine environment. In this case, the total gamma ray should be used, which shows only the shale content Vsh [5].

In organic-rich shale, the resistivity is higher than the average. We can infer the amount and the maturity of the organic matter from the size of the resistivity anomaly. Resistivity also provides information about other rock forming minerals (for example, the amount of pyrite).

As the organic material has low density, it will have a significant impact on the bulk density log. If the other parameters of the rock do not change, then the bulk density is in accordance with the total organic content (TOC).

P and *S* waves are both useful to detect hydrocarbon in shale formation, but mainly the *P* wave is used. The *P* wave moves at a lower speed in organic matter (increased transit time), because of this it can let us know the amount of total organic content [3].

Neutron-porosity measurement: if the unconventional hydrocarbon layers are rich in clay, the hydroxide ion of the clay masks hydrocarbon content. Thus, the neutron logs are only useful in layers with low clay content.

All porosity logs are very useful in unconventional hydrocarbon exploration, especially if it is combined with resistivity logs. It can help us to evaluate the amount of TOC. Some other methods such as temperature, gamma ray or borehole image logs can be also useful.

4. VISUAL ANALYSIS OF TOC

Two qualitative methods were developed to examine the total organic content of the rocks. In the first method the possible source rock will show crossover between the sonic and the resistivity curves. In the second method we use a crossplot of resistivity and one porosity measurement to define and segregate organic rich layers from other layers.

The analysis is based on the porosity-resistivity technique which was presented by PASSEY [3], [4]. With this technique reservoir rocks, mother rock, coal seam etc. can be easily distinguished. If we use this method in a more radioactive zone, organic rich shales can be identified.

The resistivity curve is plotted on a logarithmic scale, next to the sonic curve. The two curves are matched in a known (or assumed) non-source rock. The place of the matching should be as close as possible to the investigated shale layer. Because of the organic content the resistivity becomes higher, and the sonic velocity becomes slower in the mature source rock. Are recognizable crossover can be seen at the mature source rock *(Figure 4).* The absolute value of the sonic and resistance for shale rock is called the base line (it is similar to the clay line in conventional case). This base line will change proportionally to depth and the burial time [6].

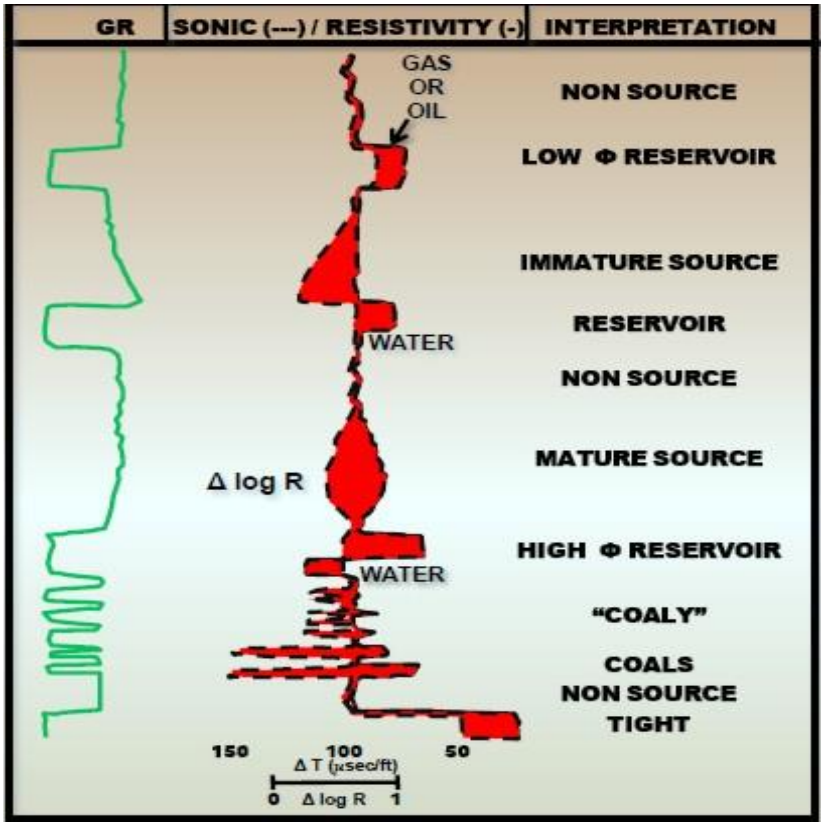

Figure 4. *Separation of source rock from non-source rock [6]*

ΔlogR method: A method is also described by Passey in which a porosity and a resistivity curve are used.

First, the resistivity logarithm is depicted in the coordinate system *x,* the result of sonic or neutron measurements on the *y* axis (density measurement can be also sufficient). Then the point on the bottom left corner of the figure indicates carbonate rock, whereas in the upper right corner there are shales *(Figure 5).* There is a dividing line which separates the cluster of source rock from non-source rock. From the coordinate system we can determine the gradient and the intercept of this line, thus we can calculate a pseudo sonic log DtR. (**DtR = y–m*logR** where *y* is the intercept and *m* is the gradient of the "shale line".)

The resulting DtR curve should be plotted next to the original sonic curve. Thus, there will be a crossover in the potential hydrocarbon layer, similarly to the first method. In the case of organic matter content the original sonic log will be on the left side of the crossover, and the right side is the DtR curve *(Figure 6).* The reason for this is that the original DT value is larger than the calculated DtR value in shale rocks whereas it is the inverse in other rocks.

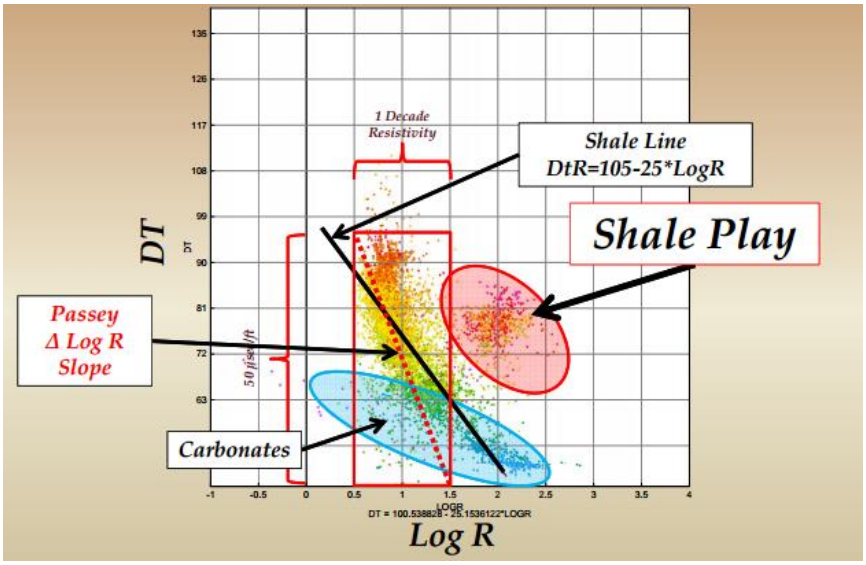

Figure 5. *The shale line and the determination of DtR [7]*

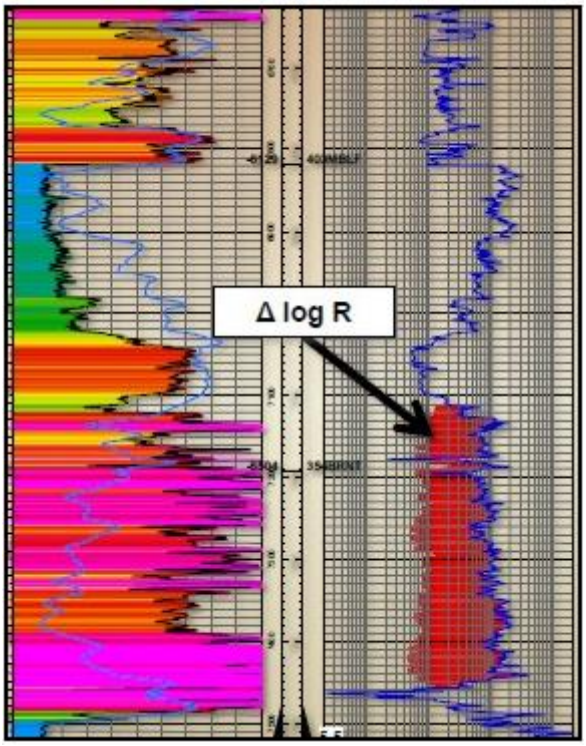

Figure 6. *Crossover because of organic content (Barnett Oil Play) [8]*

5. QUANTITATIVE DETERMINATION OF TOC (PASSEY ΔLOGR METHOD)

Petrophysics and geophysicists have shown that there is a correlation between porosity logs (sonic, neutron and density) and TOC. There are many ways to estimate the TOC value from logs. Two of this will be described below. The most common is the **ΔlogR** method. Here a deep penetration resistivity and a porosity log are used. With the simple equation these logs can be transformed directly to TOC if the level of maturity is known:

$$\Delta\text{logR}\ (\Delta t) = \log\ (R/R_{base}) + 0{,}02*(\Delta t - \Delta t_{base})$$

$$\Delta\text{logR}\ (den) = \log\ (R/R_{base}) - 2{,}5*(\rho - \rho_{base})$$

$$\Delta\text{logR}\ (n) = \log\ (R/R_{base}) + 4{,}0*(\Phi_N - \Phi_{Nbase})$$

$$TOC = \Delta\text{logR}*10\text{^}(2{,}297 - 0{,}1688*LOM)$$

where ΔlogR Passey numbers (from sonic, density and neutron logs)
R – deep penetration resistivity in the examined zone
R_{base} – deep penetration resistivity in the baseline
Δt, ρ, Φ_N – sonic, density and neutron values in the examined zone
Δt_{base}, ρ_{base}, Φ_{Nbase} – sonic, density and neutron values in the baseline
LOM – level of maturity; it ranges from 6 to 14; for gas it equals 8.5; for oil 10.5

Any Passey number can be placed in the fourth equation. In practice the "level of maturity" originates from core data. Vitrinite reflectance could be very useful to obtain this value. In case the LOM is incorrectly calculated the absolute value of TOC will be false, but the vertical variability of organic content will be correctly represented.

5.1. TOC calculated with a spectral gamma log

The uranium content is related to the kerogen. Unfortunately, a spectral gamma log is not available in many cases. The following equation can be used if we have access to a spectral gamma log:

$$TOC = SF_{uran}*\log(URAN/4)$$

where SF_{uran} – uranium factor, which ranges from 0.02 to 0.08
URAN – uranium content, counted in ppm

The total organic content alone is not very useful forus. If TOC is calculated then we can calculate Gas Content: GC = K * TOC
where GC = gas content (scf/ton)
K = gas factor (range5–15)–

6. PRACTICAL EXAMPLES: BARNETT SHALE

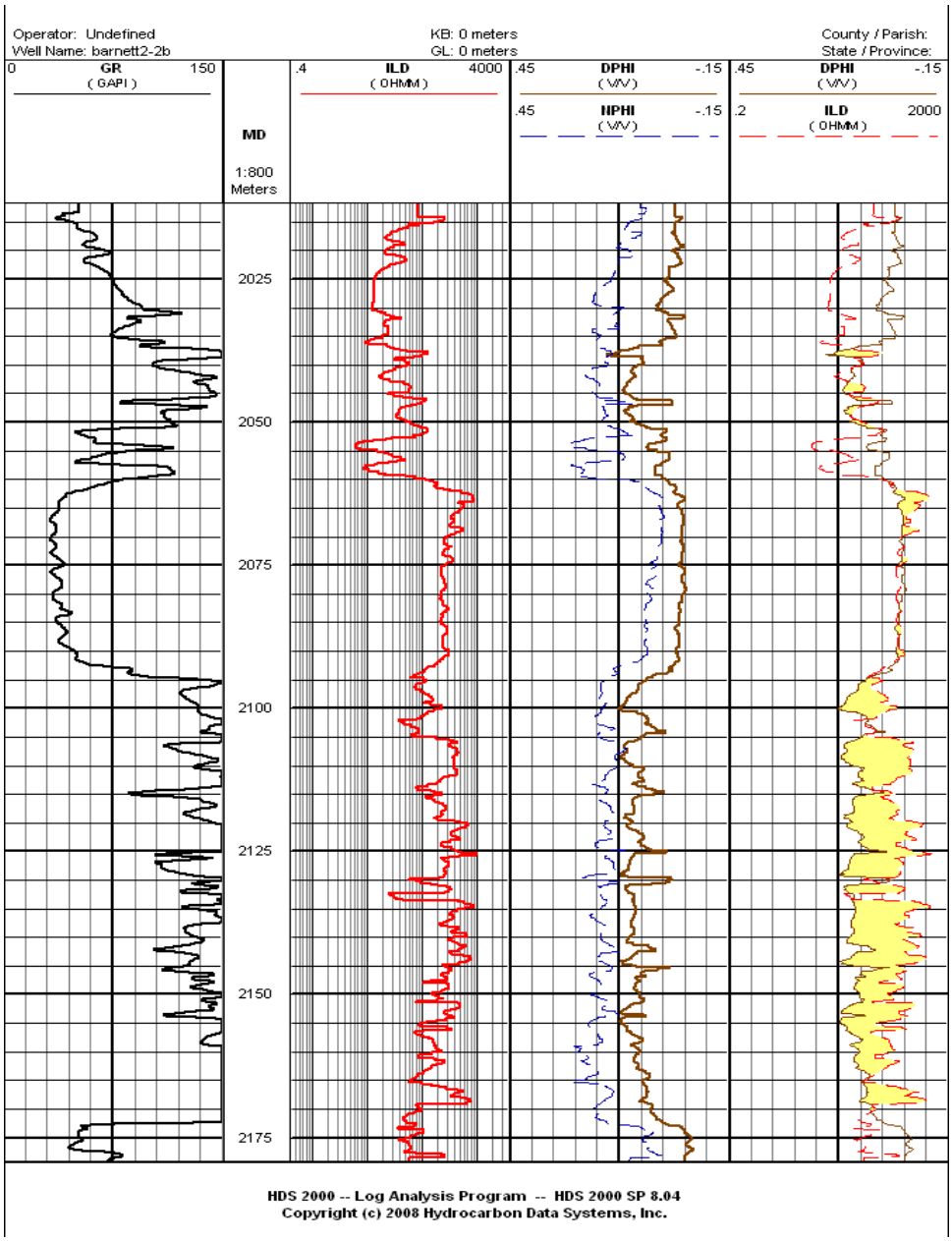

Figure 7. *Visual evaluation of Barnett Shale (Modified after [9])*

I tested the evaluation methods in an American example. I examined a well where both core data and well logs are available in order to check whether the core data is in good agreement with the calculated values.

No sonic curves were available, so I used density logs instead. There was a deep induction log. In a low resistivity zone the induction probes are not as reliable as the direct current probes. The scale of the density is linear, whereas the induction is logarithm.

We can assume from crossover that between 2095 and 2170 meters there is an organic rich layer *(Figure 7).* In this zone the gamma ray also shows a high value. We know from core data that it is a shale layer which is rich in organic content [9]. Above this there is a limestone layer with low gamma values and there is no crossover. The lack of crossover can indicate a relatively small amount of organic content. Another shale layer is between 2035 and 2060 m, appears to have lower organic content than the first one, and in the top there is a limestone layer.

It is apparent on the figure that in the shale layer the gamma ray is higher, and it fluctuates more heavily than in limestone. This fluctuation comes from the texture of the shale. This sedimentary rock is characterized by breaks along thin laminate or parallel layering. The resistivity value of the induction measurements is substantially lower than that of the upper shale layer. This can refer to the amount of organic content or its maturity. Pyrite content or salinity could also be a reason for this low resistivity.

In the crossplot *(Figure 8),* the x axis contains the resistivity values in logarithmic scale and the y is for the porosity, which was calculated from density log. I could select a shale line because the shale point is not clearly distinguished from other points.

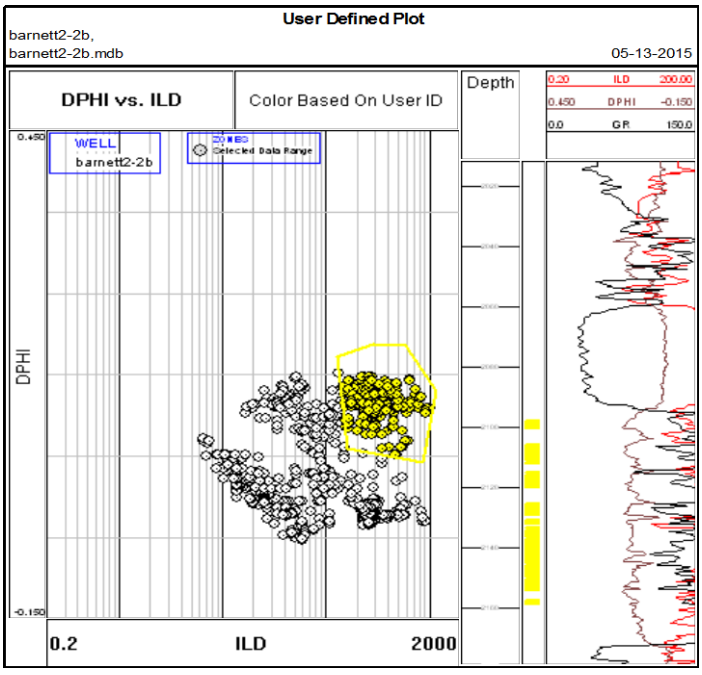

Figure 8. *Crossplot from Barnett Shale*

Numerical evaluation:

Table 1
Numerical evaluation

DEPTH	GR	ϕ_N	ϕ_D	ILD	ΔlogR	TOC	V_{sh}
2015.0	46.812	0.094	–0.007	123.712	0.093	0.311	0.096
2022.5	63.231	0.137	–0.010	32.947	–0.310	–1.038	0.218
2030.0	88.461	0.201	0.031	13.487	–0.443	–1.482	0.406
2037.5	109.930	0.198	0.068	39.039	0.007	0.025	0.567
2045.0	139.514	0.213	0.125	45.076	0.129	0.432	0.787
2052.5	78.508	0.180	0.052	75.967	0.223	0.746	0.332
2060.0	95.687	0.204	0.034	73.871	0.310	1.038	0.460
2067.5	35.440	0.036	–0.025	415.683	0.389	1.301	0.011
2075.0	36.729	0.052	–0.023	280.316	0.280	0.939	0.020
2082.5	39.549	0.074	–0.018	253.583	0.325	1.087	0.041
2090.0	45.493	0.079	–0.013	265.300	0.363	1.216	0.086
2097.5	130.058	0.199	0.112	116.108	0.485	1.624	0.717
2105.0	139.298	0.177	0.088	200.127	0.635	2.126	0.786
2112.5	148.957	0.193	0.088	248.059	0.791	2.646	0.858
2120.0	146.257	0.179	0.117	394.078	0.935	3.130	0.838
2127.5	121.042	0.183	0.118	269.716	0.786	2.631	0.650
2135.0	143.842	0.207	0.108	505.420	1.156	3.869	0.820
2142.5	123.327	0.184	0.101	532.384	1.087	3.638	0.667
2150.0	142.675	0.198	0.101	285.939	0.874	2.925	0.811
2157.5	149.027	0.226	0.102	154.671	0.716	2.396	0.858
2165.0	161.730	0.205	0.075	235.481	0.815	2.727	0.953
2172.5	77.319	0.111	–0.013	69.225	–0.091	–0.304	0.323

I applied the Passey formulas and calculated TOC number.

$$\Delta\log R\ (n) = \log\ (R/R_{base})+4{,}0*(\Phi_N–\Phi_{Nbase})$$
$$TOC = \Delta\log R*10\text{^}(2{,}297–0{,}1688*LOM)$$

During my calculation the base value for resistivity was 150 Ωm, and 0.5 for neutron porosity. The base value was chosen to be the upper zone average resistivity

and the neutron porosity at 2070 m. These layers seem to be poor in organic content until 2090 m, so they are good choice for base values.

I counted the shale value (Vsh) from gamma ray and highlighted the shale layers with gray. As the Passey technique was developed for shale layers, the result of ΔlogR calculate is reliable in these layers. The TOC value from 2067 to 2090 m could be the result of the relatively high resistivity of the limestone, whose high organic content is questionable. Density and neutron porosity also supply this conclusion.

The low resistivity of the upper shale refers to low TOC values. However, the lower shale layer is likely to have significant organic content. The resistivity, neutron and density porosity confirm this as well.

7. SUMMARY

During my research I proved that the porosity values are in close connection with the TOC. In the case of an organic-rich shale zone the density was lower than in other layers, thus its porosity appears to be higher. The neutron porosity also increases. The rock resistivity generally shows greater values. The gamma ray shows in general which the considered shale layers are. If spectral gamma measurement is carried out, we could infer TOC from uranium content. I haven't examined sonic logs, but according to Passey the transit time is increasing in shale reservoirs.

The Passey's ΔlogR method worked well in my example. I managed to calculate reliable values for TOC in the correct layer. However, I could not select the shale line in my studied example. As I was unable to distinguish the shale point from other rocks on the crossplot, it t was not a useful method in this case.

ACKNOWLEDGEMENTS

The author is grateful to Mihály Dobróka, Anita Jobbik and László Balázs for their constructive remarks and improvement of the manuscript.

LIST OF SYMBOLS

Symbol	Description	Unit
ΔlogR	Passey numbers (from sonic, density and neutron logs)	–
R	deep penetration resistivity in the examined zone	Ωm
R_{base}	deep penetration resistivity of the baseline	Ωm
Δt	sonic velocity in the examined zone	μs/ft
Δt_{base}	sonic velocity at the baseline	μs/f
ρ	density in the examined zone	kg/m^3
ρ_{base}	density at the baseline	kg/m^3
Φ_N	neutron porosity in the examined zone	–
Φ_{Nbase}	neutron porosity in the baseline	–
LOM	Level of maturity	

Symbol	Description	Unit
SF_{uran}	uranium factor	–
URAN	uranium content	ppm
GC	gascontent	scf/ton
K	gasfactor	–

REFERENCES

[1] NÉMETH 2012
NÉMETH, B.: *Ipari technológiák: Energiahordozók nem hagyományos bányá-szata*. 2012.
http://www.physics.ttk.pte.hu/pages/munkatarsak/nemetb/IT-3-Energiahordozok-nem-hagyomanyos-banyaszata-NB.pdf

[2] BJORLYKKE 2010
BJORLYKKE, K.: From Sedimentary Environments to Rock Physics. *Petroleum Geoscience,* 2010.

[3] PASSEY et al. 2010
PASSEY, Q. R.–BOHACS, K. M.–ESCH, W. L.–KLIMENTIDIS, R.–SINHA, S.: From Oil Prone Source Rock to Gas-Producing Shale Reservoir-Geologic and Petrophysical Characterization of Unconventional Shale-GasReservoirs. *Exxon Mobil Upstream Research Co.,* 2010, 13–17.

[4] PASSEY et al. 1990
PASSEY, Q. R.–CREANEY, S.–KULLA, J. B.–MORETTI, F. J.–STROUD, J. D.: Practical Model for Organic Richness from Porosity and Resistivity Logs. *AAPG Bulletin*, 1990, 74, 1777–1794.

[5] CRAIN 2015
CRAIN, E. R.: Special cases: Gasshale. *Crain's petrophysical handbook.* 2015. https://spec2000.net/17-specshgas.htm

[6] CRAIN 2015
CRAIN, E. R.: Total organic carbon (TOC). *Crain's petrophysical handbook.* 2015. https://spec2000.net/11-vshtoc.htm

[7] MEYER–NEDERLOF 1984
MEYER, B. L.–NEDERLOF, M. H.: Identification of Source Rocks on Wireline Logs by Density-Resistivity and Sonic-Resistivity Crossplot. *AAPG Bulletin*, Vol. 68, 1984, 121–129.

[8] BOWMAN 2010
BOWMAN, T.: Direct Method for Determining Organic Shale Potential from Porosity and Resistivity Logs to Identify Possible Resource Plays. *Search and Discovery*, 2010.

[9] ZHAO–GIVENS–CURTIS 2007
ZHAO, H.–GIVENS, N. B.–CURTIS, B.: Thermal maturity of the Barnett Shale determined from well-loganalysis. *AAPG bulletin*, 2007.

Geosciences and Engineering, Vol. 4, No. 7 (2015), pp. 45–58.

ESTIMATING LANDSLIDE SUSCEPTIBILITY FOR THE CARPATHIAN REGION USING GIS MODELING APPROACH

ENDRE DOBOS–ANDRÁS HEGEDŰS–JÁNOS VÁGÓ

Institute of Geography and Geoinformatics, University of Miskolc
Miskolc-Egyetemváros, 3515 Hungary
ecodobos@uni-miskolc.hu

Abstract: Landslide mapping and inventories are not available in the same format for all European countries. Several attempts have been made to collect and harmonize the available landslide data sources. However, no consistent inventory is available for the Carpathian region. Modeling is the only comprehensive approach that provides information on landslide risk, hazard and susceptibility. An existing method has been generalized and modified here to fit the whole Carpathian region. Five environmental factors were integrated into the model: slope, local relief (derived from an SRTM image), land use (developed from a multitemporal MODIS image), lithology (from the European Soil Database) and the expected daily maximum precipitation, which was derived from the CLAVIER database. These factors have been classified and weights were specified for each factor and class based on an expert knowledge approach. The model was run for the whole Carpathian region for the period 1951–2050, and also by splitting the dataset into two periods, namely the years between 1971–2000 and 2021–2050 and a comparison was performed to characterize the climate change impact. The results show that the Carpathian region in general is severely impacted by landslides, because the environmental conditions of the area favor their development. More than 65% of the entire area is classified as medium, high and very high susceptibility classes. The high and very high susceptibility areas are located mainly in the outer bend of the Northwestern Carpathians, namely the flisch zone of the North-Eastern and Eastern Carpathians, the Bend Carpathians, the Banat Mountains and the Apuseni Mountains. These are the areas where slopes exceed 12–15 %, and the lithology consists of sedimentary rock formations – mainly Carpathian flisch having sandstones with intercalated clay bands – and clayey Pannonian sediments in the lower lying areas, like in the Transylvanian depression. Slope and lithology have been found to be the most significant factors in the indication of landslide probability.

Keywords: *landslide, CARPATHCC, GIS modeling*

1. INTRODUCTION

A landslide is defined in the ENVASSO Glossary of Key Terms [1] as: 'the movement of a mass of rock, debris, artificial fill or earth down a slope, under the force of gravity, causing a deterioration or loss of one or more soil functions' [2]. There are many different types of landslides, and their classifications are complex and sometimes contradictory [3]. However, there is a general consensus that mass movements can be classified according to their mode of failure. CRUDEN and VARNES [2] classify the types of failures as follows:

I. slides – rotational or translational mass displacements with limited internal deformation, and relatively uniform velocity profiles;
II. flows – associated with relatively high moisture contents, and with non-uniform velocity profiles, reflecting frictional effects between the base of the flow and the in-situ ground;
III. falls – slope displacement that are principally vertical in nature;
IV. topples – slope displacements with both lateral and vertical components;
V. lateral spreads – slope displacements that are primarily horizontal;
VI. ground or frost-heave – associated with expansion/contraction of individual constituents of the slope material, which destabilizes the slope e.g. freeze/thaw; exfoliation.

Europe and the Carpathians have been increasingly affected by landslides and flashfloods in the last few decades. One of the major reasons for this increase is believed to be climate change. Climate change and global warming have several recognizable effects on the spatial and temporal patterns of weather elements, like precipitation, temperature etc. There is common agreement that the spatial and temporal distribution of precipitation will be more extreme, with alternating severe rainstorms and drought periods. Severe rainstorms and extreme wet periods support the development of flashfloods and landslides. Therefore, the number of these events and their seriousness are likely to increase in the future. Any kind of prevention activity requires the understanding of their development processes and the major environmental factors that affects their spatial distribution and occurrence. Several initiatives have been launched all over Europe with different goals and methodologies in order to map the areas where these natural hazards may occur.

Several inventories of past landslide events have been compiled in the European countries. The first coherent report was made by HERVÁS [4], where examples of existing EU country inventories – Great Britain, Italy, Greece and Spain – were described and compared. There are more recent studies as well by GALLI et al. [5], HERVÁS and BOBROWSKY [6] and VAN DEN EECKHAUT and HERVÁS [7, 8]. The latter ones compiled a report on the status of landslide inventories for the EU countries. They concluded that the information available on this issue is still limited. As an example, only the Slovakian database can be considered more or less complete, while Hungary – where landslide susceptibility is lower – has a half-completed database. No information exists on a national database for either Romania or Ukraine. BALTEANU et al. [9] describe the Romanian situation in more detail. They mention several related mapping activities, but no complete accessible inventory is available, only small areas mapped within research projects [10, 11].

Landslide hazards can be expressed by different tools as well. The most common approach is the landslide susceptibility map, which shows the probability of landslide events in a certain area based on the existence of the most important contributing factors. These are usually the products of models. The most recent EU-wide assessments of landslide susceptibility were performed by GÜNTHER et al. [12] and HERVÁS [13].

Landslide susceptibility mapping has several published methodologies. HUBER et al. [3] listed a number of major factors increasing the vulnerability to landsliding. The factors of are summarised as: i) slope materials (texture, lithology, stratigraphy, angle of internal friction, cohesion); ii) slope steepness; iii) moisture content of slope materials (including pore water pressure); iv) rainfall and snowmelt contributing to slope instabilities, except some 'dry' slope failures e.g. rock falls and topples); v) temperature fluctuations (applies to snow melt, freeze/thaw processes, exfoliation); vi) seismic activity; vii) land use change (e.g. deforestation); viii) land management practices (e.g. over-grazing) ,and ix) evidence of previous landslides.

The static factors, like terrain, soil/geology, and land use can be used as common criteria for a continental, EU or regional coverage model. This approach was used in the ELSUS1000 model [12]. They reclassified the 3 input layers/factors into 5 classes each. Each of these factors and their classes was given a weight factor *(Table 1).*

These factors and weights were used to calculate the susceptibility index using the equation below.

$$S = \sum_{j=1}^{n=3} Wj * Xij$$

where *Wj* is the weight of criterion *j* and *Xij* is the weight of class *i* for criterion *j*. GÜNTHER et al. [12] concluded that landslide susceptibility can be successfully evaluated for the delineation of risk areas with limited environmental information. However, any synoptic analysis at the continental level can be supposed to give a biased overview on landslide susceptibility, since it does not consider specific landslide types or climato-physiographic settings.

BALTEANU et al. [9] assessed landslide susceptibility for Romania using six predicting factors *(Table 1).* Their model has much more detailed thematic resolution. The same set of variables was used together with three additional factors: seismicity, maximum rainfall within 24 hours, and local relief. The weights for the factors and their classes were established by expert judgement *(Table 1).*

The Romanian study gave much less weigh to the slope. Although they introduced local relief as a new terrain variable, even the sum of the weights of the two terrain related variables is less than half one of that used in the other study, for a total of 30 percent. On the other hand, lithology is taken as a most important factor with the highest weight. Due to the more detailed scale of the Romanian study, the number of classes within each of the factors was higher.

BALTEANU et al. [9] considered this map of landslide susceptibility of Romania as a preliminary step for more detailed susceptibility and hazard studies, as well as a useful tool for risk management. The model allows the identification of the most problematic areas where the development of detailed investigations and the application of mitigation measures would provide a better cost/benefit ratio.

Table 1
Comparison table for the weights used in the studies of GÜNTHER et al. [12] and BALTEANU et al. [9]. Numbers in brackets are the relative weights without the extra elements of seismicity and maximum rainfall. Local relief and slope are summed up as terrain related variables

Factor	Weight (%)	
	EU study by GÜNTHER et al.	Romanian study by BALTEANU et al.
Lithology (F1)	26	35 (46)
Slope (F2)	64	25 (40)
Maximum rainfall in 24 hours (F3)	–	15
Land use (F4)	10	10 (14)
Seismicity (F5)	–	10
Local relief (F6)	–	5

The current study aims to map landslide susceptibility and its changes due to the changing climate, and to forecast the magnitude and significance of this natural hazard for the Carpathian region. After considering several options for modeling landslide susceptibility, we decided to adopt the model of BALTEANU et al. [9] because it was developed and already adjusted to the Carpathian region. Unfortunately, no seismicity database was available for the project, therefore some necessary simplification was performed on the procedure.

2. MATERIALS AND METHODS

2.1. Study area and the data sets

The study area of the landslide susceptibility analysis was the entire Carpathian Region. Five input data layers were used to represent the controlling factors of landslides generation, namely lithology, slope, local relief, land use and precipitation. Each of them was resampled into a spatial resolution of 0,001° (~ 89 m).

2.1.1. Lithology layer

The information for the lithology raster was derived from the parent material layer of the 1:1 M scale European Soil Database (ESDB) [14]. This layer covers the whole of Europe, but its reliability and the resolution is inhomogeneous: the lithological data for Ukraine (NE Carpathians) is less detailed than in the other parts of the examined region. Therefore the Ukrainian part of the ESDB was refined using the geological map of Hungary compiled by Lajos Lóczy in 1922. The geological units of the ESDB and the digitized Lóczy map were reclassified into 10 lithological classes. The classification process was based on the method applied by BALTEANU et al. [9]. The main criteria for rating the lithological classes were the genesis of the geological formations (metamorphic, igneous or sedimentary rocks) and their geotechnical properties *(Table 2).*

Table 2
The lithological classes and their rating

Class names	**Rates**
Water body	0
Metamorphic and igneous formations	1
Limestones and dolomitic formations	2
Coarse cemented siliciclastic and/or volcanic formations	3
Alluvial formations covered by aeolian or colluvial deposits	4
Alluvial unconsolidated gravel formations	5
Aeolian or colluvial silty formations	6
Sandstones with secondary intercalations of marls and clays	7
Quasi-rhythmic clay and sandstone formations	8
Clays and marls with secondary intercalations of sandstones	9
Clay and marl formations	10

2.1.2. Terrain features

Two terrain features were added to the model, the slope and the relief intensity. These factors were derived from the SRTM data [15]. The slope was classified into 8 classes using the slope command of ArcGIS *(Table 3).* The local relief layer (also called relief intensity or amplitude of relief) reflects the topography of a wider area and relates to the capacity of moving loosened rock masses. This factor has a special importance in the case of landslides induced by earthquakes [16]. Relief intensity is calculated as the difference between the maximum and minimum elevation within a 1 km^2 area. *Table 3* shows the grading of the local relief classes within the landslide susceptibility model.

Table 3
Slope classes, local relief classes and maximum rainfall classes and their ratings

Slope		**Local relief**		**Maximum rainfall**	
Degrees	**Rating**	**Class (m/km^2)**	**Rating**	**Class (mm)**	**Rating**
0–2	0	0–30	2	< 100	2
2–5	2	30–70	4	100–150	5
5–8	4	70–150	7	150–200	8
8–12	6	150–250	10	> 200	10
12–15	8	250–500	8		
15–30	10	500–750	6		
30–45	7	> 750	4		
> 45	5				

2.1.3. Land use

The land use dataset was developed from the classification of a multitemporal MODIS image stack representing different periods of vegetation development *(Figure 1).* Images from April, July and September were integrated into one multi-channel image. Channels 1–4 were selected representing the visible and the near infrared spectra. Channels 1 and 2 (red and NIR) had an original resolution of 250 meters, while Channels 3 and 4 (blue and green) had a 500 meter resolution, but all channels were resampled to 500 meters. The final class set and grades defined by BALTEANU et al. [9] are listed in *Table 4.*

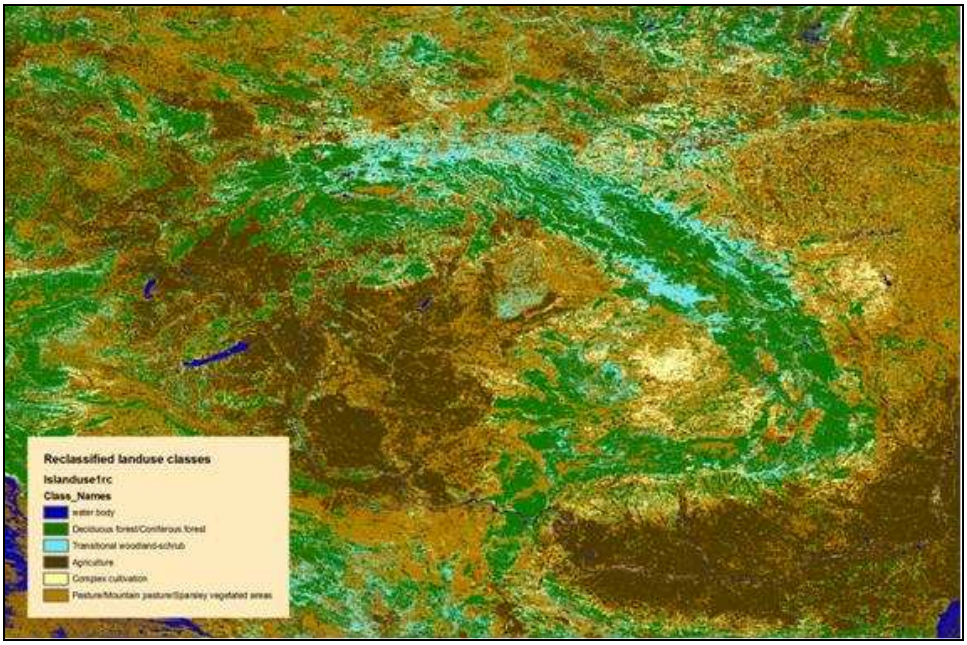

Figure 1. Land use map - derived from the MODIS data – recoded according to the LSI calculation requirement

Table 4
Land use classes and their rating

Land use description	**Rating**
Water body	0
Forests	2
Permanent crops (vineyards, fruit trees etc.)	5
Transitional woodland-shrub	6
Land principally occupied by agriculture, agro-forestry areas etc.	7
Complex cultivation patterns, arable land etc.	8
Pastures, sparsely vegetated areas etc.	9

2.1.4. Maximum precipitation within 24 hours

The precipitation dataset (maximum rainfall in 24 hours) is based on the CLAVIER precipitation database [17, 18] for the periods between 1950–2050, 1971–2000 and 2021–2050 (predicted), and represent the highest daily precipitation occurring in the selected period for a given pixel *(Figure 2).* The values were classified into four classes. Classes and their rates are shown in *Table 3.*

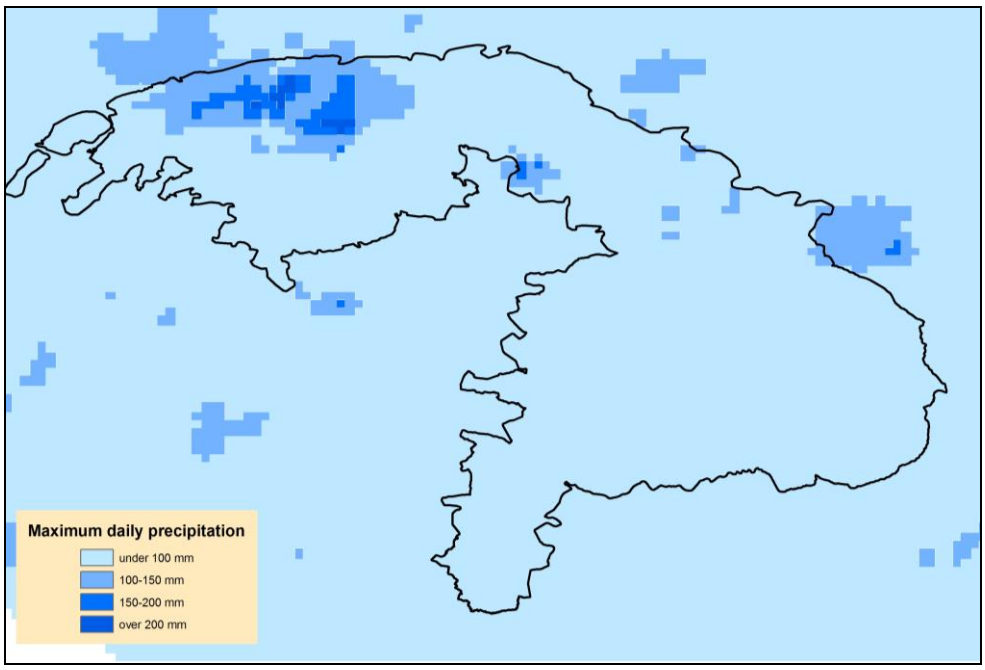

Figure 2. Maximum daily precipitation for the Carpathian region between 1950 and 2050

2.2. Methodology

The Landslide Susceptibility Index (LSI) developed by BALTEANU et al. [9] was applied here to characterize the future trends of landslide events in the Carpathian region. *Table 1* shows the factors and their original weights in the calculation process. The class ratings are listed in the corresponding *Tables 2, 3* and *4.* The equation below was used to calculate the LSI values:

$$LSI = \frac{F1*35 + F2*25 + F3*15 + F4*10 + F5*10 + F6*5}{100}$$

where F1–F6 are the rates for each factor according to *Table 1.* The Landslide Susceptibility Index may range from 0 to 10. These values have been grouped into five susceptibility classes of no (0–2), low (2–4), moderate (4–6), high (6–7) and very

high (7–10) susceptibility. This approach was slightly modified, because of the lack of harmonized seismicity information for the project. Seismicity was skipped and the remaining 5 factors were used for the LSI calculation. The 10 percent weight of seismicity was distributed equally among the remaining factors and the weights shown in *Table 5* were used.

Table 5
Factors and weights used for the LSI calculation

Causal factor	Code	Assigned weight (%)
Lithology	F1	39
Slope	F2	28
Maximum rainfall in 24 hours	F3	16.5
Land use	F4	11
Local relief	F5	5.5

The raster calculator of the Spatial Analyst module of the ArcGIS Desktop 9.3.1. software package was used for the LSI calculation.

2.2.1. Temporal trend analysis

In order to characterize the landslide susceptibility changes due to the climate change effect, two separate maximum precipitation datasets have been created, one for the period between 1971 and 2000, while the second one for the period between 2021 and 2050. Two calculations of LSI were run using these two datasets to characterize the susceptibility for the two periods. At the end the difference between the two LSI class layers was calculated to reveal the temporal changes.

3. RESULTS AND DISCUSSION

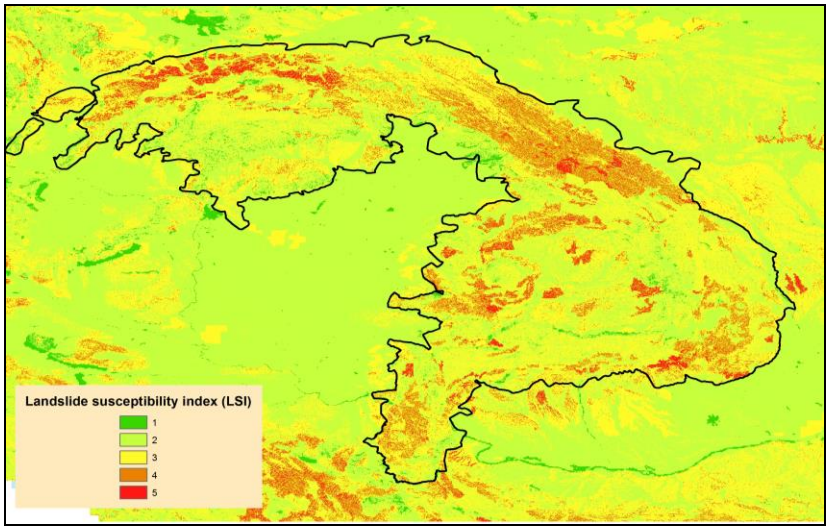

Figure 3. Landslide susceptibility map for the Carpathians

A landslide susceptibility model was performed for the Carpathian region following a modified method of BALTEANU et al. [9]. *Figures 3* and *4* show the results for the entire Carpathian region.

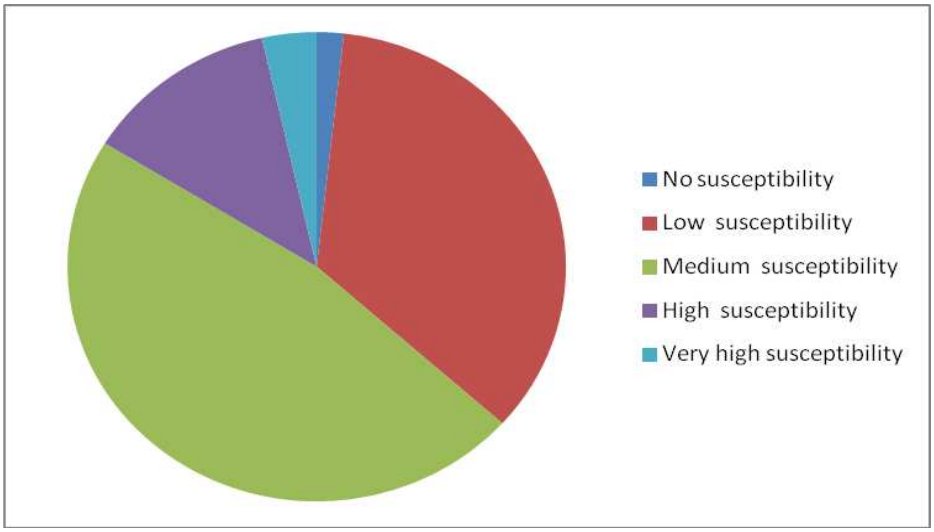

Focal area	No susceptibility	Low susceptibility	Medium susceptibility	High susceptibility	Very high susceptibility
Carpathian average	1.75	34.88	47.20	12.64	3.54

Figure 4. Landslide susceptibility class distribution for the Carpathians

Landslides are a significant natural hazard in the Carpathians. More than 65% of the entire area is classified in the medium, high or very high susceptibility classes. The high and very high susceptibility areas are located mainly in the outer bend of the Northwestern Carpathians, namely the flisch zone of the Northeastern and Eastern Carpathians, the Bend Carpathians, the Banat Mountains and in the Apuseni Mountains.

Slope and lithology have been found to be the most significant factors in the indication of the landslide probability, while the local relief factor was found to be less dominant, with only a slight impact on the final results. High or very high susceptibility areas are those where slopes exceed 12–15% and the lithology consist of sedimentary rock formations – mainly Carpathian flisch having sandstones with interlayering clay bands – and clayey Pannonian sediments in the lower lying areas, like in the Transylvanian depression.

HUBER et al. [3] summarized the major components that are responsible for landslide events. The two most important parameters, the terrain and slope material (soil and parent material) are temporarily static parameters, land use is semi-static (can be changed, but follows the traditional way defined by the environmental factors), while weather related parameters, like soil moisture, precipitation and tem-

perature changes are dynamic factors. As dynamic factors are defined by the climate, climate change may have a significant impact on landslide events. The method used here included one weather related parameter, the maximum daily precipitation. The higher the precipitation, the higher the soil moisture content and the weight of the soil matrix, contributing to the slope instability. Only the Northwestern Carpathians (the Beskids, Zapadne Tatra, High Tatra) and a small island of the Northeastern Carpathians (along the Slovakian-Ukrainian border, Szinyák, Rónahavas) have potentially higher precipitatio, than the rest of the area. Therefore, these are the only areas classified in the very high susceptibility class.

The land use layer at this scale has only a slight impact on the overall results, because the majority of the potentially damaged areas are in the mountains, where the dominant land use is forest, which does not change much. However, any clear-cut, open areas, or pastures in the mountains may increase the probability of landslide events significantly. Small spots of these land use features do not show up in the land use image derived from MODIS due to its course spatial resolution of 500 meters. Therefore this model accounts for the majority classes only.

3.1. The most susceptible areas

Areas with the highest susceptibility are those characterized by the Outer Carpathian flisch bend, where Oligocene and Eocene sandstones and clay bands dominate the lithology. The dominant slopes of these areas are between 12 and 30% and the land use is mainly forest. These areas are classified as areas with high susceptibility to landslides. The only very high susceptibility area is the outer band of the Northwestern Carpathians, where the major difference is due to the very high potential daily precipitation. This is the area where the potential climate change impact increases the susceptibility to landslide significantly.

3.2. Temporal trend analysis

The maximum daily precipitation simulation shows a significant increase over time. LSI values of the two periods, the years between 1971–2000 and 2021–2050 were compared *(Figure 5).* In the later period a significant increase was detected. The spatial distribution does not change much, but the hot spots – where higher precipitations are expected – will probably get even more precipitation. This simulation result agrees with the common scientific understandings that the intensity of rain may increase while its distribution in time becomes more uneven. The maximum daily precipitation remains unchanged for the majority of the Carpathians. A significant increase occurs only in the outer bend of the Northwestern Carpathians, namely the area NW from the High Tatra (the Zapadne Tatry area). As a consequence, this area may have an increase of more than 1 unit in the LSI index, so the susceptibility may increase by 10–15%. The Tatra National Park and the Rodna-Maramures areas may experience some slight change in the LSI values, as well.

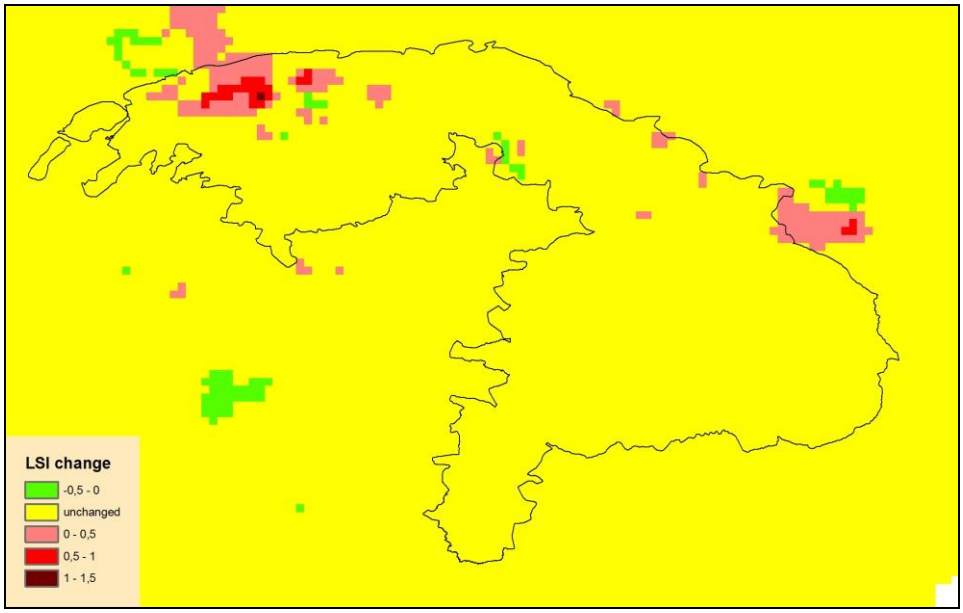

Figure 5. LSI changes between the periods 1971–2000 and 2021–2050

4. CONCLUSIONS AND RECOMMENDATIONS

Landslide mapping and inventories are not available in the same format for all European countries. Several attempts were made to collect and harmonize the available landslide data sources. However, no consistent inventory is available for the Carpathian region, meaning that modeling is the only comprehensive approach that provides harmonized information on landslide risk, hazard and susceptibility. While European studies on landslide susceptibility are available from the Joint Research Centre of the European Commission, areas outside of the EU are not covered and therefore the Northeastern Carpathians in Ukraine are missing from the database. The regional study for landslide susceptibility for Romania was performed. The study by BALTEANU et al. [9] developed a methodology fitted to the Carpathian mountains, which has been generalized and modified here to fit t the whole Carpathian region.

The results show that the Carpathian region in general is severely impacted by landslides, because the environmental conditions of the area favor the landslide development. More than 65% of the entire area is classified as medium, high and very high susceptibility classes. The high and very high susceptibility areas are located mainly in the outer bend of the Northwestern Carpathians, namely the flisch zone of the Northeastern and Eastern Carpathians, the Bend Carpathians, the Banat Mountains and in the Apuseni Mountains. These are the areas where slopes exceed 12–15%, and the lithology consists of sedimentary rock formations – mainly Carpathian flisch having sandstones with intercalated clay bands – and clayey Pannonian sediments in the lower lying areas, like in the Transylvanian depression. Slope

and lithology have been found to be the most significant factors in the indication of the landslide probability.

The maximum daily precipitation simulation shows a significant increase in time. Comparison of the periods 1971–2000 and 2021–2050 shows a significant increase in the later period. The spatial distribution does not change much, but the hot spots – where higher precipitation levels are expected – will probably get more precipitation. This simulation result agrees with the common scientific understanding that the intensity of rain may increase while its temporal distribution becomes more uneven. The maximum daily precipitation remains unchanged for the majority of the Carpathians, with significant increase occurring only in the outer bend of the Northwestern Carpathians, namely the area NW from the High Tatra (the Zapadne Tatry area). As a consequence, the susceptibility of the area may increase by 10–15 percent.

REFERENCES

[1] http://eusoils.jrc.ec.europa.eu/library/themes/Landslides/Inventories.html

[2] CRUDEN–VARNES 1996
CRUDEN, D. M.–VARNES, D. J.: Landslide Types and Processes, in Landslides – Investigation and Mitigation. *Special Report 247,* Transportation Research Board, National Research Council. National Academy Press, Washington, D. C., 1996, 36–75.

[3] HUBER et al. 2008
HUBER, S.–PROKOP, G.–ARROUAYS, D.–BANKO, G.–BISPO, A.–JONES, R. J. A.–KIBBLEWHITE, M. G.–LEXER, W.–MÖLLER, A.–RICKSON, R. J.–SHISHKOV, T.–STEPHENS, M.–TOTH, G.–VAN DEN AKKER, J. J. H.–VARALLYAY, G.–VERHEIJEN, F. G. A.–JONES, A. R. (eds.): *Environmental Assessment of Soil for Monitoring*. Volume I, Indicators & Criteria. EUR 23490 EN/1, Office for the Official Publications of the European Communities, Luxembourg, 2008.

[4] HERVÁS 2007
HERVÁS, J. (ed.): Guidelines for mapping areas at risk of landslides in Europe. *Proc. Experts Meeting, JRC,* Ispra, Italy, 23–24 October, 2007. JRC Report EUR 23093 EN, Office for Official Publications of the European Communities, Luxembourg. 2007.

[5] GALLI et al. 2008
GALLI, M.–ARDIZZONE, F.–CARDINALI, M.–GUZZETTI, F.–REICHENBACH, P.: Comparing landslide inventory maps. *Geomorphology,* 94, 2008, 268–289.

[6] HERVÁS–BOBROWSKY 2009
HERVÁS, J.–BOBROWSKY, P.: Mapping: inventories, susceptibility, hazard and risk. In: SASSA, K.–CANUTI, P. (eds.): *Landslides – Disaster Risk Reduction.* Springer, Heidelberg–Berlin, 2009, 321–349.

[7] VAN DEN EECKHAUT–HERVÁS 2012
VAN DEN EECKHAUT, M.–HERVÁS, J.: Landslide inventories in Europe and policy recommendations for their interoperability and harmonisation – A JRC contribution to the EU-FP7 SafeLand project. *JRC Report EU 25666 EN,* Publications Office of the European Union, Luxembourg, 2012.

[8] VAN DEN EECKHAUT–HERVÁS 2012
VAN DEN EECKHAUT, M.–HERVÁS, J.: State of the art of national landslide databases in Europe and their potential for assessing susceptibility, hazard and risk. *Geomorphology,* 139–140, 2012, 545–558.

[9] BALTEANU et al. 2010
BALTEANU, D.–CHENDES, V.–SIMA, M.–ENCIU, P.: A country-wide spatial assessment of landslide susceptibility in Romania. *Geomorphology,* Vol. 124, No. 3–4 (2010), 102–112.

[10] MICU 2008
MICU, M.: *Landslide hazard assessement Buzau Subcarpathians (Buzau-Telejan sector).* PhD Thesis. Romanian Academy, Institute of Geography, 2008.

[11] TODICA 2009
TODICA, T. S.: *Morfodinamica actual in zona de contact Obcinele Bucovinei-Podisul Sucevei.* PhD Thesis. Babes-Bolyai Univ. Cluj-Napoca, Faculty of Geography, 2009.

[12] GÜNTHER et al. 2012
GÜNTHER, A.–REICHENBACH, P.–MALET, J.-P.–VAN DEN EECKHAUT, M.–HERVÁS, J.–DASHWOOD, C.–GUZZETTI, F.: *Tier-based approaches for landslide susceptibility assessment in Europe. Landslides.* DOI: 10.1007/s10346-012-0349-1, 2012.

[13] HERVÁS 2013
HERVÁS, J.: Landslide Inventory. In: BOBROWSKY, P. T. (ed.): *Encyclopedia of Natural Hazards.* Springer-Verlag, Berlin–Heidelberg, ISBN 978-90-481-8699-0 (Print) 978-1-4020-4399-4 (Online), 2013, 610–611.

[14] PANAGOS et al. 2012
PANAGOS, P.–VAN LIEDEKERKE, M.–JONES, A.–MONTANARELLA, L.: European Soil Data Centre: Response to European policy support and public data requirements. *Land Use Policy,* Vol. 29, No. 2, 329–338. DOI: 10.1016/j.landusepol.2011.07.003, 2012.

[15] FARR–KOLBRICK 2000
FARR, T. G.–KOLBRICK, M.: Shuttle Radar Topography Mission produces a wealth of data. *EOS, Trans. Am. Geophys. Union,* 81, 2000, 583–585.

[16] PAUS 2012
PAUS, H.-L.: Reply of insurance industry to landslide risk. In: GLADE, T.–ANDERSON, M.–CROZIER, J. (eds.): *Landslide hazard and risk.* Wiley Online Library, 2012.

[17] KOTOVA et al. 2008
KOTOVA, Jacob D. L.–LORENZ, P.–MOSELEY, Ch.–PFEIFER, S.: Regional climate modelling activities in relation to the CLAVIER project. *Quarterly Journal of the Hungarian Meteorological Society,* 2008, 141–153.

[18] http://www.clavier-eu.org/

Geosciences and Engineering, Vol. 4, No. 7 (2015), pp. 59–74.

HOW OVERDETERMINATION AND START MODEL INFLUENCE THE ESTIMATION ACCURACY OF AN ACOUSTIC ROCK PHYSICAL MODEL

ANETT KISS

Department of Geophysics, University of Miskolc, Hungary
gfka@uni-miskolc.hu

Abstract: In geophysical exploration the knowledge of the pressure dependence of physical parameters is an important point of view. Seismic and acoustic well-logging and laboratory acoustic measurements are based on the investigation of seismic/acoustic waves in different types of rocks and under different pressures. The exponential increase in velocities due to increasing pressure is well known. Several empirical equations and qualitative models can be found in the literature, as well. The aim of the rock physical model development at the Department of Geophysics, University of Miskolc is to provide quantitative description of the phenomena with three-parameter exponential model equations, where the model parameters are determined by a quality-checked joint inversion procedure. Studies have found that the new model can be applied well in practice. In this paper, the effect of the rate of overdetermination and of the chosen start model on the inversion results is investigated. To test the effect, some data were excluded from the inversion while some were involved step-by-step, and different parameter settings were applied. Results confirmed that the model predicted accurate velocities even if data from low or high pressures had been excluded or a farther start model had been chosen.

Keywords: *acoustic velocities, rock physical model, rate of overdetermination*

1. INTRODUCTION

Geophysics has several tools to obtain information about the Earth based on physical parameters. Seismic measurements are widely used to map regional and local geological subsurface structures which are promising, for example, for hydrocarbon accumulation. Well logging provides much more local information but with a much higher resolution, for example about porosity. These methods are based on the measurement of the travel times of seismic or acoustic waves. If the velocities are also known, the length of propagation path (depth) can be calculated, or vice versa. Based on the velocities other important parameters such as the elastic moduli can be determined, which are important for example in the fracturing or production design. The longitudinal *(P)* and transverse *(S)* wave velocities can be determined on (usually cylindrical) core samples in the laboratory, as well. The advantage of the method is that the conditions are controlled and well known; on the other hand, the results obtained on core plugs provide information from a very small volume.

Like many other physical parameters, the seismic/acoustic wave velocities are also influenced by pressure. Numerous laboratory measurements [1] [2] [3] [4] [5] have focused on the investigation of the pressure dependence of the petrophysical parameters. Several studies have found an exponential relation. BIRCH [6] considers this phenomenon to be the result of changing pore volume due to varying stress. WALSH and BRACE [7] explain the increasing velocity under increasing pressure by the closure of microcracks. Empirical relations can be found in the literature, with regression parameters for the best fitting functions [8], [9]. EBERHART-PHILLIPS et al. [10] suggest the following formula

$$v = B_0 + B_1\phi + B_2\sqrt{C} + B_3(P_e - \mathrm{e}^{-16.7P_e}), \tag{1}$$

where v is the velocity, P_e is the effective pressure, B_0, B_1, B_2 and B_3 are constants, ϕ is the porosity, C is the clay content. WEPFER and CHRISTENSEN [11] proposed the empirical formula

$$v(P) = A(P/100)^a + B(1-\mathrm{e}^{-bP}), \tag{2}$$

where P is the confining pressure in MPa, v is the velocity (P or S wave), A, a, B and b are adjustable parameters. WANG et al. [12] found an alternative expression that can provide good fit with the data in the nonlinear and linear regimes

$$v = a(\ln P)^2 + b\ln P + c \quad \text{and} \quad v = v_0 + DP, \tag{3}$$

where v is the velocity, a and b are two constants describing the pressure sensitivity of velocity below the critical pressure, attributed to a combination of the gradual closure of cracks and pores and lattice compression within the sample, c is the velocity when confining pressure P is set equal to unity (1 MPa); v_0 is the extrapolated velocity of the crack-free sample at room pressure (0.1 MPa) and D is the intrinsic pressure derivative. As can be seen, these equations contain regression parameters, which should be determined empirically.

SOMOGYI MOLNÁR [13] introduced a new rock physical model describing the pressure dependence of longitudinal *(P)* wave velocity, which provides the physical connection between these quantities. Further investigations [14] [15] [16] demonstrated that the model can be extended to transverse *(S)* waves. In this paper, a complex velocity model is presented. To prove its applicability acoustic P and S wave velocity data measured on a sandstone core sample at the rock physical laboratory of the Department of Geophysics, University of Miskolc were processed using a quality-checked joint inversion procedure. The rate of overdetermination – the number of observed data compared to the number of unknown model parameters – is a key characteristic of inverse problems. Another important question is how the chosen start model influences the inversion results. To test the

reliability of the model, pressure dependent velocities were determined based on different overdetermination ratios, meaning different start models.

2. THE VELOCITY MODEL

The presented rock physical model explaining the physical relationship between the applied stress and the acoustic *P* and *S* wave velocities is based on the idea of BIRCH [6]. He assumed that the main reason for the increasing longitudinal wave velocity under loading is the closure of pores. Since the starting point of the model is the (pore) volume change, and this is an isotropic quantity, the model is applicable for both the longitudinal *(P)* and transverse *(S)* wave velocities. Increasing pressure pushes the grains closer to each other, while the pore volume decreases and the waves propagate faster through the rock. The first law of the velocity model can be formulated as

$$dV = -\lambda_V V d\sigma , \tag{4}$$

where V is the pore volume, dV is the change of unit pore volume, $d\sigma$ is the applied stress increase. The proportionality factor λ_v is a rock physical parameter. To give its meaning some more notations need to be introduced, therefore it is defined later in *Equation (13).* The negative sign represents that the increasing stress causes a decrease in the pore volume. The solution of the differential *Equation (4)* can be written as

$$V = V_0 \exp(-\lambda_V \sigma) , \tag{5}$$

where V_0 is the pore volume at a stress-free state ($\sigma = 0$).
Assuming a linear relation between the infinitesimal change of the appropriate wave velocity dv (substitutable with the longitudinal α or transverse β wave) and dV, the second model law is

$$dv = -\kappa dV , \tag{6}$$

where κ is a proportionality factor being another material characteristic. The negative sign represents the fact that decreasing pore volume results in increasing velocity. Combining *Equations (4)* and *(6)* and solving the resultant differential equation one can obtain

$$dv = \kappa\lambda_V V_0 \exp(-\lambda_V \sigma) d\sigma \quad \rightarrow \quad v = K - \kappa V_0 \exp(-\lambda_V \sigma) , \tag{7}$$

where K is an integration constant. At stress-free state ($\sigma = 0$) the propagation velocity v_0 can be measured and K can be computed from *Equation* (7) as $v_0 = K–$

κV_0. With this result and introducing the notation $\Delta v_0 = \kappa V_0$, *Equation (7)* can be rewritten in the following form

$$v = v_0 + \Delta v_0 \,(1 - \exp(-\lambda_V \sigma)) \,, \tag{8}$$

where v_0 is the propagation velocity at stress-free state. Δv_0 is called the velocity drop, which means the difference between the velocities measured at maximum and zero stresses. By substituting the appropriate velocities the model equations describing the pressure dependence of longitudinal (α) and transverse (β) waves can be obtained in the forms

$$\alpha = \alpha_0 + \Delta\alpha_0 \,(1 - \exp(-\lambda_V \sigma)) \,, \tag{9}$$

$$\beta = \beta_0 + \Delta\beta_0 \,(1 - \exp(-\lambda_V \sigma)) \,. \tag{10}$$

Note that λ_v is the same for both types of waves, thus if both *P* and *S* wave velocity data are available they can be processed in a joint inversion procedure.

The physical meaning of λ_V can be given by introducing the notations $\Delta\alpha = \alpha_{max} - \alpha$ and $\Delta\beta = \beta_{max} - \beta$ (the velocity drops caused by the presence of pores at pressure σ), and *Equations (9)–(10)* can be rewritten in the forms

$$\Delta\alpha = \Delta\alpha_0 \exp(-\lambda_V \sigma) \,, \tag{11}$$

$$\Delta\beta = \Delta\beta_0 \exp(-\lambda_V \sigma) \,. \tag{12}$$

Laboratory tests indicate that the variant types of rocks respond to pressure changes on a different scale. This feature can be described with the sensitivity function, which is widely used in the seismic [17], geoelectric [18], electromagnetic [19], well-logging [20] literature and their application in global inversion procedures [21]. Hence we introduce the (logarithmic) stress sensitivity of the velocity drops as

$$S(\sigma) = -\frac{1}{\Delta\alpha}\frac{d\Delta\alpha}{d\sigma} = -\frac{d\ln(\Delta\alpha)}{d\sigma} = -\frac{1}{\Delta\beta}\frac{d\Delta\beta}{d\sigma} = -\frac{d\ln(\Delta\beta)}{d\sigma} = \lambda_V \,. \tag{13}$$

From *Equations (11)–(12)* it can be seen that this is equal to the rock physical characteristic λ_V [22].

3. LABORATORY MEASUREMENTS

The longitudinal and transverse wave velocities are determined with the pulse transmission technique [23] in the laboratory. In this technique the sample is placed between an acoustic transmitter and receiver. A generated acoustic wave *(P* or *S)*

travels through the sample. On a screen the first arrivals are detected *(Figure 1)* and the travel times *(t_α, t_β)* are measured. Since the length of the sample *(l)* is known, the velocities *(α* and *β)* can be calculated easily

$$\alpha = l/t_\alpha \qquad \text{and} \qquad \beta = l/t_\beta \ . \tag{14}$$

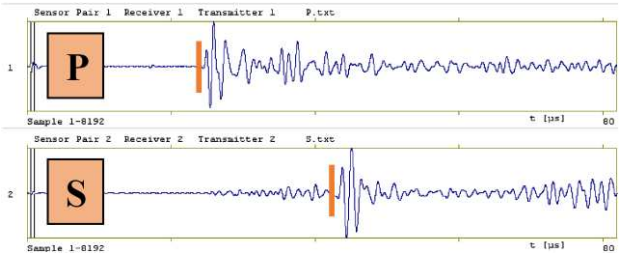

Figure 1. Detected P and S wave arrivals

Such acoustic measurements were carried out in the rock physical laboratory of the Department of Geophysics, University of Miskolc on cylindrical sandstone samples under a uniaxial load. In this paper, the investigations on sample *A* are presented. The diameter of the core plug is 3.50 cm, the length is 9.35 cm and density is 2.56 g/cm^3. The laboratory is equipped with a load frame (maximum compression force 300 kN) to apply force in axial direction onto the endcaps of the sample, a triaxial cell having special pressure stamps including piezoelectric crystals for the acoustic measurements (maximum operating pressure 80 MPa, maximum axial load 300 kN, diameter of the pressure stamp 35 mm), and an ultrasonic 2-channel device able to measure *P* and *S* wave travel times *(Figure 2).* Transducers have 1 MHz frequency of resonance. Detailed technical data can be found in [24].

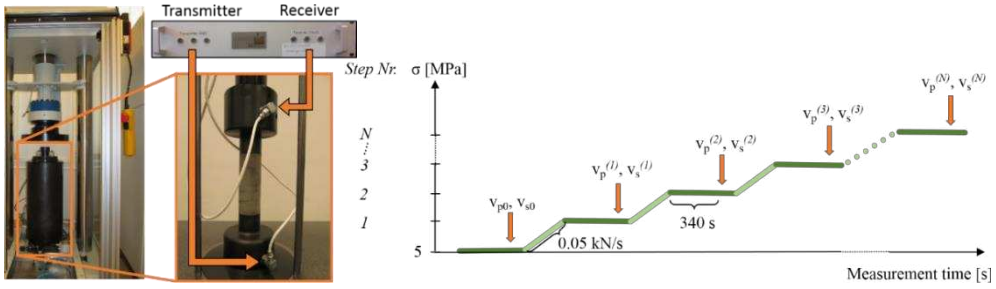

Figure 2. Left: Measuring equipment. Right: Workflow of the automatic measurement

The workflow of the measurement is shown in *Figure 2.* The axial pressure was increased stepwise from 5 MPa to 91 MPa. As can be seen, 0.05 kN/s linear loading rate was applied to produce a ramp function with the Freely Programmable Interface module of the software DION 7, which provides completely automatic

measurement. After each ramp a 340 s break was embedded for the relaxation of the sample. The *P* and *S* wave travel times were measured at each stress steps (orange arrows on the right-hand side of *Figure 2*). From the length of the sample the *P* and *S* wave velocities were calculated. We applied 256-fold stacking to increase the signal-to-noise ratio and 32 dB gain. The measured values are listed in *Table 1* and plotted with red dots in *Figure 3.*

Table 1
Measured velocities at varying uniaxial pressure

σ [MPa]	α [m/s]	β [m/s]	σ [MPa]	α [m/s]	β [m/s]
5	3691	2353	50	4248	2669
8	3729	2381	52	4269	2678
10	3763	2417	55	4291	2688
13	3803	2450	57	4308	2695
16	3846	2476	60	4324	2703
18	3889	2501	62	4340	2709
21	3930	2518	65	4357	2716
23	3967	2539	68	4371	2722
26	4003	2555	70	4383	2728
29	4035	2569	73	4398	2732
31	4065	2581	75	4410	2737
34	4095	2597	78	4421	2742
36	4126	2610	81	4433	2746
39	4151	2624	83	4444	2750
42	4178	2637	86	4454	2753
44	4203	2649	88	4463	2757
47	4225	2660	91	4473	2759

4. DATA PROCESSING

Joint inversion methods are an important research field at the Geophysical Department of the University of Miskolc [25] [26] [27]. It means that different types of data are processed together more efficiently if a connection between data sets is provided by common model parameter(s). In our case the measured longitudinal and transverse acoustic velocity data are processed by means of a quality-checked joint inversion method. The common parameter is the parameter λ_v. Since the problem is overdetermined (number of data N > number of model parameters M), the Gaussian Least Square Method is used [28].

First the model parameters of the start model are defined according to *Table 2*. With these parameters the forward problem is solved, i.e. theoretical velocities are calculated using the model *Equations (9)–(10)*. The objective function to be minimized is defined as the L_2 norm of the deviations between the measured and calculated velocities. The model parameters are modified iteratively until the stop criteria is fulfilled. The model parameters determined in the last iteration step are considered as the solution of the problem. Substituting them into the model *Equations (9)–(10)* velocities can be calculated for the stresses in the region of interest. The results are shown in *Figure 3*. As was mentioned, dots mean the measured values and the lines represent the values calculated by *Equations (9)* and *(10)* with the use of the model parameters given by the inversion procedure. It can be seen that the measured and calculated data are in good accordance.

Table 2

Parameters of the start model

Parameter	Meaning	Chosen value for the start model
α_0	*P* wave velocity at $\sigma = 0$	*P* wave velocity at $\sigma_{min,\ measured}$
$\Delta\alpha_0$	*P* wave velocity-drop $= \alpha_{max}-\alpha_0$	*P* wave velocity-drop $= \alpha_{max,\ measured}-\alpha_{min,\ measured}$
λ_v	Stress sensitivity of velocity drop	0.01
β_0	*S* wave velocity at $\sigma = 0$	*S* wave velocity at $\sigma_{min,\ measured}$
$\Delta\beta_0$	*S* wave velocity-drop $= \beta_{max}-\beta_0$	*S* wave velocity-drop $= \beta_{max,\ measured}-\beta_{min,\ measured}$

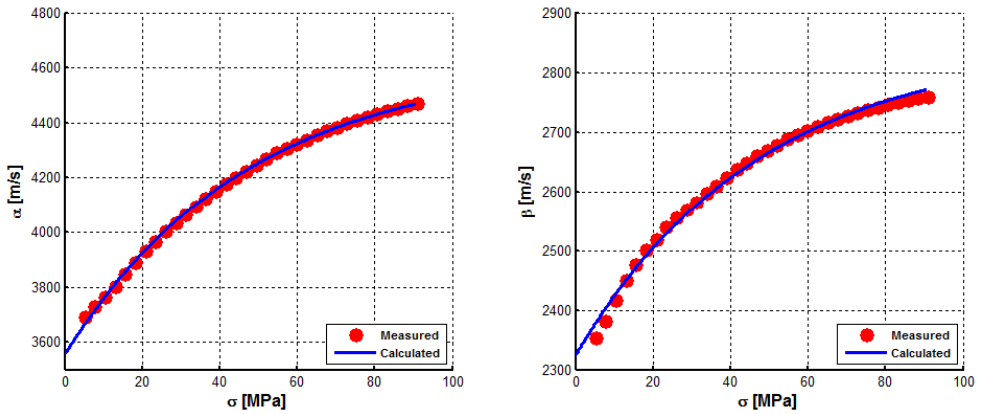

Figure 3. Measured and calculated velocity data in the range of 5–91 MPa

The estimation errors of the model parameters *(std_i)* are in the main diagonal of the covariance matrix in parameter space (number of parameters is *M*, which $i = 1,2,\ldots,5$ in the given problem)

$$std_i = \sqrt{cov(\boldsymbol{m})_{ii}}\ . \tag{15}$$

To characterize the accuracy of data fit of the inversion estimates the *RMS* value is calculated with the following formula [28]

$$RMS = \sqrt{\frac{1}{N}\sum_{k=1}^{N}\left(\frac{d_k^{(m)} - d_k^{(c)}}{d_k^{(c)}}\right)^2} \cdot 100\,[\%]\,, \tag{16}$$

where $d_k^{(m)}$ is the measured data at the *k*-th pressure and $d_k^{(c)}$ is the *k*-th calculated data computed with the *model Equations (9)–(10), N* is the number of measured data. The mean spread showing the reliability of the suggested rock physical model is also determined with the formula below, where δ is a Kronecker-delta symbol and *corr(***m***)* is the correlation matrix in parameter space, which provides the strength of linear relationships between each pair of model parameters

$$S = \sqrt{\frac{1}{M(M\text{-}1)}\sum_{i=1}^{M}\sum_{j=1}^{M}\left(corr(\boldsymbol{m})_{ij} - \delta_{ij}\right)^2}\,. \tag{17}$$

5. EFFECT OF OVERDETERMINATION RATIO

During laboratory measurements some limiting factors must be considered. At small pressures the first arrivals can often be hardly detected, especially in case of transverse waves. The signal-to-noise ratio can be increased by a higher stacking number (sum of more measurements), but it has limitations. Only random noise can be reduced with this signal sum up, and the higher the stacking number the longer the measurement. Another aspect is to avoid making new microcracks or total failure of the sample due to overloading. In other words samples have to be handled with care and a reliable model which is able to predict the velocities for wider pressure intervals can be a good solution.

The aim of this study was to examine the effect of rate of overdetermination *(N/M)* on inversion results. Therefore, data from different pressure ranges were used as input data vector for the inversion. Based on the "actual" measured data the model parameters were estimated by joint inversion and the velocities were calculated for the pressure range 0–150 MPa in each case. Results are shown in *Figures 4–5.* For better visibility graphs do not contain the measured data, only the velocities calculated by inversion. The estimated model parameters with the estimation errors in the parenthesis, as well as the *RMS* and mean spread are summarized in *Table 3.*

In *Case 1, P* and *S* wave velocities belonging to the pressure ranges 5–31 MPa, 5–50 MPa, 5–70 MPa and 5–91 MPa were processed, accordingly the *N/M* rate was increased from 2.2 to 6.8 by involving measured data from higher pressures. It can be seen in *Figure 4* and in *Table 3* that the model parameters determined from a lower number of measured data slightly overestimate the velocities. Their

estimation errors – especially that of the velocity drops – decrease with increasing *N/M* ratio. Of course, it is expected that higher overdetermination of the problem will reduce the error of the determined parameters. Comparing the results obtained for the pressure interval 5–31 MPa and 5–91 MPa, it can be seen that the estimation error of $\Delta\alpha_0$ reduces from 17% to 0.7%, and $\Delta\beta_0$ reduces from 17% to 1.3%. Since the picking of first arrivals in the low pressure intervals is uncertain because of the higher noise and considering that the 11 measured data are mostly on the linear interval of the velocity change, the applied velocity model can be considered reliable even for the case when fewer data in the lower pressure interval are available. This is important if the strength of the sample is unknown and one would like to avoid the overloading and failure of the sample, and thus the measurement is planned to stay in the "safe" interval.

In *Case 2,* the measured points at the beginning phase of loading (5–23 MPa) were excluded, because in this region the picking of first arrivals is not always easy and this interval can contain more uncertainty. Velocity data for pressure intervals 23–50 MPa, 23–68 MPa and 23–91 MPa were inverted (*N* varies from 11 to 27). With an increasing number of data the velocities determined by the velocity model slightly decrease, as can be seen in *Figure 5* and *Table 3.* Comparing the results for *N/M* ratios 2.2 and 3.6 from *Case 1* and *2,* it can be seen that the estimation errors are lower if data from the non-linear phase are inverted. From the results plotted with blue and green lines in *Figure 5* it can be concluded that the intermediate number of data had already provided acceptable results, especially for *P* wave.

If *Cases 1* and *2* are compared in total, it can be seen that the relative distances in data space *(RMS)* are lower if data do not contain the velocities measured at low pressures, i.e. in *Case 2.* Looking at the mean spread *(S)* one can conclude that it can be reduced effectively by involving more data.

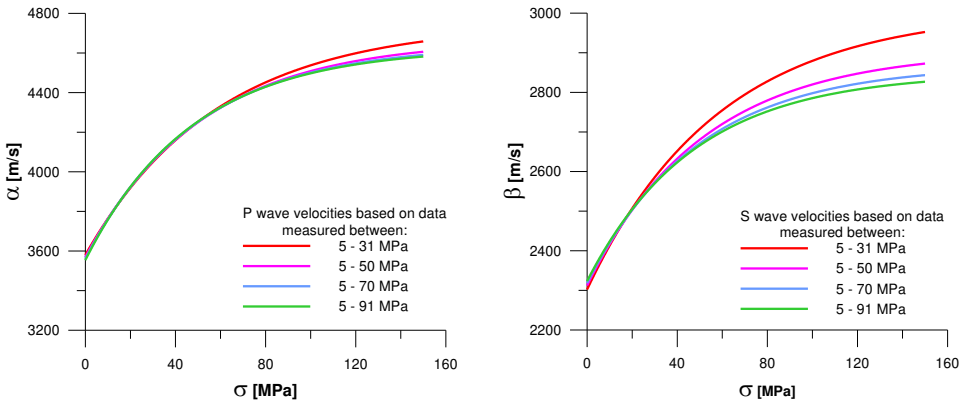

Figure 4. Velocities estimated by inversion based on data measured in different intervals

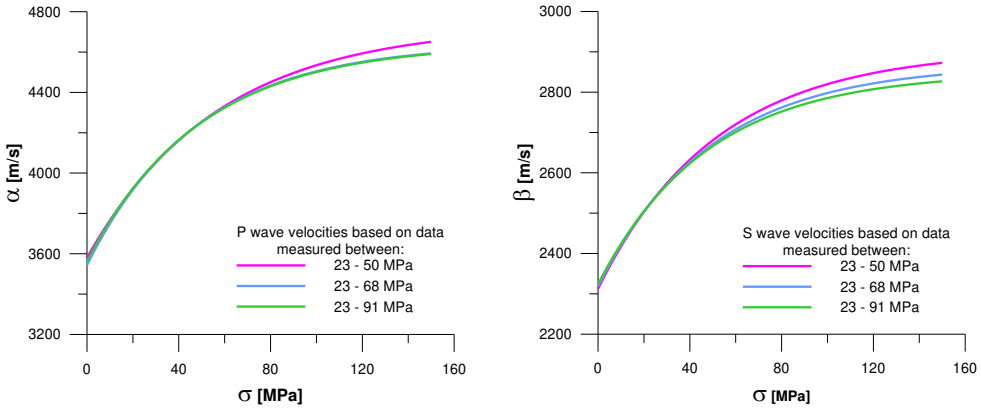

Figure 5. Velocities estimated by inversion based on data measured in different intervals

Table 3
Estimated model parameters and their estimation errors, RMS and mean spread

#	N	N/M	Pressure [MPa]	α_0 [m/s]	$\Delta\alpha_0$ [m/s]	λ_V [1/MPa]	β_0 [m/s]	$\Delta\beta_0$ [m/s]	RMS [%]	S [–]
CASE 1	11	2.2	5–31	3579 (±10)	1168 (±203)	0.0172 (±0.0042)	2302 (±9)	704 (±123)	0.25	0.80
	18	3.6	5–50	3568 (±7)	1097 (±43)	0.0194 (±0.0014)	2312 (±6)	593 (±26)	0.26	0.70
	26	5.2	5–70	3560 (±6)	1080 (±15)	0.0204 (±0.0007)	2318 (±5)	551 (±11)	0.26	0.58
	34	6.8	5–91	3553 (±5)	1074 (±7)	0.0211 (±0.0004)	2323 (±5)	526 (±7)	0.27	0.47
CASE 2	11	2.2	23–50	3579 (±9)	1154 (±24)	0.0176 (±0.0009)	2355 (±5)	543 (±12)	0.04	0.88
	18	3.6	23–68	3543 (±6)	1099 (±4)	0.0208 (±0.0004)	2344 (±4)	505 (±4)	0.05	0.60
	27	5.4	23–91	3523 (±5)	1097 (±3)	0.0220 (±0.0003)	2345 (±4)	485 (±4)	0.08	0.56

6. CHOOSING THE START MODEL

In linearized inverse problems the choice of start model is always a key issue. In *Section 4* it was already mentioned how the model parameters were chosen in the given problem *(Table 2)*. The investigations on the effect of overdetermination ratio provided a set of different start models: *Cases 1* and *2* are different regarding the parameters α_0 and β_0 because these velocities belonged to the minimal pressures 5 and 23 MPa, respectively. The single subcases of different overdetermination ratios provided different $\Delta\alpha_0$ and $\Delta\beta_0$ parameters, since the

maximal values of velocities varied and so the velocity drops, meaning that the difference of velocities at maximal and minimal pressures also changed. The initial value of parameter λ_v was always 0.01; this seemed experimentally reliable for all cases. The applied start model parameters are listed in the grey columns of *Table 4.* If *Tables 3* and *4* are examined together, it can be seen that despite the different start values of model parameters the inversion found almost the same final results for the parameters.

To show that the model and the inversion work also if the start model parameters are farther from the solution we investigated *Case 3,* where the parameters of the start model were chosen independently from the measured data sets. We varied not only the starting values of α_0, β_0, $\Delta\alpha_0$ and $\Delta\beta_0$, but λ_v as well. The number of iterations remained 10 and the results were the same as in *Case 1,* where all of the 34 velocity data were inverted (fourth row in *Table 3* and *4*). The chosen start parameters and the RMS values calculated in the first and last iteration steps are listed in *Table 4.* It can be seen that the inversion found the optimal solution, even when they are far from the starting values. The process can be considered fast as well, because only 10 iteration steps were used and no significant changes occurred in model parameters.

Table 4

Start model parameters in grey columns, RMS for the first and last iteration steps

#	N	N/M	σ [MPa]	α_0 [m/s]	α_{max} [m/s]	$\Delta\alpha_0$ [m/s]	λ_V [1/MPa]	β_0 [m/s]	β_{max} [m/s]	$\Delta\beta_0$ [m/s]	"starting" RMS [%]	RMS [%]
CASE 1	11	2.2	5–31	3691	4065	374	0.1	2353	2581	228	2.82	0.25
	18	3.6	5–50	3691	4248	557	0.1	2353	2669	316	4.54	0.26
	26	5.2	5–70	3691	4383	692	0.1	2353	2728	375	5.44	0.26
	34	6.8	5–91	3691	4473	782	0.1	2353	2759	406	5.33	0.27
CASE 2	11	2.2	23–50	3967	4248	281	0.1	2539	2669	130	1.46	0.04
	18	3.6	23–68	3967	4371	404	0.1	2539	2722	183	1.69	0.05
	27	5.4	23–91	3967	4473	506	0.1	2539	2759	220	1.76	0.08
CASE 3	34	6.8	5–91	1000	–	100	0.2	1000	–	100	68.14	0.27
	34	6.8	5–91	6000	–	600	0.2	8000	–	800	162.45	0.27
	34	6.8	5–91	12000	–	1000	0.2	9500	–	1000	242.79	0.27
	34	6.8	5–91	12000	–	1000	0.02	9500	–	1000	233.11	0.27

7. CONCLUSIONS

Longitudinal and transverse acoustic wave velocities were determined under varying uniaxial pressure in the laboratory. Data were inverted according to the suggested rock physical model describing the pressure dependence of parameters in a quality-checked joint inversion procedure. The advantage of the model is that after determining the model parameters, *P* and *S* wave velocities can be calculated for any pressure using the model equations. Since the velocity measurements have limitations, i.e. the determination of first arrivals can be uncertain at low pressures, and we have to avoid the failure of the sample at high pressures, the effects of rate of overdetermination on inversion results were investigated. In *Case 1* measured data from higher pressures were involved stepwise, in *Case 2* the beginning phase of loading was excluded. Based on the investigations it can be concluded that the presented velocity model predicts reliable velocities even if data up to ($\sigma < 50$ MPa) or only at a (23 MPa $< \sigma <$ 68 MPa) intermediate pressure level are measured. These investigations included the testing of different start models as well. From the results it can be seen that the chosen start model did not essentially influence the estimated model parameters; the inversion found the optimal model parameters in a few iteration steps.

ACKNOWLEDGEMENT

This study was supported by the Hungarian Research Fund OTKA, project No.: K 109441.

LIST OF SYMBOLS

Symbol	Description	Unit
a	constant	–
A	constant	–
b	constant	–
B	constant	–
c	velocity when confining pressure *P* equals unity	m/s
C	clay content (varies from 0.0 to 0.5)	–
corr(m)	correlation matrix	–
cov(m)	covariance matrix in parameter space	–
D	intrinsic pressure derivative	1/MPa
$d_k^{(c)}$	calculated velocity at the k-th pressure value	m/s
$d_k^{(m)}$	measured velocity at the k-th pressure value	m/s
dv	change of propagation wave velocity	m/s
dV	change in the unit pore volume	m^3
dσ	stress increase	MPa
K	integration constant	–
l	length	m
M	number of model parameters	–

N	number of measured points	–
P	pressure	MPa
P_e	effective pressure	MPa
RMS	Root Mean Square	%
S	mean spread	–
$S(\sigma)$	stress sensitivity of velocity drop	1/MPa
std_i	estimated error of the i-th model parameter	–
t_α	travel time of P wave	s
t_β	travel time of S wave	s
V	pore volume	m^3
v	acoustic wave velocity	m/s
V_0	pore volume at $\sigma = 0$	m^3
v_0	wave velocity at stress-free state	m/s
α	longitudinal *(P)* wave velocity	m/s
α_0	longitudinal *(P)* wave velocity at stress-free state	m/s
α_{max}	P wave velocity at maximum pressure	m/s
β	transverse *(S)* wave velocity	m/s
β_0	transverse *(S)* wave velocity at stress-free state	m/s
β_{max}	S wave velocity at maximum pressure	m/s
δ	Kronecker-delta symbol	–
Δv_0	velocity drop at zero pressure	m/s
$\Delta\alpha$	P wave velocity drop at pressure σ	m/s
$\Delta\alpha_0$	P wave velocity drop at pressure $\sigma = 0$	m/s
$\Delta\beta$	S wave velocity drop at pressure σ	m/s
$\Delta\beta_0$	S wave velocity drop at pressure $\sigma = 0$	m/s
κ	proportionality factor	$1/m^2s$
λ_V	new material quality dependent petrophysical parameter	1/MPa
σ	stress	MPa
ϕ	porosity	–

REFERENCES

[1] WYLLIE–GREGORY–GARDNER 1958
WYLLIE, M. R. J.–GREGORY, A. R.–GARDNER, G. H. F.: An experimental investigation of factors affecting elastic wave velocities in porous media. *Geophysics,* 23, 1958, 459–493.

[2] NUR–SIMMONS 1969
NUR, A.–SIMMONS, G.: The effect of saturation on velocity in low porosity rocks. *Earth and Planetary Science Letters,* 7, 1969, 183–193.

[3] STACEY 1976
STACEY, T. R.: Seismic assessment of rock masses. *Proceedings of Symposium on Exploration for Rock Engineering,* Johannesburg, 1976.

[4] SENGUN et al. 2011
SENGUN, N.–ALTINDAG, R.–DEMIRDAG, S.–YAVUZ, H.: P-wave velocity and Schmidt rebound hardness value of rocks under uniaxial compressional loading. *International Journal of Rock Mechanics and Mining Sciences,* 48, 2011, 693–696.

[5] HE–SCHMITT 2006
HE, T.–SCHMITT, D. R.: Velocity measurements of conglomerates and pressure sensitivity analysis of AVA response. *Proceedings of 76th SEG International Exposition and Annual Meeting,* New Orleans, USA, 2006.

[6] BIRCH 1960
BIRCH, F.: The velocity of compression waves in rocks to 10 kbars. *Journal of Geophysical Research,* 65, 1960, 1083–1102.

[7] WALSH–BRACE 1964
WALSH, J. B.–BRACE, W. F.: A fracture criterion for brittle anisotropic rock. *Journal of Geophysical Research,* 69, 1964, 3449–3456.

[8] FREUND 1992
FREUND, D.: Ultrasonic compressional and shear velocities in dry clastic rocks as a function of porosity, clay content, and confining pressure. *Geophysical Journal International,* 108, 1992, 125–135.

[9] KHAKSAR–GRIFFITHS–MCCANN 1999
KHAKSAR, A.–GRIFFITHS, C.–MCCANN, C.: Effective stress coefficient for P- and S-wave velocity and quality factor in sandstone. Example from Cooper Basin, Australia. *Proceedings of 69th SEG Annual Meeting,* Houston, USA, 1999.

[10] EBERHART-PHILLIPS–HAN–ZOBACK 1989
EBERHART-PHILLIPS, D.–HAN, D. H.–ZOBACK, M. D.: Empirical relationships among seismic velocity, effective pressure, porosity, and clay content in sandstone. *Geophysics,* 54, 1989, 82–89.

[11] WEPFER–CHRISTENSEN 1991
WEPFER, W. W.–CHRISTENSEN, N. I.: A seismic velocity-confining pressure relation, with applications. *International Journal of Rock Mechanics and Mining Sciences,* 28, 1991, 451–456.

[12] WANG et al. 2005
WANG, Q.–JI, S. C.–SALISBURY, M. H.–PAN, M. B.–XIA, B.–XU, Z. Q.: Pressure dependence and anisotropy of P-wave velocities in ultrahigh-pressure metamorphic rocks from the Dabie-Sulu orogenic belt (China): Implications for seismic properties of subducted slabs and origin of mantle reflections. *Tectonophysics,* 398, 2005, 67–99.

[13] SOMOGYI MOLNÁR 2013
SOMOGYI MOLNÁR, J.: *Rugalmas hullámok terjedési jellemzőinek nyomásfüggése – új kőzetfizikai modellek.* PhD dissertation. University of Miskolc, 2013.

[14] SOMOGYI MOLNÁR–KISS–DOBRÓKA 2015
SOMOGYI MOLNÁR, J.–KISS, A.–DOBRÓKA, M.: Petrophysical models to describe the pressure dependence of acoustic wave propagation characteristics. *Acta Geodaetica et Geophysica,* 3, 2015, 339–352.

[15] SOMOGYI MOLNÁR–KISS–DOBRÓKA 2014
SOMOGYI MOLNÁR, J.–KISS, A.–DOBRÓKA, M.: Rock Physical Model of the Pressure Dependence of Elastic Moduli. *76th EAGE Conference and Exhibition,* Amsterdam, The Netherlands, 2014.

[16] SOMOGYI MOLNÁR–KISS–DOBRÓKA 2014
SOMOGYI MOLNÁR, J.–KISS, A.–DOBRÓKA, M.: Describing the pressure dependence of Lamé coefficients on coal samples. *Near Surface Geoscience 2014 Conference,* Athen, Greece, 2014.

[17] DOBRÓKA 1987
DOBRÓKA, M.: Love seam-waves in a horizontally inhomogeneous three-layered medium. *Geophysical Prospecting,* Vol. 35, No. 5 (1987), 502–516.

[18] GYULAI 1989
GYULAI, Á.: Parameters sensitivity of underground DC measurements. *Geophysical Transactions,* Vol. 35, No. 3 (1989), 209–225.

[19] SZALAI–SZARKA 2008
SZALAI, S.–SZARKA, L.: Parameter sensitivity maps of surface geoelectric arrays, I. Linear arrays. *Acta Geodaetica et Geophysica Hungarica,* 43, 2008, 419–437.

[20] DOBRÓKA–SZABÓ 2011
DOBRÓKA, M.–SZABÓ, N.: Interval inversion of well-logging data for objective determination of textural parameters. *Acta Geophysica,* Vol. 59, No. 5 (2011), 907–934.

[21] SZABÓ 2004
SZABÓ, N. P.: Global inversion of well log data. *Geofizikai Közlemények – Geophysical Transactions,* Vol 44, No. 3–4 (2004), 313–329.

[22] DOBRÓKA–SOMOGYI MOLNÁR 2012
DOBRÓKA, M.–SOMOGYI MOLNÁR, J.: The pressure dependence of acoustic velocity and quality factor: new petrophysical models. *Acta Geodaetica et Geophysica Hungarica,* 47, 2012, 149–160.

[23] TOKSÖZ–JOHNSTON–TIMUR 1979
TOKSÖZ, M. N.–JOHNSTON, D. H.–TIMUR, A.: Attenuation of seismic waves in dry and saturated rocks: I. Laboratory measurements. *Geophysics,* 44, 1979, 681–690.

[24] SOMOGYI MOLNÁR–KISS–DOBRÓKA 2015
SOMOGYI MOLNÁR, J.–KISS, A.–DOBRÓKA, M.: An automatic test system to measure acoustic velocity data to prove the applicability of the new rock physical model. *Geosciences and Engineering: A Publication of The University of Miskolc,* Vol. 4, No. 6 (2015), 22–35.

[25] DOBRÓKA–SZABÓ–TURAI 2012
DOBRÓKA, M.–SZABÓ, N. P.–TURAI, E.: Interval inversion of borehole data for petrophysical characterization of complex reservoirs. *Acta Geodaetica et Geophysica Hungarica,* Vol. 47, No. 2 (2012), 172–184.

[26] DOBRÓKA–SZABÓ 2012
DOBRÓKA, M.–SZABÓ, N. P.: Interval inversion of well-logging data for automatic determination of formation boundaries by using a float-encoded genetic algorithm. *Journal of Petroleum Science and Engineering,* 86–87, 2012, 144–152.

[27] DOBRÓKA et al. 2016
DOBRÓKA, M.–SZABÓ, N. P.–TÓTH, J.–VASS, P.: Interval inversion approach for an improved interpretation of well logs. *Geophysics,* Vol. 81, No. 2 (2016), 163–175.

[28] MENKE 1984
MENKE, W.: *Geophysical data analysis – Discrete inverse theory.* Academic Press, London, 1984.

Geosciences and Engineering, Vol. 4, No. 7 (2015), pp. 75–85.

EVALUATION OF THE BIOSORPTION POTENTIAL OF *UNDARIA PINNATIFIDA* MACRO ALGAE IN A COLUMN SYSTEM WITH REAL EFFLUENTS

JÓZSEF PAULOVICS[1]–LJUDMILLA BOKÁNYI[2]

[1]*EMK North Hungarian Environmental Protection Ltd., Gyártelep, Sajóbábony HU-3792, Hungary (paulovics.jozsef@gmail.com)*
[2]*Institute of Raw Material Preparation and Environmental Processing University of Miskolc, Egyetemváros, Miskolc, HU-3515, Hungary (ejtblj@uni-miskolc.hu)*

Abstract: Different research groups have accomplished a large number of laboratory investigations and experiments on biosorption aimed at the pollution removal from aqueous solutions with different kinds of biomass. The most investigated materials in the development of biosorbents are micro- and macro algae. A representative of the latter group, *Undaria pinnatifida* macro algae, have outstanding transient metal sorption ability. The *U. pinnatifida* biosorption research presented in this paper was carried out applying a custom-built biosorption column system. Two real effluent samples were examined: a groundwater sample from a site contaminated with heavy metal and a scrubber water sample from the wet flue-gas cleaning process of a hazardous waste incineration plant. The aim of the research was to compare the biosorption results obtained for the polycationic model solutions with those of the real systems. It was established that *U. pinnatifida* biosorption is a promising technique for the removal of the polluting metals from effluent. It has selectivity towards lead. The results obtained for the real systems are somewhat poorer than those for polycationic model solutions. The main reason is the complexity of the real solutions, as well as some processing difficulties using columns in series. For selecting the raw material of the biosorbent, it can be stated that it is important to know the place of origin and any previous treatment of the biomass – especially by macro algae – because it can be contaminated with pollutants (e.g. heavy metals) from the environment during its growth and from pretreatment processes after harvesting, as well.

Keywords: *biosorption, heavy metals, algae, Undaria pinnatifida*

1. INTRODUCTION

Conventional methods (e.g. chemical precipitation, oxidation/reduction, ion-exchange, electrolysis and membrane filtration) have been widely used to remove toxic metals from different kinds of industrial wastewaters and contaminated groundwater. Nevertheless, the phenomenon of biosorption could be a promising alternative to these conventional methods in the near future. Unlike the conventional techniques, biosorption is environmentally friendly, as the biosorbents are renewable.

Many kinds of biological material have an affinity for binding inorganic and organic pollutants, so there is an enormous biosorption potential within the countless types of biomaterials (GADD, 2009; DHANKHAR and HOODA, 2011).

Numerous research attempts on biosorption has been made by different universities and research groups around the world for the last three decades. One of the most important research teams in this field is the Technische Universität Berlin, where research on bioprocessing, including research on biosorption, has been taking place. The Institute of Raw Material Preparation and Environmental Processing at the University of Miskolc, has been cooperating with this research group in Berlin in the framework of a DAAD program on investigation of the biosorption process (BOKÁNYI et al., 2011).

Different research groups have accomplished a large number of laboratory investigations and experiments with different kinds of biomass. The most investigated materials in the development of biosorbents are the micro- and macro algae. Within the latter group, *Undaria pinnatifida* macro algae have outstanding transition metal sorption ability (KLIMMEK et al., 2001; BUNKE et al., 2003; PLAZA CAZÓN et al., 2013). Macro algae, especially brown algae, have been found to be very effective biosorbents in removing transition metals from wastewater because of their high uptake capacities, adequate to commercial ion-exchange resins, and their availability in nearly unlimited amounts from the oceans (LEUSCH et al., 1995; KIM et al., 1999; LIU et al., 2009).

Lead, cadmium, copper, nickel and zinc are important metals regarding their environmental impact and industrial usage as well. Our research has proved earlier that if several metal ions occur in a solution in equimolar concentration – lead (Pb^{2+}), cadmium (Cd^{2+}), copper (Cu^{2+}), nickel (Ni^{2+}) and zinc (Zn^{2+}) – then *U. pinnatifida* macro algae adsorbs the lead in the highest amount *(Figure 1).* The adsorption of lead seems not to be affected by the presence of other cations, and it is similar to the adsorption process in a mono-cationic system. It can be therefore stated that *U. pinnatifida* has a selective adsorption ability towards the lead. The adsorption of other cations is a competitive one (BOKÁNYI et al., 2009).

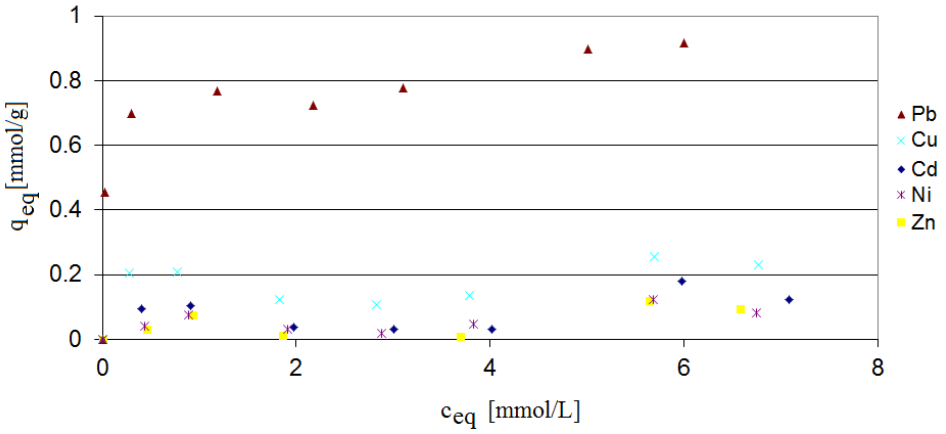

Figure 1. Adsorption ability of U. pinnatifida in polycationic system
(BOKÁNYI et al., 2009)

The present study reports experimental results obtained for real contaminated effluents from different sources: the groundwater from a heavy-metal contaminated site in Northern Hungary and the scrubber effluent from the wet flue-gas cleaning process of a Hungarian hazardous waste incineration plant. Biosorption experiments using *U. pinnatifida* macro algae were carried out in a column system. The main aim of the experiments was to compare the polluting metals uptake by biosorption in real systems with the experimental results obtained for the model solutions.

2. MATERIALS AND METHODS

2.1. The investigated effluents and their pretreatment

This paper reports the description and results of biosorption experiments with two different effluents, a groundwater sample originated from a site contaminated with heavy metal and a scrubber effluent sample from the wet flue-gas cleaning process of a hazardous waste incineration plant.

The effect of pH on metal biosorption has been studied by many researchers, and the results indicate that the pH value of a solution can significantly influence the biosorption (LIU et al., 2009; MONTAZER-RAHMATIA et al., 2011), thus the pH value of the effluents needs to be adjusted prior to the biosorption with *U. pinnatifida* macro algae up to pH = 4...6.

Sample 1: Groundwater

The first sample used in our investigation originated from a heavy-metal contaminated site in the area of Gyöngyösoroszi, Northern Hungary (FT-1 monitoring well, EOV 712 099; 278 372).

The sample of this effluent had pH = 4.9 before the biosorption, thus we did not use pH adjustment, while the suspended solid particles were removed using filter paper (grade: 1,290; diameter: 150 mm; 84 g/m^2).

The biosorption experiment was carried out with 3 L of this sample. *Table 1* contains the initial concentrations of different metals before the biosorption.

Table 1
Initial metal concentrations in the groundwater sample

Unit	Chemical elements						
	Al	**Cd**	**Cu**	**Mn**	**Ni**	**Pb**	**Zn**
mg/L	2.13	0.133	0.48	3.47	0.077	0.037	25.01

Sample 2: Scrubber effluent

The second sample used in our investigation originates from the hazardous waste incineration plant in Sajóbábony, Hungary. The samples were collected after the

wet flue-gas cleaning process (two acid- and one alkaline scrubbers) and before the precipitation and settling treatment process of scrubber water in the plant.

The sample from the incineration plant had an acidic pH value of 1.4, thus it was adjusted using 1 M NaOH to 5.6, then the solid particles were removed using filter paper (grade: 1,290; diameter: 150 mm; 84 g/m^2).

The biosorption experiment was carried out with 3 L of this sample. *Table 2* contains the initial concentrations of different metals before the biosorption.

Table 2
Initial metal concentrations in the scrubber effluent sample

Unit	Chemical elements							
	As	**Cd**	**Cr**	**Cu**	**Hg**	**Ni**	**Pb**	**Zn**
mg/L	<0.002	0.012	0.005	2.629	0.345	0.010	0.513	0.881

2.2. Biological material and its pretreatment

The brown algae *U. pinnatifida* is an invasive species belonging to the *Phaeophyta* class and the *Laminariales* order. The dried algae biomass used in this work was purchased as foodstuff from a grocery store in Hungary. It was imported by Pan Asia Handels Ges.m.b.H under the product name *Wakame*.

The dried macro algae can swell significantly while contacting with water, thus it was applied after grinding, because our previous experiments showed that the < 1 cm particle size fraction of this algae can easily cause clog in our columns, which have a diameter of 3 cm. Before the biosorption the dried biomass was ground using a mortar.

Sample 1: Groundwater
The applied biosorbent was sieved and the fraction between 1 and 2 cm particle size was packed into columns, then it was washed once using distilled water (500 mL per column).

Sample 2: Scrubber effluent
To avoid the effect of salts, 3 g of dried alga was suspended in 100 mL of acidic distilled water (pH was adjusted down to 2 using 8 M HCl), then flushed with another 100 mL acidic distilled water. After this pretreatment it was packed in the columns.

2.3. Biosorption in fixed bed columns

Our biosorption research with the *U. pinnatifida* was carried out at the University of Miskolc, Institute of Raw Materials Preparation and Environmental Processing, Department of Bioprocessing and Reaction Techniques using custom-built biosorption column system.

2.3.1. Experiments with groundwater

A biosorption column system with 4 open-top columns was built in the laboratory to test the groundwater sample (see *Figure 2*). Each of the four plastic columns had an inner diameter of 3 cm and height of 20 cm. These columns were coupled in series, and 3 grams of biomass (the fraction between 1 and 2 cm particle size) were packed in each column. Bed height of the dry biomass was 2 cm in the columns, but during the experiments it increased up to 10 cm when the dried macro algae became wet. Before the biosorption experiments the biosorbent was washed with 500 mL of distilled water.

Three liters of the effluent were fed downward through the four columns, after the fourth column the effluent was fed again into the first and then the second columns at ~1.6 $mL*s^{-1}$ using a peristaltic pump.

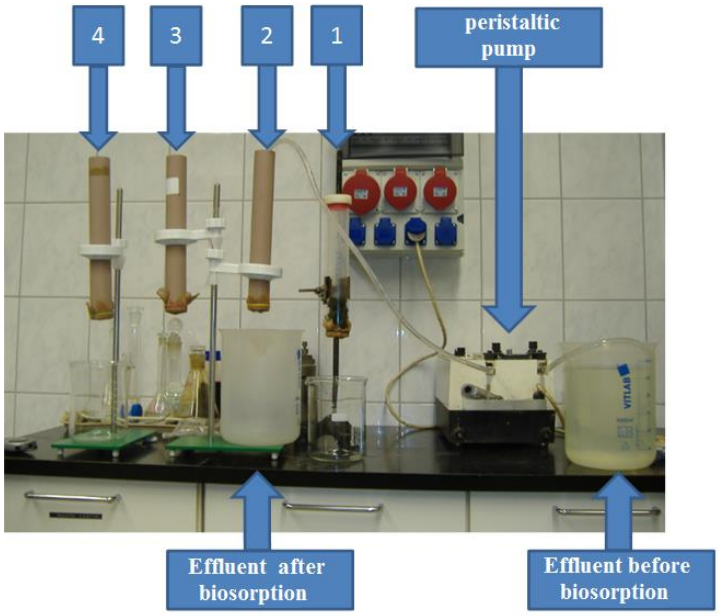

Figure 2. The biosorption column system installation applied in the experiments with groundwater

Effluent was collected from the bottom of the column to analyze metal concentrations in the liquid phase using ICP OES (Varian 720-ES). The concentration measurements were carried out at the Institute of Chemistry, Faculty of Materials Science and Engineering, University of Miskolc.

2.3.2. Experiments with scrubber effluent

In case of the scrubber effluent sample we installed a similar biosorption column system as shown in *Figure 2,* but only two columns were applied (3 cm inner diameter and 20 cm height). These columns were coupled in series, and 3 grams of

biomass (fraction between 1 and 2 cm particle size) were packed in every column. Bed height of the dry biomass was 2 cm in the columns, but during the experiments the bed height increased to 10 cm while the dried macro algae became wet. Before the biosorption experiments the biosorbent was suspended in 100 mL of acidic distilled water (pH was adjusted down to 2 using 8 M HCl), then flushed with another 100 mL acidic distilled water.

Three liters of the metal solution was fed downward through the columns at ~1.6 $mL*s^{-1}$ flow rate using a peristaltic pump. Effluents were sampled after every column to analyze metal concentrations in the liquid phase using ICP OES.

After the biosorption experiments, the scrubber water samples were examined using ICP-OES (SPECTRO CIROS VISION). These chemical analytical measurements were carried out at the KISANALITIKA Laboratory Services Ltd., Sajóbábony.

3. RESULTS AND DISCUSSION

3.1. Pollution limit values and technological emission limits

Regarding the pollution limit values for our examined groundwater, the relevant authority regulation in Hungary is the joint decree of the Ministry of Environment, the Ministry of Health, and the Ministry of Agriculture and Rural Development No. 6/2009 (IV. 14.) on the protection against the contamination of the subsoil and groundwater. It contains provisions on control and the pollution limit values. This decree is in compliance with Directive 2006/118/EC of the European Parliament and of the Council on the protection of groundwater against pollution and deterioration.

In case of scrubber waters from waste incineration plants the relevant Hungarian regulation was KöM Decree 3/2002 (II. 22.) *On technical requirements, operating conditions and technological emission limits of waste incineration plants,* where the given technological emission limits were higher than the pollution limit values.

Decree No. 29 of 2014 (XI. 28.) FM of the Ministry of Agriculture repealed KöM Decree 3/2002 (II. 22.) on January 12, 2014 and the new decree does not stipulate technological emission limits for waters, they were incorporated in Kv-VM Decree 28/2004 (XII. 25.).

In the evaluation of the obtained experimental results and their discussion we considered the pollution limit values regarding both tested contaminated waters.

3.2. Metal concentration drop in case of the tested effluents

Three liters of the pretreated groundwater were fed downward through 4 columns in series at ~1.6 $mL*s^{-1}$ flow rate using a peristaltic pump, after the fourth column the effluent was fed again into the first and then the second columns (marked as 1* and 2* on the horizontal axis of *Figure 3*).

Figure 3 shows the drop in concentrations of different heavy metals (cadmium, copper, lead, nickel and zinc) after flowing through the biosorption columns (column number 0 shows the initial concentration of the effluent). The red lines indicate the pollution limit values according to Hungarian Decree No. 6/2009 (IV. 14.).

We found that the pH increased after every column from 4.8 to 5.5. It can be seen from *Figure 3* that the concentrations of all of the investigated heavy metals decreased after almost every step of the in-series coupled columns (see 1–4 on the horizontal axis) for the contaminated groundwater containing several heavy metals at different concentrations. After the second biosorption experiment with the same column (see 1* and 2* on the horizontal axis) the concentrations did not decrease further, and in some cases some desorption could be noticed as well. Thus, it can be declared that the biomass in the columns have become saturated with heavy metals during the first flow through.

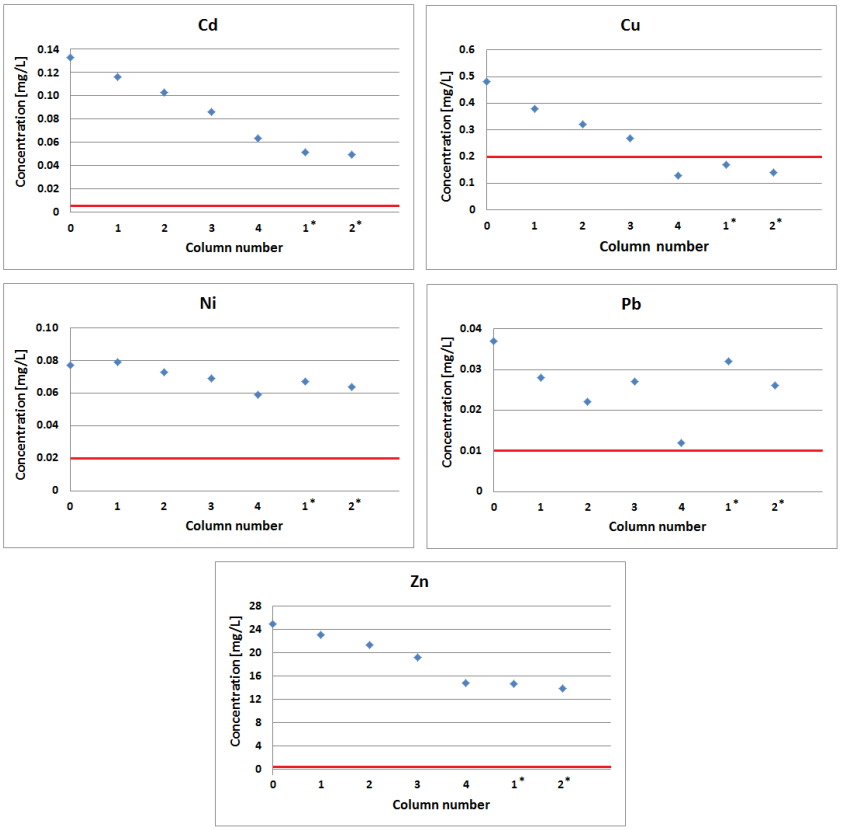

Figure 3. Concentration drop in the groundwater sample for different heavy metals (horizontal axis: 0 – initial concentration of the contaminated groundwater; 1...4 – concentrations after the first...fourth columns, 1 – concentration after the second flow through in the first column, 2* – concentration after the second flow through in the second column)*

Only the concentration of copper decreased below the given pollution limit value, but it is possible to observe a significant reduction in the concentration of Cd and Zn as well. It should be noted here that this groundwater contains several heavy metals, and there are significant differences in the initial concentrations of different metals.

It is noticeable as well that there are some cases when the metal concentration after the biosorption is higher than before it. This phenomenon can only indicate that the applied biosorbent had its own heavy metal burden before, despite the applied pretreatment.

Three liters of the pretreated scrubber effluent were fed downward through 2 columns in line at ~1.6 $mL*s^{-1}$ flow rate using a peristaltic pump.

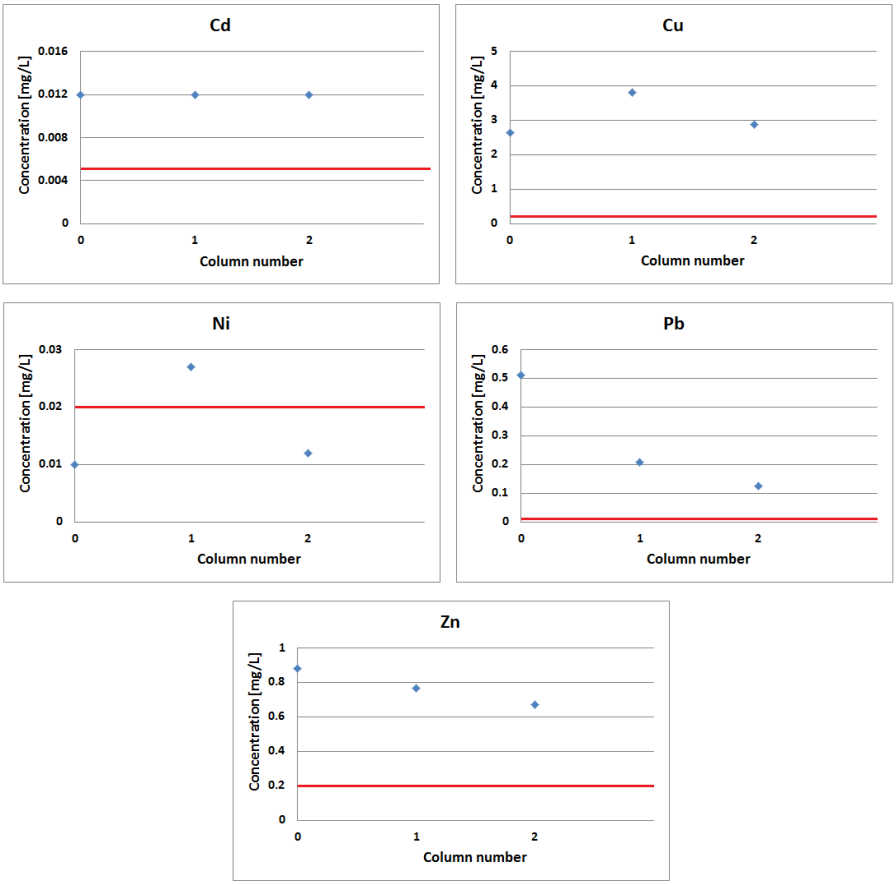

Figure 4. Concentration drops in the scrubber effluent sample for different heavy metals (horizontal axis: 0 – initial concentration of the contaminated scrubber water; 1 – concentration after the first column, 2 – concentration after the second column)

Figure 4 shows the changes of concentration of various heavy metals (cadmium, copper, lead, nickel and zinc) after flowing through the biosorption columns. The red lines indicate the pollution limit values according to Hungarian Decree No. 6/2009 (IV. 14.).

It can be seen from *Figure 4* that the measured concentrations of Cd, Cu, Pb and Zn in the liquid phase are above the pollution limit values before and after the biosorption. Significant concentration reduction can only be observed in the case of Pb and Zn after two columns.

In case of the copper we could not manage to reduce the concentration under the pollution limit value; in fact, after the biosorption an even higher concentration could be measured. This phenomenon indicates that the applied biosorbent had its own heavy metal burden before the biosorption, despite the applied pretreatment.

Only in the case of lead could a significant reduction of the concentration after both columns be observed. We were able to reduce the concentration below 0.2 mg/L, which is the technological emission value according to Kv-VM Decree 28/2004 (XII. 25.).

The selective adsorption ability of *U. pinnatifida* towards the lead established in the experiments with polycationic model solutions is therefore confirmed in the case of a real effluent.

The obtained biosorption results for the real effluent systems are somewhat poorer than those for the model solutions. The reason can be the diversity of the competitive cations and anions, as well as the processing difficulties using columns in series.

4. CONCLUSIONS

Considering that *U. pinnatifida* are invasive algae, their cultivation, harvesting and use as biosorbent for wastewater polluted with transition metals could represent an effective alternative to remove polluting metals from industrial effluents.

It was found that the applied biosorbent is able to reduce the polluting transition metal concentrations, especially that of lead, in both tested real effluents: the contaminated groundwater and the scrubber effluent samples. Nevertheless, to achieve effective biosorption it is necessary to adjust the pH value of the initial solution to a value between pH = 4 and 6.

In the selection of the raw material of the biosorbent, it is important to know the place of origin and previous treatment of the biomass – especially for macro algae – because it can become contaminated with pollutants (e.g. heavy metals) from the environment during its growth and from the pretreatment processes after harvesting, as well.

The porosity of the biosorbent is also a very important parameter for the design processes of biosorption in columns. Special circumstances are needed in the case of macro algae, because the dried macro algae can swell significantly when contacting water. This can negatively affect the diffusion phenomenon.

It was further proved that *U. pinnatifida* has a selective adsorption ability towards lead. The results obtained for the real systems are somewhat poorer than for polycationic model solutions. The main reason is the complexity of the real solutions, as well as the processing difficulties using columns in the series described above.

ACKNOWLEDGEMENTS

This research was supported by the cooperation between the Institute of Raw Material Preparation and Environmental Processing, University of Miskolc and the EMK North Hungarian Environmental Protection Ltd., Hungary. The laboratory assistance of B.Sc. students Janka Laczkó and Mercédesz Evelin Zsiri is also highly appreciated.

REFERENCES

[1] BOKÁNYI–PAULOVICS–BUNKE 2009
BOKÁNYI, L.–PAULOVICS, J.–BUNKE, G.: Az „Undaria pinnatifida" makroalgán történő bioszorpció leírásának pontosítása. *Proceedings of 5th Carpathian Basin Conference on Environmental Sciences.* Cluj-Napoca, Romania, March 26–29, 2009, 233–238.

[2] BOKÁNYI et al. 2011
BOKÁNYI, L.–VARGA, T.–MÁDAI-ÜVEGES, V.–PAULOVICS, J.: Bioprocessing research in Institute of Raw Materials Preparation and Environmental Processing, University of Miskolc. *Biotechnology & Metals 2nd International Conference,* Košice, 22–23. 09. 2011. Košice, Slovakia, ISBN: 978-80-553-0723-7, 5–8.

[3] BUNKE et al. 2003
BUNKE, G.–SCHLÜPMANN, D.–PARK, J. H.–WILKE, A.–STAN, H.-J.: *Biosorption von Schwermetallen mit Makro- und Mikroalgen.* Poster, Gemeinschaftsstand des Landes Berlin zur Biotechnica, 2003.

[4] DHANKHAR–HOODA 2011
DHANKHAR, R.–HOODA, A.: Fungal biosorption – an alternative to meet the challenges of heavy metal pollution in aqueous solutions. *Environ. Technol,* 32, 2011, 467–491.

[5] GADD 2009
GADD, G. M.: Biosorption: critical review of scientific rationale, environmental importance and significance for pollution treatment. *J. Chem. Technol. Biotechnol,* 84, 2009, 13–28.

[6] KIM et al. 1999
KIM, Y. H.–PARK, J. Y.–YOO Y. J.–KWAK, J. W.: Removal of lead using xanthated marine brown alga, "Undaria pinnatifida". *Process Biochem,* 34, 1999, 647–652.

[7] KLIMMEK et al. 2001
KLIMMEK, S.–WILKE, A.–BUNKE, G.–BUCHHOLZ, R.–STAN, H.-J.: Characterization of the Biosorption of Cadmium, Lead, Nickel and Zinc by Algae. *Environ. Sci. Technol,* Vol. 35, No. 21 (2001), 4283–4288.

[8] LEUSCH–HOLAN–VOLESKY 1995
LEUSCH, A.–HOLAN, Z. R.–VOLESKY, B.: Biosorption of heavy metals (Cd, Cu, Ni, Pb, Zn) by chemically-reinforced biomass of marine algae. *J. Chem. Technol. Biotechnol,* 62, 1995, 279–288.

[9] MONTAZER-RAHMATIA et al. 2011
MONTAZER-RAHMATIA, M. M.–RABBANIA, R.–ABDOLALIA, A.–KESHTKARB, A. R.: Kinetics and equilibrium studies on biosorption of cadmium, lead, and nickel ions from aqueous solutions by intact and chemically modified brown algae. *J. Hazard. Mater,* 185, 2011, 401–407.

[10] PLAZA CAZÓN 2013
PLAZA CAZÓN, J.–VIERA, M.–DONATI, E.–GUIBAL, E.: Zinc and cadmium removal by biosorption on "Undaria pinnatifida" in batch and continuous processes. *Journal of Environmental Management,* 129, 2013, 423–434.

[11] YINGHUI LIU–CAO–LUO 2009
YINGHUI LIU, Q.–CAO, F.–LUO, J. C.: Biosorption of Cd^{2+}, Cu^{2+}, Ni^{2+} and Zn^{2+} ions from aqueous solutions by pretreated biomass of brown algae. *J. Hazard. Mater,* 163, 2009, 931–938.

Geosciences and Engineering, Vol. 4, No. 7 (2015), pp. 86–96.

EFFECT OF VARIOUS PRODUCTION PARAMETERS ON BIOMASS AGGLOMERATION

TRINH VAN QUYEN[1]–SÁNDOR NAGY[2]

[1]PhD student, [2]Associate Professor
[1,2]Institute of Raw Materials Preparation and Environmental Processing
University of Miskolc

Abstract: The use of biomass is a good option for domestic heating systems and power plants to reduce their fossil CO_2 emissions. The agglomeration of biomass by methods such as extrusion, tableting, or pelletizing can increase bulk density, improves storability, reduces transportation costs, makes handling easier, and increases the quality of products. The aim of this article is to analyze the effects of temperature, moisture content (MC) and particle size on the products of beech biomass tableting and also to find the optimal conditions of the densification process for producing tablets with high density. Beech biomass was compressed in a load cell with a hydraulic piston press of 25 mm diameter. Effects of independent variables, including temperature (20 °C to 100 °C), moisture content conditions (1.47 m/m % and 9.27 m/m % in the case of x < 1 mm, and 1.44 m/m % and 9.68 m/m % in the case of x < 2 mm) were investigated. Results showed that for constant pressure, the increasing temperature resulted in higher density tablets, but higher moisture content resulted in lower density tablets. Increasing the temperature over 40 °C resulted in only minimal density growth. Tablets made from raw materials with smaller particle size have lower strength compared to tablets made from materials with larger particle size.

Keywords: *agglomeration, densification, pelletizing, tableting, extrusion, biomass, beech*

1. INTRODUCTION

Wood pellet production in the European Union was estimated to be about 10 million tons (SIKKEMA et al., 2011) and 6.2 million tons for North America (SPELTER and TOTH, 2009) for year 2009. Another study by COCCHI et al. (2011) estimated a slightly lower value for the global pellet production of about 14.3 million tons for the year 2010. The globally installed pellet production capacity for 2011 was estimated to be at about 30 million tons. All studies suggest a strong growth for both the European and North American pellet markets. The Finnish Pöyry Industry consulting company has predicted growth of the global pellet production capacity to 46 million tons by 2020 (PÖYRY, 2011) [5].

2. LITERATURE OVERVIEW

During pressure agglomeration, new, enlarged entities (tablets, briquettes etc.) are formed by applying external forces to particulate solids in more or less closed dies that define the shape of the agglomerated product *(Figure 1)* [3].

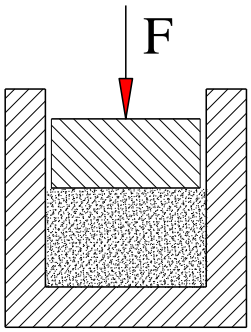

Figure 1. Pressure agglomeration

Plenty of models exist for describing the compaction behavior of bulk materials (compressibility). Some of them are introduced in the following form, starting with the most relevant one (Johanson's equation) [6]:

$$\frac{\rho}{\rho^*} = \left(\frac{\mathrm{p}}{\mathrm{P}^*}\right)^{1/\kappa},$$

where κ is the compressibility factor, ρ is agglomerate density, p is tableting pressure and p^*, ρ^* are reference values.

The compaction characteristics of chopped biomass with the application of normal pressure have been studied using models developed by KAWAKITA and LUDDE (1971) and WALKER (1923). Walker proposed the following model for understanding the pressure-volume relationships of calcium carbonate and tetranitro-methylaniline, and subsequently various researchers used this model for biological materials:

$$V = a_1 - K_1 lnP,$$

where V is relative volume ratio, P is applied pressure (kPa), and a_1 and K_1 are constants. Another model widely used for understanding the pressure-volume relationship was developed by KAWAKITA and LUDDE (1971):

$$\frac{P}{C} = \frac{1}{a_2 b_2} + \frac{P}{a_2},$$

where P is applied pressure, a_2 and b_2 are constants, and C is relative volume decrease or engineering strain given by the equation:

$$C = \frac{V_0 - V_P}{V_0},$$

where V_0 is the initial volume and V_P is volume measured at any given pressure. The model was further developed by SONE (1969) [1].

HECKET (1961) proposed a model to express the compaction behavior of compressed powders. The equation expresses the density of powdered materials in terms of packing fractions as a function of the applied pressure:

$$ln\frac{1}{1-\rho_f} = mp + n \text{ and } \rho_f = \frac{\rho}{\rho_1 X_1 + \rho_2 X_2},$$

where ρ_f is packing fraction or relative density of the material after particle rearrangement. p is applied pressure (MPa); m, n are Heckel model constants; ρ is bulk density of compacted powder mixture (kg/m^3); X_1, X_2 are mass fractions of components of the mixture.

SHIVANAND and SPROCKEL (1992) showed that constant n is related to relative density at particle rearrangement:

$$n = ln\frac{1}{1-\rho_f}.$$

A high ρ_f value indicates that there will be a high volume reduction of the sample due to particle rearrangement. The constant m has been shown to be equal to the reciprocal of the mean yield pressure required to induce plastic deformation. A larger value for m (low yield pressure) indicates the onset of plastic deformation at relatively low pressure, a sign that the material is more compressible [2].

Biomass sources with different chemical compositions require different process parameters for their densification. Production temperature and moisture content of the raw material are the two most important process parameters that influence the quality of biomass agglomerates [4]. The effect of raw material moisture content on the pelletizing properties and product quality has been the subject of several studies (NIELSEN et al., 2009a; STELTE et al., 2011b). In these studies the optimum moisture content for the densification of beech was 6 m/m % to 10 m/m % [7], for spruce it was about 10 m/m % [8].

In this article the effects of temperature, moisture content and particle size were investigated on the density and strength of beech biomass tablets.

3. MATERIALS AND METHODS

3.1. Material

Beech sawdust was chosen as raw material for our experiments. It originates from Miskolc, Hungary (Borsodwood Ltd.). It was dried and then ground using a cutting mill (Retsch SM2000) in two steps (screen sizes: 2 mm and 1 mm). The biomass was stored at room temperature (25 °C) in closed plastic bags. The moisture content conditions (1.47 m/m %, 9.27 m/m % in the case of x < 1 mm, and 1.44 m/m %, 9.68 m/m % in the case of x < 2 mm).

3.2. Apparatus

The hydraulic piston press *(Figure 2)* was designed and produced by the University of Miskolc. The press is supported by a pump motor unit with pressure limiter and a heatable load cell (20–140 °C). The maximal force is 200 kN, and the maximal velocity of the piston feed rate is 30 mm/s. The measuring of the piston position is solved by an incremental encoder. The PC data acquisition software was written in LabWindows C by J. Faitli.

Figure 2. Hydraulic piston press

3.3. Experimental procedure

The piston press diameter was 25 mm, and each tablet was made by the compression of 5 g sawdust. The five applied temperatures were 20 °C, 40 °C, 60 °C, 80 °C and 100 °C. The five applied pressures on the surface of tablets were 50 MPa, 100 MPa, 150 MPa, 200 MPa and 250 MPa. Experiments were carried out with two particle size fractions: < 1 mm and < 2 mm.

The quality of the tablets can be described easily by the density. The diameters and heights of the tablets were measured by a Vernier caliper (the tablet can be extended after agglomeration). The mass was measured and the density was calculated for each test sample.

Determination of tablet strength was carried out by the known falling test method. Tablets were released by freefall from a height of 2 m onto a concrete floor as many times as needed until breaking. The Falling number is the number of undamaged falls. In every experiment three tablets were tested.

4. RESULTS AND DISCUSSION

4.1. Tablet density

Tablets produced using different parameters are shown in *Figure 3*.

a)

b)

Figure 3. Tablets made from particle size x < 1mm (a); particle size x < 2 mm (b)

Tables 1 and *3* show the tablet density values, which were recorded as an average of five measurements at particle size x < 1mm and also for particle size x < 2 mm.

Table 1
Tablet density values (particle size x < 1mm)

Pressure, p [MPa]	**Density, $\bar{\rho}$** [kg/m^3]					
	MC = 1.47 m/m %					MC = 9.27 m/m %
	$\bar{\rho}_{20^oC}$	$\bar{\rho}_{40^oC}$	$\bar{\rho}_{60^oC}$	$\bar{\rho}_{80^oC}$	$\bar{\rho}_{100^oC}$	$\bar{\rho}_{20^oC}$
50	639.0	679.8	712.6	689.4	744.8	674.44
100	829.0	898.2	910.6	912.4	916.0	827.4
150	942.2	1007.4	1008.2	1006.6	1013.0	912.89
200	1011.4	1022.8	1030.0	1034.6	1051.8	948.84
250	1040.0	1058.0	1065.0	1090.2	1099.6	982.11

The description of compression was carried out according to Johanson's equation $\rho = ap^{1/k}$. *Figure 4* shows the pressure-density values and the fitted curves in the case of < 1 mm raw material at 20 °C, 40 °C, 60 °C, 80 °C and 100 °C. *Table 2* shows the constants of the fitted curves and coefficient of determination *(R^2),* residual mean square *(σ)* and calculated deviation *(V_s).* Results for particle size x < 2 mm are introduced in *Figure 5* and *Table 4.*

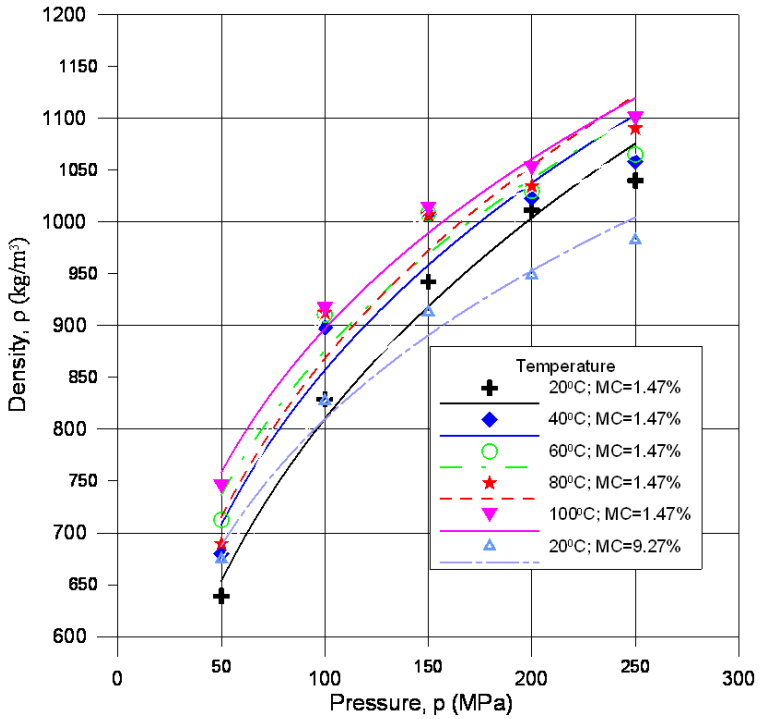

Figure 4. Compressibility of biomass on different temperatures (x < 1mm)

Results showed that at the same pressure and temperature, higher moisture content resulted in lower density of tablet (if p > 100 MPa). At the same pressure and moisture content, higher temperatures resulted in higher density of the tablet. Increasing the temperature over 40 °C resulted in only a minimal density growth.

Table 2
Constants of Johanson's equation at different temperatures (x < 1mm)

Temperature [°C]	**Moisture content % (MC)**	**Constant "a"**	**Constant "κ"**	**Spread deviation: V_s Coef. of determination: R^2 Residual mean square: σ**
20	9.27	273.9956	4.2517	$R^2 = 0.9782$; σ = 0.00066; $V_s = 3.0\%$
20	1.47	194.5093	3.2283	$R^2 = 0.9816$; σ = 0.00096; $V_s = 2.78\%$
40	1.47	240.7600	3.6271	$R^2 = 0.9366$; σ = 0.00276; $V_s = 4.53\%$
60	1.47	276.8318	3.9980	$R^2 = 0.9492$; σ = 0.00180; $V_s = 3.64\%$
80	1.47	239.2337	3.5727	$R^2 = 0.9535$; σ = 0.00205; $V_s = 3.79\%$
100	1.47	294.5099	4.1350	$R^2 = 0.9820$;σ = 0.00057; $V_s = 2\%$

Table 3
Tablet density values with particle size x < 2mm

Pressure, [MPa]	**Density ($\bar{\rho}$), [kg/m^3]**					
	MC = 1.44 m/m %					MC = 9.68 m/m %
	$\bar{\rho}_{20^0C}$	$\bar{\rho}_{40^0C}$	$\bar{\rho}_{60^0C}$	$\bar{\rho}_{80^0C}$	$\bar{\rho}_{100^0C}$	$\bar{\rho}_{20^0C}$
50	659.6	684.0	748.4	727.0	722.2	719.47
75	737.4	780.4	814.2	836.6	808.2	795.33
100	849.6	901.6	864.0	922.4	914.0	848.75
125	908.2	937.2	949.6	972.2	956.6	904.33
150	952.6	988.6	1004.2	1010.2	1013.4	941.72
175	985.2	1013.4	1020.0	1023.0	1033.4	966.83
200	1012.2	1031.0	1027.4	1054.8	1047.8	991.7
225	1026.0	1037.2	1051.4	1071.2	1079.6	1006.6
250	1030.8	1052.8	1073.4	1090.6	1097.8	1026.8
275	1055.4	1071.4	1092.8	1098.0	1112.0	1052.9

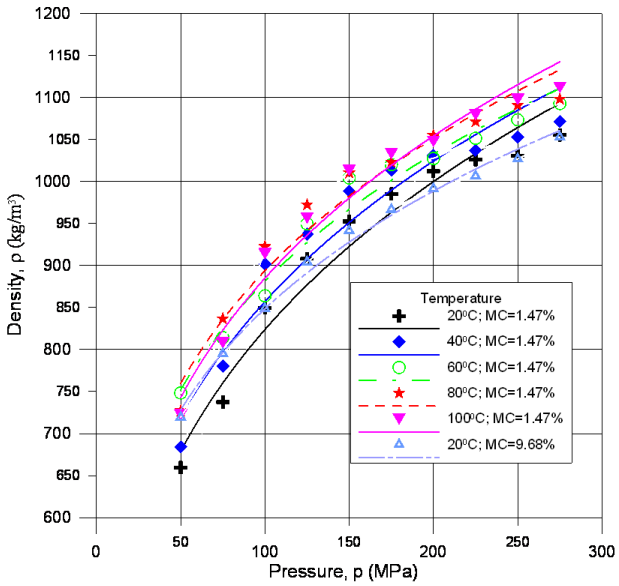

Figure 5. Compressibility of biomass at different temperatures (x < 2 mm)

Results showed that at the same pressure and temperature, higher moisture content resulted in lower density tablets. At the same pressure and moisture content, with increasing temperature the density of tablets increased as well. Increasing the temperature over 40 °C resulted in only a minimal density growth.

Regarding the particle size of the raw material, x < 2 mm and x < 1mm, the densities of the produced tablets were practically the same (at constant pressure, temperature and moisture content).

Table 4

Constants of Johanson's equationat different temperatures (x < 2 mm)

Temperature [°C]	**Moisture content % (MC)**	**Constant "a"**	**Constant "κ"**	**Spread deviation: V_s Coef of determination: R^2 Residual mean square: σ**
20	9.68	307.3354	4.5351	$R^2 = 0.9934$; σ = 0.00011; V_s = 2.2 %
20	1.44	227.3821	3.5775	$R^2 = 0.9647$; σ = 0.00098; V_s = 4.18%
40	1.44	262.2798	3.8892	$R^2 = 0.9438$; σ = 0.00135; V_s = 4.24%
60	1.44	307.4255	4.3731	$R^2 = 0.9767$; σ = 0.00042; V_s = 3%
80	1.44	303.8298	4.2682	$R^2 = 0.9617$;σ = 0.00075; V_s = 3.1%
100	1.44	276.6470	3.9605	$R^2 = 0.9725$; σ = 0.00062; V_s = 3.4%

The magnitude of the calculated spread deviation values *(V_s)* was lower than 5% for all of the tests parameters shown in *Tables 2* and *4*. At the same temperature, the increasing moisture content resulted in a higher constant "a" and constant "κ" (both for x < 1 mm and x < 2 mm).

4.2. Tablet strength

Tables 5 and *6* show the results of the falling tests in the case of < 1 mm and < 2 mm raw materials. Falling number is shown in *Figure 6* as a function of temperature at different pressure values.

Table 5

Falling number of tablets (particle size x < 1mm) formed at different pressures and temperatures, for two moisture contents

Temperature [°C]	**Pressure**				
	50 MPa	100 MPa	150 MPa	200 MPa	250 MPa
	Falling number				
	MC = 9.27%				
20	0.00	1.00	2.66	3.00	4.00
20	MC = 1.47%				
	0.00	0.00	0.33	2.00	2.33
40	0.00	0.66	2.66	3.00	4.33
60	0.00	1.00	2.66	4.66	3.33
80	0.00	1.00	2.66	4.33	5.00
100	0.00	0.00	3.33	4.66	6.00

Table 6
Falling number of tablets (particle size x < 2 mm) formed at different pressures and temperatures, for two moisture contents

Temperature [°C]	Pressure					
	50 MPa	100 MPa	150 MPa	200 MPa	250 MPa	275 MPa
	Falling number					
	MC = 9.68%					
20	0.00	1.33	3.00	5.33	4.00	5.00
20	MC = 1.44%					
	0.00	1.00	2.66	4.00	4.00	5.33
40	0.00	1.00	3.66	5.00	6.00	6.00
60	0.00	2.00	4.33	6.00	8.33	9.00
80	0.00	2.66	6.00	7.66	10.33	10.00
100	0.00	2.33	5.66	7.33	10.66	11.00

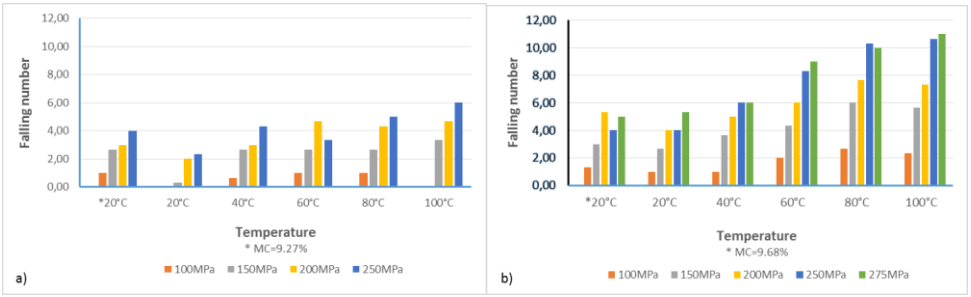

Figure 6. Relationship between falling number, temperature and pressure
a) Particle size < 1 mm, MC = 1.47 m/m % (except first data)
b) Particle size < 2 mm, MC = 1.44 m/m % (except first data)

Tablets made from raw material x < 2 mm (MC = 1.44 m/m %) have higher strength than tablets made from material x < 1 mm biomass (MC = 1.47 m/m %) if the applied temperature and pressure were constant (with the exception of p = 50 MPa).

5. CONCLUSIONS

This paper has presented tools and methods to evaluate the effect of process temperature, pressure and particle size on the produced tablet density for beech sawdust. The description of the processes at the laboratory scale is essential to be able to determinate the optimal parameters by which later production of proper agglomerate quality and low production costs will be achieved. The applied Johanson

function describes well the processes (at 60 °C, in the case of < 1 mm raw material $V_S = 3.64\%$, using < 2 mm raw material $V_s = 3.00\%$).

For the same pressure and particle size, increasing temperature resulted in higher density tablets (in the case of < 1 mm raw material at 100 MPa the tablet densities: 829 kg/m^3 [20 °C] and 916 kg/m^3 [100 °C]). Increasing the temperature over 40 °C does not result in a significant increase indensity. If temperature and pressure are kept constant, tablets made from material x < 2 mm have higher strength (falling number: 7.33 at 200 MPa and 100 °C) than tablets made from x < 1 mm biomass (falling number: 4.66 at 200 MPa and 100 °C).

The method can be used for other materials as well to find the optimal condition of pressure, temperature and particle size during an agglomeration process.

The effect of moisture content on tablet density can be explained by different stress-strain behavior of wood particles with various moisture contents. It is necessary to investigate these phenomena in more detail in further research work.

ACKNOWLEDGEMENTS

This publication was carried out as research within the Centre of Excellence of Sustainable Resource Management, in the framework of the New Széchenyi Plan. The realization of this project is supported by the European Union, co-financed by the European Social Fund. The Research work of Trinh Van Quyen was supported by the Stipendium Hungaricum Scholarship Program. The author thanks Mrs. Bernáth and Mrs. Seszták for their support in the laboratory.

REFERENCES

[1] CHEVANAN 2010
CHEVANAN, N.: Bulk density and compaction behavior of knife mill chopped switchgrass, wheat straw, and cornstover. *Bioresource Technology,* 101, 2010, 207–214.

[2] MANI 2004
MANI, S.: Evaluation of compaction equations applied to four biomass species. *Canadian Biosystems Engineering,* Vol. 46, 2004, 355–361.

[3] PIETSCH 2005
PIETSCH, W.: *Agglomeration in Industry: Occurrence and Applications.* 2005.

[4] XIA 2016
XIA, Z.: Effect of moisture content and temperature on the quality of water hyacinth pellets. *Bio Resources,* Vol. 11, No. 1 (2016), 1407–1416.

[5] STELTE 2012
STELTE, W.: Recent developments in biomass palletization – a review. *Bio Resources,* Vol. 7, No. 3 (2012), 4451–4490.

[6] STIESS 1993
STIESS: *Mechanische Verfahrenstechnik 2.* Springer Lehrbuch, 1993.

[7] NIELSEN 2009a
NIELSEN, N. P. K.: Importance of temperature, moisture content, and species for the conversion process of wood residues into fuel pellets. *Wood Fiber Sci,* Vol. 41, No. 4 (2009), 414–425.

[8] STELTE 2011b
STELTE, W.: Fuel pellets from biomass: The importance of the pelletizing pressure and its dependency on the processing conditions. *Fuel,* Vol. 90, No. 11 (2011), 3285–3290.